Divergent changes in aerosol optical hygroscopicity and new particle

2	formation during <u>a</u> heatwaves of summer 2022
3	
4	Yuhang Hao ^{1, a} , Peizhao Li ^{1, a} , Yafeng Gou ¹ , Zhenshuai Wang ¹ , Mi Tian ¹ , Yang Chen ² ,
5	Ye Kuang ³ , Hanbing Xu ⁴ , Fenglian Wan ¹ , Yuqian Luo ¹ , Wei Huang ⁵ , Jing Chen ^{1, 6, *}
6	
7	¹ College of Environment and Ecology, Chongqing University, Chongqing 400045,
8	China
9	² Center for the Atmospheric Environment Research, Chongqing Institute of Green
10	and Intelligent Technology, Chinese Academy of Sciences, Chongqing 400714, China
11	³ Institute for Environmental and Climate Research, Jinan University, Guangzhou
12	511443, China
13	⁴ Experimental Teaching Center, Sun Yat-sen University, Guangzhou 510275, China
14	⁵ National Meteorological Center, China Meteorological Administration, Beijing
15	100081, China
16	⁶ Key Laboratory of Three Gorges Reservoir Region's Eco-Environment, Ministry of
17	Education, Chongqing University, Chongqing 400045, China
18	
19	^a These authors contributed equally
20	Company day as to line Chan (shen iin a Gagy adv an)
21	Correspondence to: Jing Chen (chen.jing@cqu.edu.cn)

Abstract. As a crucial climate-forcing driver, the aerosol optical enhancement factor (f(RH)) is significantly modulated by chemical compositions and the evolution of particle number size distribution (PNSD), e.g., during new particle formation (NPF). However, the mechanisms regulating aerosol optical hygroscopicity during different NPF days, particularly those influenced by heatwaves due to global warming, remain poorly understood. In the extremely hot summer of 2022 in urban Chongqing of southwest China, simultaneous measurements of aerosol optical and hygroscopic properties, PNSD, and bulk chemical compositions were conducted. Two distinct types of NPF were identified: the ones with relatively polluted period (NPF_{polluted}) and clean cases during heatwave-dominated period (NPFclean, HW). Compared to the NPF_{polluted} events, NPF_{clean}, HW occurred approximately one hour earlier and the subsequent growth was prolonged, accompanied by a smaller aerosol effective radius (Reff) and lower formation/growth rate during heatwaves. This agreed with the concurrently increased aerosol hemispheric backscattering fraction and scattering Ångström exponent. f(RH) was generally higher on NPF days in comparison to that for non-event cases in both periods. Moreover, heatwave-induced stronger photooxidation may intensify the formation of more hygroscopic secondary components, as well as the atmospheric aging/subsequent growth of both pre-existing and newly formed particles, thereby enhancing f(RH) especially during NPF_{clean, HW} days. The promoted f(RH) and lowered R_{eff} could synergistically elevate the aerosol direct radiative forcing, specifically under persistent heatwave conditions. Further in-depth exploration on molecular-level characterizations and aerosol radiative impacts of both direct and indirect interactions during underweather extremes (e.g., heatwaves) and other weather extremes with the warming climate are recommended.

46

47

48

49

22

23

24

25

26

27

28

29

30

31

32

33

34

35

36

37

38

39

40

41

42

43

44

45

1 Introduction

Weather extremes (e.g., heatwaves) have become more and more frequent and intense largely due to the global climate change, and the heatwave-driven

environmental, climatic, and health effects have garnered widespread attention (Hauser et al., 2016; Sun et al., 2016). The China Climate Bulletin 2022 confirmed that the national average temperature reached an unprecedented high level since 2012 (China Meteorological Administration, 2022), and the risk of heatwaves in China will persist and potentially intensify in the future (Guo et al., 2016; Li et al., 2017). Extreme heatwave events could pose significant threats to human health, the survival of organisms, agriculture, and socio-economic activities (e.g., power supply restrictions) (Anderson and Bell, 2011; Ma et al., 2021; Su, 2021). Moreover, heatwaves can trigger natural disasters such as droughts and wildfires, affecting social stability (Sharma and Mujumdar, 2017).

50

51

52

53

54

55

56

57

58

59

60

61

62

63

64

65

66

67

68

69

70

71

72

73

74

75

76

77

78

79

Heatwaves could also affect the atmospheric physical and chemical processes by modulating ambient meteorological conditions. Specifically, extremely high temperature weather is typically characterized by a combination of intensified solar radiation with elevated temperature and low humidity levels. This could significantly affect the formation and evolution of secondary aerosols in the atmosphere (Bousiotis et al., 2021; Hamed et al., 2011; Kurtén et al., 2007), given that the air temperature is crucial for chemical reactions (Xu et al., 2011). New particle formation (NPF) serves as a crucial source of atmospheric particulate matter and plays a significant role in the secondary transformation processes in the atmosphere (Zhu et al., 2021). Generally, NPF involves the initial formation of thermodynamically stable clusters from condensable vapors (e.g., ammonia, sulfuric acid, and organic precursor gases) and subsequent growth of the formed clusters, eventually reaching detectable sizes or even larger dimensions (Kerminen et al., 2018; Kulmala et al., 2003, 2012). Over time, these newly formed particles have the potential to serve as cloud condensation nuclei (CCN), thereby impacting the global climate (Salma et al., 2016). NPF events normally introduce a sharp increase in the number concentration of nucleation mode particles within a short time, altering the particle number size distribution (PNSD). These variations in PNSD likely influence intrinsic physicochemical properties of aerosols, such as the optical hygroscopicity (Chen et al., 2014; Titos et al., 2016; Zhao et al., 2019).

Aerosol hygroscopicity plays a critical role in the atmospheric environment and climate change, given the complex interaction between aerosol particles and water vapor (Zhao et al., 2019; Zieger et al., 2011). Water uptake by aerosols not only alters the particle size and composition (e.g., as reflected in the aerosol refractive index) but also impacts aerosol scattering efficiency, which further contributes to the uncertainty in aerosol radiative forcing estimation (Titos et al., 2016, 2021). The aerosol optical hygroscopicity parameter, f(RH), defined as the ratio of the scattering coefficient at a certain RH to that of the dry condition, was widely used to describe the aerosol scattering enhancement through water uptake (Covert et al., 1972; Titos et al., 2016; Zhao et al., 2019). Numerous studies have demonstrated that f(RH) is influenced by the size distribution, in addition to particle chemical composition (Chen et al., 2014; Kuang et al., 2017; Petters and Kreidenweis, 2007; Quinn et al., 2005). There is currently limited research on the variations in aerosol optical hygroscopicity during NPF days despite significant changes in aerosol size distributions and chemical compositions, partly due to that newly formed particles insignificantly affect the optical properties of aerosols (Kuang et al., 2018). However, previous studies have observed the enhancement in aerosol hygroscopicity (Cheung et al., 2020; Wu et al., 2015, 2016) and extinction coefficients (Shen et al., 2011; Sun et al., 2024) during the subsequent growth of NPF. It is suggested that the influence of NPF on aerosol hygroscopicity was likely due to changes in aerosol chemical composition at different stages of NPF events (Cheung et al., 2020), whereas the subsequent particle growth associated with NPF events can significantly affect particle hygroscopicity as well (Wu et al., 2016). Although previous studies showed the dependences of aerosol hygroscopicity on chemical composition (Petters and Kreidenweis, 2007; Titos et al., 2016; Zhao et al., 2019) (e.g., the variation in composition of precursor species during NPF events), it is important to acknowledge that the utilized chemical compositions of NPF were either from PM_{2.5} or PM₁ bulk data. This may differ from the corresponding composition of newly formed ultrafine particles primarily in the nucleation and Aitken modes, further introducing bias in exploring the impacts of NPF and subsequent growth on aerosol optical hygroscopicity. Hence, more

80

81

82

83

84

85

86

87

88

89

90

91

92

93

94

95

96

97

98

99

100

101

102

103

104

105

106

107

108

comprehensive investigations on the influencing mechanisms of aerosol optical hygroscopicity from different perspectives are required, e.g., for the aspects of the evolution of particle size distribution in modulating aerosol optical and hygroscopic properties (Tang et al., 2019; Zhao et al., 2019). Additionally, field observations on f(RH) under extreme weather conditions (e.g., heatwaves) are rather scarce, largely hindering our understanding of how weather extremes (e.g., extremely high temperature) influence the optical hygroscopic properties of aerosols. This knowledge gap further impedes comprehensive understanding of the aerosol water uptake property and resulted effects on air quality and the climate under varied synoptic conditions.

During the summer of 2022, a rare heatwave event raged throughout China, especially the Sichuan-Chongqing region of southwest China (Chen et al., 2024; Wang et al., 2024), with the daily maximum temperature exceeding 40 °C lasted for 29 days observed at Beibei meteorological station in Chongqing (Hao et al., 2023). This persistent heatwave not only impacted residents' daily lives significantly, but also affected the aerosol optical and hygroscopic properties likely through changed aerosol physicochemical characteristics and relevant atmospheric processing during the period. In this study, a field observation was conducted by using a combination of a home-built humidified nephelometer system and a scanning mobility particle sizer (SMPS), along with the total suspended particle (TSP) filter sampling. A main goal of this study is to investigate the influence of heatwaves on both aerosol optical hygroscopicity and the NPF with subsequent growth events, along with the related discrepancies. Furthermore, we aimed to explore the mechanisms behind the variability in f(RH) under different meteorological conditions and diverse NPF events. This study will further enrich insights into the potential environmental impacts due to variations in the aerosol optical hygroscopicity and size distribution, specifically under weather extremes (e.g., heatwaves) with the changing climate.

2 Data and Methods

138

139

140

141

142

143

144

145

146

147

148

149

150

151

152

153

154

155

156

157

158

159

160

161

162

163

164

165

2.1 Field observation

A continuous field observation on aerosol optical, hygroscopic and chemical properties was carried out from July 29 to August 19, 2022. The detailed description of the observation site is available in Supporting Information, S1. During the observation period, urban Chongqing suffered a rare heatwave (Fig. S1; Chen et al., 2024; Wang et al., 2024), which significantly affected the local transportation and industrial activities (Hao et al., 2023). China Meteorological Administration (CMA) defines heatwaves as three or more consecutive days with daily maximum temperature (T_{max}) above 35 °C (http://www.cmastd.cn/standardView.jspx?id=2103; Guo et al., 2016; Sun et al., 2014; Tan et al., 2007). Since no unified definition of heatwaves worldwide, the whole study period was categorized into two stages according to CMA's criteria of the daily T_{max} records and the Excess Heat Factor (EHF) metric proposed by Nairn and Fawcett (2014) (Fig. S2a): (1) the normally hot period from 29 July to 6 August (marked as P1); (2) the heatwave-dominated period from August 7-19 (marked as P2) characterized with the consistently occurrence of T_{max} exceeding 38 °C (approximately the last 25th percentile of temperature records for the whole observation period; Fig. S2b).

2.2 Instrumentation and methods

2.2.1 Measurements of aerosol optical hygroscopicity

The humidified nephelometer system, consisting of two three-wavelength (i.e., 450, 525, and 635 nm) nephelometers (Model Aurora 3000, Ecotech Inc.) and a humidification unit, was used to determine the aerosol light scattering enhancement factor, f(RH). Ambient air was firstly dried through a Nafion dryer (model MD-700, Perma Pure LLC) to ensure RH <35%, then split into two streams for both dry and humidified nephelometers operated in parallel. The flowrate for each nephelometer was 2.6 LPM. The aerosol scattering (σ_{sca} , λ) and backscattering coefficients (σ_{bsca} , λ) were detected in a dry state (RH <35%) and at a controlled RH level of 85 \pm 1%,

respectively, with the humidification efficiency regulated automatically by a temperature-controlled water bath. More details on the home-built humidified nephelometer system are available in Kuang et al. (2017, 2020) and Xue et al. (2022).

Hence, f(RH) could be calculated as the ratio of the aerosol scattering coefficient at a predefined RH ($\sigma_{sca, RH}$) to the dry ($\sigma_{sca, dry}$) state, i.e., $f(RH) = \sigma_{sca, RH} / \sigma_{sca, dry}$ (Covert et al., 1972). In this study, the f(RH) discussed is mainly targeted for the 525 nm wavelength, unless otherwise specified. More information about the measurement of humidified nephelometer system was illustrated in Sect. S2 of the supplement.

In additional to f(RH), aerosol optical parameters, such as scattering Ångström exponent (SAE; Schuster et al., 2006) and hemispheric backscattering fraction (HBF; Collaud Coen et al., 2007), were calculated as below:

$$SAE_{\lambda 1/\lambda 2} = \frac{-\ln(\sigma_{sea, \lambda 1}/\sigma_{sea, \lambda 2})}{\ln(\lambda 1/\lambda 2)}$$
 (1)

178
$$HBF_{\lambda} = \frac{\sigma_{bsca, \lambda}}{\sigma_{sca, \lambda}}$$
 (2)

where $\sigma_{sca, \lambda}$ and $\sigma_{bsca, \lambda}$ represent the aerosol scattering and backscattering coefficients at a specific wavelength λ (e.g., $\lambda 1$, $\lambda 2$), respectively.

Both HBF and SAE reflect crucial optical properties of aerosols, e.g., an elevated HBF (or SAE) generally signifies a higher concentration (or a smaller particle size) of fine particles within the aerosol population (Jefferson et al., 2017; Kuang et al., 2017; Luoman et al., 2019). The HBF and SAE discussed in this study are targeted for the dry condition, unless otherwise specified. Based on the measurements with the humidified nephelometer system, the equivalent aerosol liquid water content (ALWC) and the corresponding fraction of ALWC (f_W) can also be obtained (Kuang et al, 2018; see Sect. S2 of the supplement).

The SMPS-measured concurrent particle number size distributions were further utilized to calculate the aerosol effective radius (R_{eff}) and representative parameters for NPF events, e.g., the formation rate (FR) and growth rate (GR) of new particle, condensation sink (CS) and coagulation sink (CoagS) (Dal Maso et al., 2005; Kulmala et al., 2012). More details are provided in the supplement (Sect. S5).

Results of the offline chemical analysis with TSP filter samples are provided in Sect. S3 and Fig. S3. It should be noted that certain secondary organics and crustal elements (e.g., Ca²⁺, Mg²⁺) that could exhibit a broader size distribution may contribute to the observed discrepancy in the total mass concentration between the 24-h TSP samples and daily mean PM_{2.5} (of similar temporal variations; Fig.S3) (Duan et al., 2024; Kim et al., 2020; Xu et al., 2021). Nonetheless, previous studies reported that key components such as SNA (i.e., SO₄²⁻, NO₃⁻, and NH₄⁺) and primary organics of PM_{2.5} (or PM₁₀) were predominantly concentrated within the submicron size range (An et al., 2024; Bae et al., 2019; Chen et al., 2019; Duan et al., 2024; Kim et al., 2020; Xu et al., 2024). While the use of TSP samples contains some uncertainties, the bulk chemical information remains reasonable for characterizing the optical and hygroscopic properties of PM_{2.5}. The descriptions of simultaneous meteorological and air quality data can be found in Sect. S4, and the 48-h/72-h backward trajectory analysis was given in Sect. S5 of the supplement.

2.2.2 Determination of the aerosol direct radiative forcing (ADRF) enhancement factor

Given the high sensitivity of aerosol optical properties (e.g., f(RH)) to the changes in RH under real atmospheric conditions, the influence of RH, or rather the aerosol hygroscopicity, on ADRF can be quantitatively estimated with the radiative transfer model by the following equation (Chylek and Wong, 1995; Kotchenruther et al., 1999; L. Zhang et al., 2015):

$$\Delta F_R(RH) = -(S_0/4) \times [T_a^2 \times (1 - A_C)] \times [2 \times (1 - R_s)^2 \times \beta(RH) \times \tau_s - 4 \times R_s \times \tau_a]$$
 (3)

where S_0 is the solar constant, T_a is the atmosphere transmittance, A_C is the fractional cloud amount, R_s is the albedo of the underlying surface, $\beta(RH)$ is the upscattering fraction at a defined RH, τ_s and τ_a are the optical thicknesses of the aerosol layer due to light scattering and light absorption, respectively, which can be expressed as follows (Kotchenruther et al., 1999):

221
$$\tau_s = M \times \alpha_s \times f(RH), \tau_a = M \times \alpha_a \tag{4}$$

where M is the column burden of aerosol (unit: gm^{-2}), α_s is the mass scattering efficiency (MSE), and α_a is the mass absorption efficiency (MAE). The direct radiative forcing is usually calculated with the assumption that the absorption enhancement is negligible, in comparison to the aerosol scattering enhancement (Xia et al., 2023).

Hence, the dependence of ADRF on RH (i.e., $f_{RF}(RH)$) can be estimated by equation (5) (Chylek and Wong, 1995; Kotchenruther et al., 1999; L. Zhang et al., 2015):

230
$$f_{RF}(RH) = \frac{\Delta F_R(RH)}{\Delta F_R(dry)} = \frac{(1 - R_s)^2 \times \beta(RH) \times \alpha_s \times f(RH) - 2 \times R_s \times \alpha_a}{(1 - R_s)^2 \times \beta(dry) \times \alpha_s \times f(dry) - 2 \times R_s \times \alpha_a}$$
(5)

where the constant parameters used were $R_s = 0.15$, $\alpha_a = 0.3 \text{ m}^2 \cdot \text{g}^{-1}$ (Hand and Malm, 2007; Fierz-Schmidhauser et al., 2010). It should be noted that the assumed constant α_a might introduce some uncertainty in the calculated $f_{RF}(RH)$, given the fact that the contribution of absorption by brown carbon was unknown, although the mass fraction of BC in TSP remained almost constant (i.e., $4.6\% \pm 1.1\%$, Fig. S3) during the observation period. The parameter α_s was calculated by dividing $\sigma_{sca, 525}$ in the dry condition by the mass concentration of PM_{2.5} (i.e., $\alpha_s = \sigma_{sca, 525}$ / PM_{2.5}). β could be calculated empirically from the measured HBF: $\beta = 0.0817 + 1.8495 \times \text{HBF} - 2.9682 \times \text{HBF}^2$ (Delene and Ogren, 2002).

3 Results and discussion

3.1 Overview of the aerosol optical hygroscopicity and PNSD measurements

Figure 1 displayed the time series of the measured aerosol scattering coefficients, f(RH), PNSD, and the corresponding meteorological conditions and air pollutants during the study period. A sharp decrease in aerosol scattering coefficients and PM_{2.5}, accompanied with the continuous excellent visibility over 20 km was observed after August 6, indicating a markedly cleaner environment during P2 in comparison to P1 in summer 2022 of Chongqing. This could be largely attributed to the reduction in anthropogenic emissions (e.g., NO₂, CO, except SO₂) from limited outdoor activities

influenced by the heatwaves in P2, as well as partly suspended industries and transportation to alleviate the power shortage issue (Chen et al., 2024). Notably, the increased wind speed and enhanced mixing layer height (MLH) also enabled a more favorable atmospheric diffusion condition in P2, facilitating the dilution of surface air pollutants (Zhang et al., 2008). However, a higher mass concentration of SO₂ was observed in the P2 period, likely due to a surge in electricity demand and resulted higher emissions from power plants operating almost at full capacity during the heatwave (Su, 2021; Teng et al., 2022). Moreover, significant discrepancies in the aerosol optical and hygroscopic properties were observed under different synoptic conditions (Table S2). Both HBF and SAE were higher during the P2 period, aligning with the smaller R_{eff} (Table S2). The f(RH) was found to be relatively higher (p < 0.05) in heatwave days, with the mean values of 1.61 ± 0.12 and 1.71 ± 0.15 during the P1 and P2 periods, respectively. Differently, ALWC was more abundant during the normally hot P1 period than the heatwave-dominated P2 period. This is likely due to that the derivation algorithm of ALWC utilized in this study (Kuang et al., 2018) was partly dependent on (e.g., positively correlated) the dry aerosol scattering coefficient, or rather the aerosol volume concentration in the dry condition (refer to Sect. S3 and Fig. S11 of the supplement). The mean $\sigma_{sca, 525}$ for P2 was about 46.8% of that for the P1 period, and the corresponding mean level of ALWC was approximately 55.8% of that for P1. This partly agrees with the stronger aerosol optical hygroscopicity with a marginally higher f_W during the P2 period, highlighting a complex interaction between the optical enhancement and aerosol physicochemical properties.

249

250

251

252

253

254

255

256

257

258

259

260

261

262

263

264

265

266

267

268

269

270

271

272

273

274

275

276

277

278

The particle number size distribution data suggested that NPF events appeared in about half the number of observation days (Fig. 1i), with an overall occurrence frequency of 52.4% (Fig. S4a). This suggests the rather frequent summer NPF events in Chongqing, notably higher than those observed in other regions of the world, e.g., Beijing (16.7%, Deng et al., 2020; ~20%, Wang et al., 2013), Dongguan (4%, Tao et al., 2023), Hyytiälä (<40%, Dada et al., 2017) and LiLLE (<20%, Crumeyrolle et al., 2023). Moreover, the frequent NPF events during heatwaves formed substantially ultrafine particles that are of less contribution to aerosol optical properties in

comparison to large particles (Fig. S13), partially explaining the significantly lower levels of total scattering coefficients observed during the P2 period. It should be noted that the hourly $\sigma_{sca, 525}$ values during the P2 period were exclusively below 100 Mm⁻¹ (approximately the last 10^{th} percentile of $\sigma_{sca, 525}$ data, regarded as the threshold value of relatively polluted cases; Fig. S2c), suggesting a much cleaner environment compared to the relatively polluted P1 period. Correspondingly, NPF events occurring during the relatively polluted P1 period (as detailed in section 3.2) were defined as NPF_{polluted}, while cases during the cleaner and heatwave-dominated P2 period were classified as NPF_{clean, HW}.

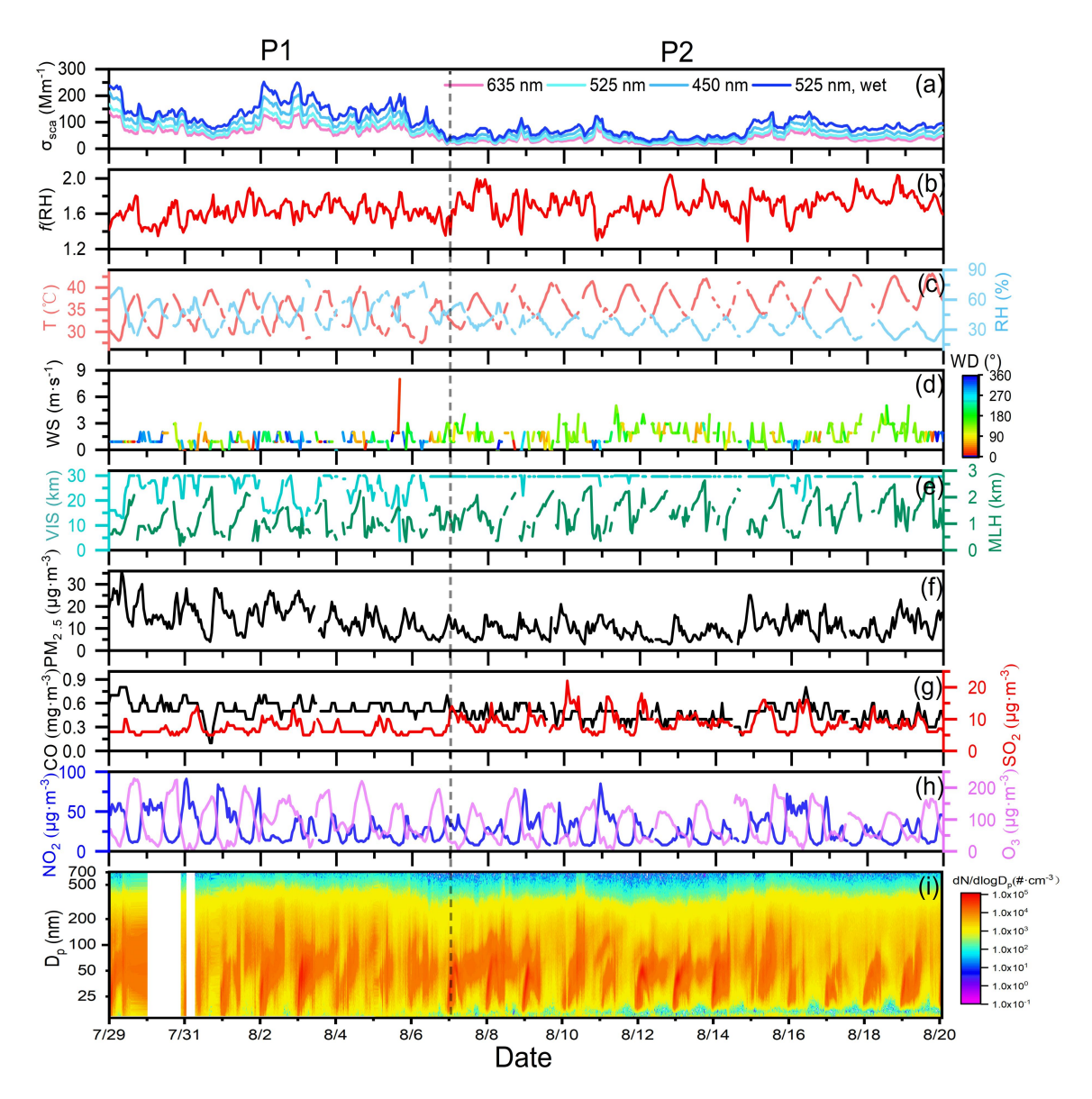


Figure 1. Time series of the measured aerosol scattering coefficients, f(RH), meteorological conditions, air pollutants, and particle number size distribution during the study period.

3.2 Characteristics of NPF events in different periods

Aside from gaseous precursors (e.g., SO₂, volatile organic compounds), meteorological conditions also play a key role in the occurrence of NPF events. In brief, NPF events are more likely to appear under sunny and clean conditions (Bousiotis et al., 2021; Crumeyrolle et al., 2023; Deng et al., 2021; Wang et al., 2017). The backward trajectory analysis revealed that the southerly breeze was predominant during the study period (Fig. S4b). Although the surface wind vector slightly varied between the P1 and P2 periods, this consistency in air mass origins suggests that some other factors (e.g., changes in environmental conditions and emissions of gaseous precursors under heatwaves) could have played a crucial role in modulating NPF events. To further explore the characteristics of NPF events in different periods, the time-averaged diurnal variations of meteorological parameters and air pollutant concentrations during both NPF events and non-event days are presented in Fig. 2.

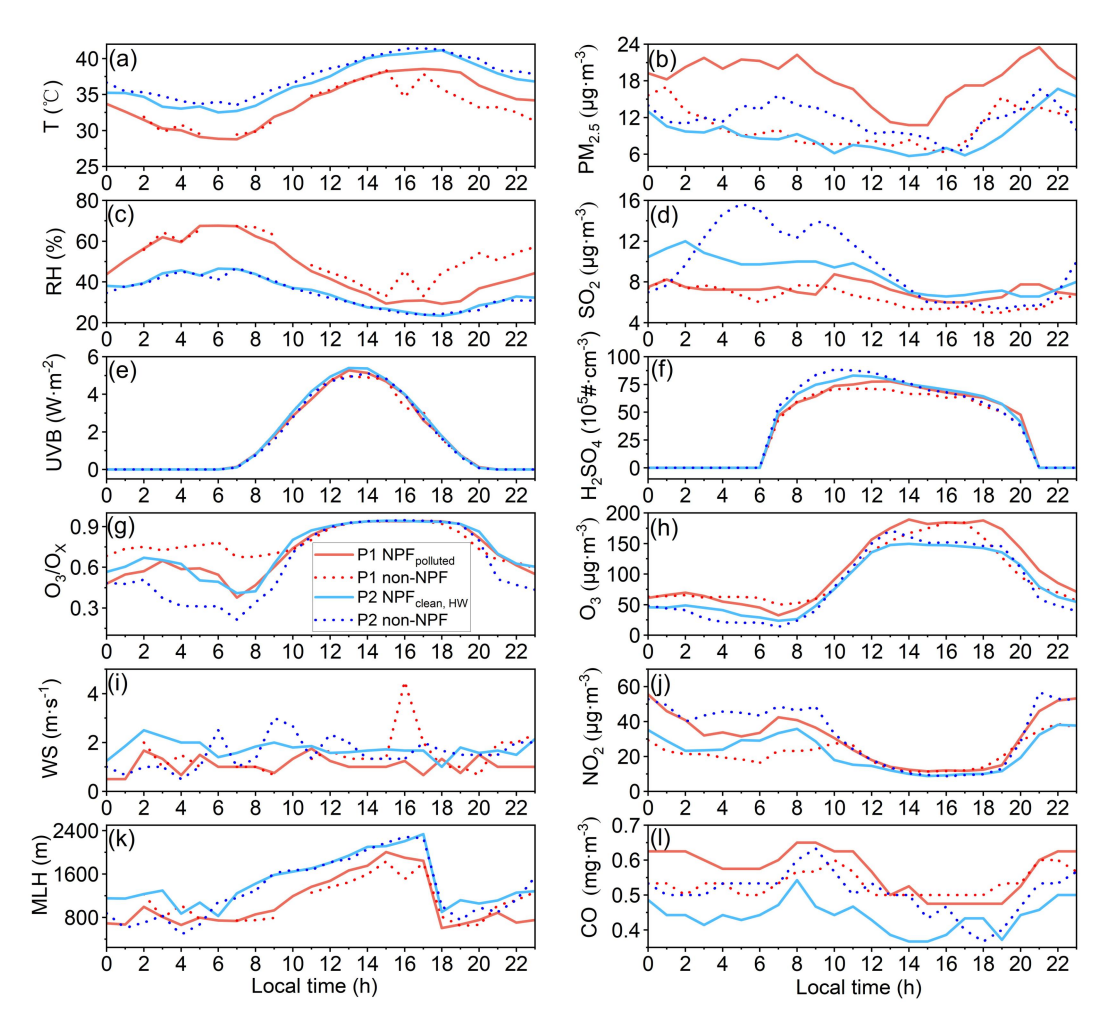


Figure 2. Diurnal variations of temperature (a), PM_{2.5} mass loading (b), RH (c), SO₂ (d), UVB (e), H₂SO₄ (f), O₃/O_X (g), O₃ (h), WS (i), NO₂ (j), MLH (k) and CO (l) during P1 (red) and P2 (blue) NPF days (solid line), as well as the corresponding non-event days (dash line).

As stated in Sect.3.1, NPF events during the P1 period tended to occur in relatively polluted environments compared to that of P2 NPF_{clean, HW} events, as evidenced by the frequent occurrence of $\sigma_{sca, 525} > 100$ Mm⁻¹, increased air pollutant concentrations and lower visibility levels during P1 (Table S2, Fig. 1). Additionally, the mean CS of the NPF_{polluted} events was above 0.015 s⁻¹ (Table S2), which could be considered as the "polluted" NPF cases (Shang et al., 2023). On P2 NPF_{clean, HW} days, the overall mean $\sigma_{sca, 525}$ was 33.2 \pm 11.7 Mm⁻¹, decreased by 68.0% (39.3%) in comparison to that for P1 NPF_{polluted} days (P2 non-event days). In addition, the mean PM_{2.5} concentration was even lower than 10.0 μ g·m⁻³, and the corresponding visibility

level was almost maintained at 30 km (Fig. 1e). All the above implies that the P2 NPF_{clean, HW} events were generally accompanied with a much cleaner environment. It is notable that the increase in SO₂ concentration after 9:00 LT (Fig. 2d), along with the significant decrease in PM_{2.5} mass loadings after 8:00 LT during P1 NPF_{polluted} events (Fig. 2b), likely favored the occurrence of NPF events. The higher gas-phase sulfuric acid (i.e., H₂SO₄, as estimated with the UVB and SO₂ concentration, Lu et al., 2019, Sect. S4) on the same NPF days (Fig. 2f), further suggesting that sulfuric acid concentration was a critical factor for the occurrence of P1 NPF_{polluted} events.

319

320

321

322

323

324

325

326

327

328

329

330

331

332

333

334

335

336

337

338

339

340

341

342

343

344

345

346

347

348

The diurnal evolutions of meteorological conditions (e.g., T, RH, MLH) for NPF events were distinct between P1 and P2 periods, although relatively insignificant differences were observed for both NPF days and non-event days within a same period (Fig. 2). This likely suggests that meteorological factors might not be the predominant determining factor of NPF occurrence during the heatwaves of 2022 summer in urban Chongqing, while NPF could be accompanied with quite different meteorological conditions depending on gaseous precursors and preexisting condensation sinks. For instance, the NPF_{clean, HW} events were typically of clean-type NPF, characterized with lower background aerosol loading, higher temperature and favorable atmospheric dispersion capacity with the higher MLH. However, it is reported that excessive heat can increase the evaporation rate of critical acid-base clusters during the nucleation process and reduce the stability of initial molecular clusters (Bousiotis et al., 2021; Kurtén et al., 2007; Zhang et al., 2012), in line with a recent study that NPF events were weaker during heatwayes in Siberian boreal forest due to the unstable clusters (Garmash et al., 2024). On the other hand, the emission rate of biogenic VOCs (BVOCs, e.g., isoprene, monoterpene) from nearby plants and trees would decrease when temperature exceeded around 40 °C (Guenther et al., 1993; Pierce and Waldruff, 1991), despite that BVOCs plays a key role in the nucleation mechanism of NPF (Wang et al., 2017; Zhang et al., 2004). Hence, the even higher temperature (e.g., T >40 °C) likely suppressed the nucleation processes and the subsequent growth of nucleation mode particles on P2 non-event days (Fig. S6b2), in spite of higher concentrations of SO₂ and H₂SO₄.

To further investigate the effect of heatwave on NPF events, the diurnal variations of PNSD, R_{eff} and particle mode diameter (D_{mode}) were shown in Fig. S6. Aerosol number and volume concentrations, as well as Reff, for different modes were illustrated in Figs. S7-8, and the relationship between temperature and the duration of NPF events was displayed in Fig. S9. Distinct particle size distributions were observed for different NPF event days. While the number concentrations of Aitken mode particles (N_{Ait.}) were comparable during NPF days of both periods, the corresponding number concentration of nucleation mode (N_{Nuc.}) was significantly higher on P1 NPF_{polluted} days (1880.8 \pm 2261.5 cm⁻³) than that for P2 NPF cases $(1132.0 \pm 1333.5 \text{ cm}^{-3})$ (Fig. 1i, Fig. S7). Different from that of the P1 NPF_{polluted} cases, the P2 NPF_{clean, HW} event did not start from the minimum size, and t The reduced N_{Nuc}. during P2 period was likely attributed to the influence of transport on the local nucleation and growth process (Fig. S4; Cai et al., 2023; Lee et al., 2019). Namely, some nucleation mode particles transported from upwind regions or from the mixing layer downwards had undergone atmospheric aging thereby a certain degree of growth upon arrival (Cai et al., 2023; Lai et al., 2022; Platis et al., 2016), resulting in relatively lower concentrations of smaller-sized particles than the case of locally formed. However, the local formation of sub-25 nm particles and the continuous growth process were still distinctly observed under heatwaves (Fig. 1i, Figs. S6, S15). However, tThe NPF events under heatwaves usually initiated earlier (Fig. S9), with the N_{Nuc} in P2 NPF_{clean}, HW cases peaked about an hour earlier in comparison to NPF_{polluted} days (Fig. S8a). The D_{mode} on P2 NPF_{clean}, HW days also reached its minimum earlier than that on P1 NPF_{polluted} days (Fig. S6). Since the sunrise and sunset time did not significantly vary within the study period (i.e., less than a half hour discrepancy), heatwaves likely provided more favorable conditions (e.g., enhanced volatile gaseous emissions, low RH; Bousiotis et al., 2021; Hamed et al., 2007; Wang et al., 2024) for the occurrence of NPF events in urban Chongqing. This is supported by the earlier start time of NPF_{clean, HW} corresponding to higher temperature ranges (Fig. S9). Furthermore, the end time of subsequent particle growth during P2 period was even later (i.e., ~ 21:00 LT) than that of P1 cases (Fig. S9).

349

350

351

352

353

354

355

356

357

358

359

360

361

362

363

364

365

366

367

368

369

370

371

372

373

374

375

376

377

Given that the growth rates of new particles were generally lower during P2 NPF_{clean}, HW events (Table S2), these explosively formed new particles could persist longer in the warmer atmosphere and probably undergo aging processes with a relatively higher oxidation degree. This is supported by the commonly higher ratios of secondary organic carbon (SOC) to organic carbon (OC) (i.e., SOC/OC >0.5) during the NPF_{clean}, HW days (Fig. S3b). In addition, aerosol Reff was significantly smaller on the NPFclean, HW days under heatwave conditions. The Reff and D_{mode} nearly kept at a same level below/approaching 50 nm during the subsequent growth on the P2 NPF_{clean, HW} days, while the Reff was generally above 50 nm and larger than D_{mode} for both P1 NPF_{polluted} cases and non-event days (Fig. S6). The diurnal patterns of aerosol volume concentrations for different size modes were similar to that of aerosol number concentrations during NPF events (Fig. S8b1-b3). However, both the Reff of Aitken mode particles (R_{Ait.}) and accumulation mode particles (R_{Acc.}) were smaller during P2 NPF_{clean, HW} events than that of P1 NPF_{polluted} events (Fig. S8c2-c3), which may further influence size-dependent aerosol optical and hygroscopic properties (e.g., $\sigma_{sca, 525}$, HBF, SAE, f(RH)). The decrease in R_{Ait.} and R_{Acc.} during heatwaves could be attributed to three factors: (1) evaporation of the outer layer of particles and unstable clusters due to heatwaves (Bousiotis et al., 2021; Cusack et al., 2013; Deng et al., 2020; Garmash et al., 2024; Li et al., 2019); (2) lower FR and GR of particles under the cleaner environment (Table S2); (3) reduced emissions of larger primary particles during the P2 period.

379

380

381

382

383

384

385

386

387

388

389

390

391

392

393

394

395

396

397

398

399

400

401

402

403

404

405

406

407

3.3 Characteristics of the aerosol optical and hygroscopic properties on different types of NPF days

Diurnal variations of the aerosol optical and hygroscopic parameters during different NPF days were shown in Fig. 3, and the corresponding results for non-event days can refer to Fig. S10. Generally, σ_{sca} , 525 possessed a similar bimodal diurnal pattern to that of the accumulation mode aerosol volume concentration (V_{Acc.}) (Fig. S8b3), as supported by the positive correlation between σ_{sca} , 525 and SMPS-measured aerosol volume concentration (Fig. S12). This is also consistent with the Mie theory,

with a stronger increase in the scattering efficiency for accumulation mode particles (Titos et al., 2021). The diurnal pattern of $\sigma_{sca, 525}$ also varied distinctly between different NPF days. Specifically, a minor peak of $\sigma_{sca, 525}$ around 12:00 LT (Fig. 3a) was influenced by the newly formed particles during P2 NPF_{clean, HW} events, which contributed more significantly to the aerosol number and volume concentrations within 100 nm size ranges in markedly clean environments (Fig. S5c1, c2). Instead of a noontime peak, $\sigma_{sca, 525}$ was observed with an early peak around the morning rush hours and a maximum value similarly occurred at the nighttime on P1 NPF_{polluted} days.

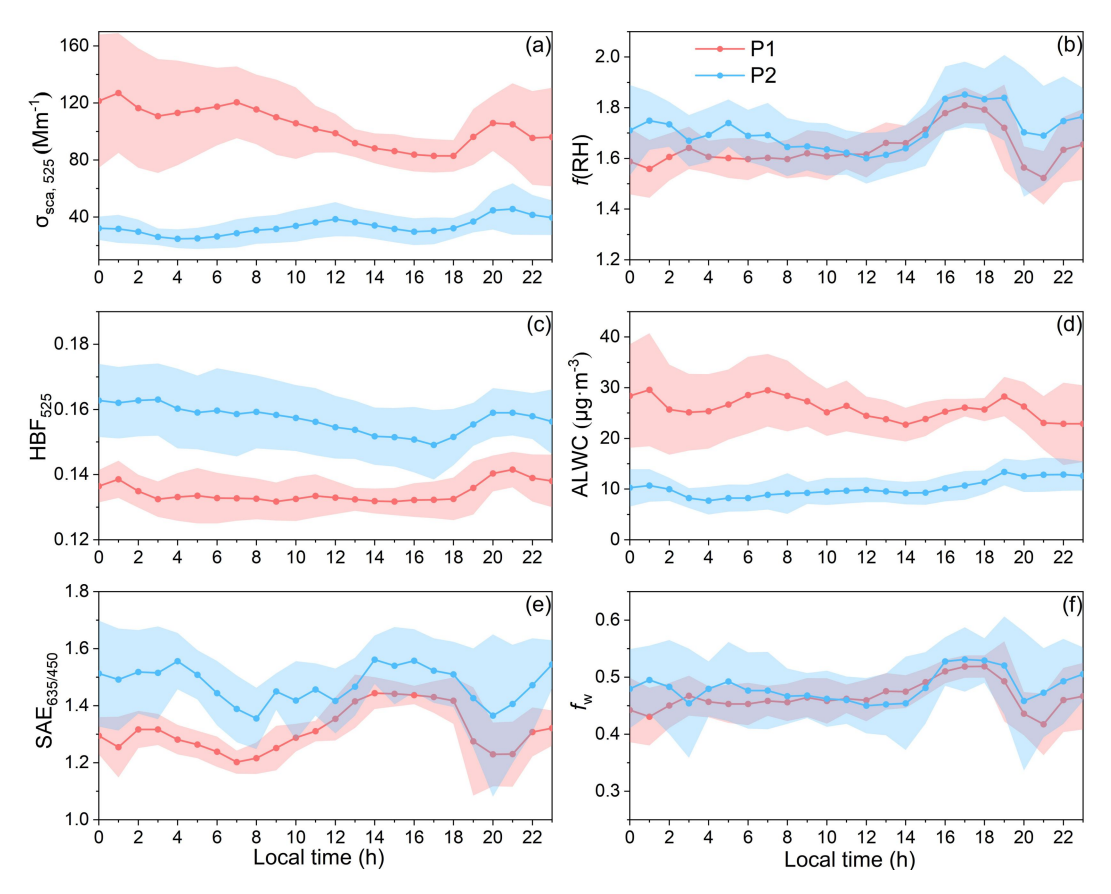


Figure 3. Diurnal variations of $\sigma_{sca, 525}$ (a), f(RH) (b), HBF₅₂₅ (c), ALWC (d), SAE_{635/450} (e) and f_W (f) on NPF days during P1 (red line) and P2 (blue line) periods. The shaded areas stand for the corresponding $\pm 1\sigma$ standard deviations.

Both HBF and SAE on P2 NPF_{clean, HW} days were significantly higher than that of P1 NPF_{polluted} cases (Fig. 3c, e), largely due to the smaller R_{eff} observed during heatwave-dominated period (Table S2). Moreover, the correlation between HBF (or SAE) and particle size in each mode was weaker on NPF days than on non-event days,

especially for NPF_{clean, HW} days (Fig. S14). A strongest negative correlation was found between HBF and R_{eff} of the accumulation mode in comparison to other modes, highlighting that HBF is more sensitive to the size distribution of accumulation mode particles (Collaud Coen et al., 2007). Given that NPF would largely enhance the abundance of both nucleation and Aitken mode aerosols (Fig. S7), no significant variation in HBF was observed during the daytime due to the weakened correlation between HBF and R_{Acc.} of NPF events. SAE is commonly used as an indicator of particle size distribution, almost decreasing monotonously with the increase of aerosol size within 1 µm (Kuang et al., 2017, 2018; Luoma et al., 2019). Accordingly, SAE decreased over the morning and evening rush hours when coarse particles (e.g., aged particles, road dust, automobile exhaust) generated during anthropogenic activities, accompanied with an increase in CO that is taken as the proxy for primary emissions (Fig. 21) (Yarragunta et al., 2020). On the contrary, the abundant ultrafine particles formed during NPF events led to a continuous increase in SAE during the day.

f(RH) exhibited a similar diurnal pattern on the P1 and P2 NPF days (Fig. 3b). During the daytime, f(RH) remained relatively stable and gradually increased until peaking around 16:00-18:00 LT, with a generally higher f(RH) particularly after 15:00 LT during P2 NPF_{clean, HW} days than that of P1 cases. The insignificant fluctuation of relatively lower f(RH) levels before the noon could be attributed to the continuous development of the mixing layer (Fig. 2k), leading to an efficient mixing of particles in the nocturnal residual layer with anthropogenic emissions near the ground. Additionally, photochemical reactions in the afternoon facilitated the formation of more hygroscopic secondary aerosols with a higher oxidation level (Liu et al., 2014; R. Zhang et al., 2015). The diurnal patterns of O₃ and the O₃/O_X ratio (i.e., an indicator of atmospheric oxidation capacity, where $O_X = O_3 + NO_2$, Tian et al., 2021) also showed similar trends (Fig. 2g, 2h). The presence of black carbon (BC) mixed with organic compounds (e.g., from traffic emissions and residential cooking activities) explained the rapid decrease in f(RH) during the evening rush hours (Liu et al., 2011). Furthermore, the daily mean f(RH) for NPF days was higher than that of non-event days (Table S2), particularly after the ending of NPF events around 12:00

LT. Given that newly formed particles were too small to significantly impact the total light scattering (Fig. S11a), this indicates that the atmospheric conditions conducive to the occurrence of NPF may promote further growth (e.g., via photooxidation or atmospheric aging processes) of pre-existing particles and newly formed ones, leading to enhanced aerosol optical hygroscopicity as clued from the concurrent variations of ALWC and f_W in urban Chongqing during hot summer (Asmi et al., 2010; Wang et al., 2019; Wu et al., 2016). The diurnal pattern of ALWC closely mirrored the variation in $\sigma_{sca, 525}$, while f_W followed the similar evolution of f(RH). This suggests that ALWC was more sensitive to changes in the aerosol volume concentration, as determined by the corresponding retrieval algorithm (Kuang et al., 2018). The f_W levels were slightly higher during NPF days in comparison to that of non-event days (Table S2). This difference was more pronounced in the afternoon of NPF days (e.g., even exceeded 50%; Fig. 3f), verified the enhancement of aerosol hygroscopicity during the subsequent growth and atmospheric aging of both pre-existing and newly formed particles.

3.4 Heatwave-induced divergent changes in aerosol optical hygroscopicity

To further explore the impacts of heatwaves on *f*(RH) during diverse NPF events, data mainly within the time window of 08:00-22:00 LT (i.e., typically covered the complete process of NPF and subsequent growth, while excluded higher RH conditions at night) were utilized for the following discussion.

Although ultrafine particles exhibited higher number concentrations during the study period, accumulation mode particles dominated the aerosol volume concentration and contributed predominantly to the total light scattering (Figs. S7, S13). A positive correlation between f(RH), $R_{\rm eff}$ and the volume fraction of accumulation mode particles (VF_{Acc.}) was found on non-event days (Fig. 4c-d), when the aerosol size distribution was undisturbed by newly formed ultrafine particles and the corresponding VF_{Acc.} maintained around a high level of 0.95 (Fig. 4a-b). The notably positive correlation between f(RH) and $R_{\rm eff}$ could be linked to the secondary formation of hygroscopic particles within the accumulation mode, primarily via

photochemical reactions and further intensified by heatwaves during the non-event day particularly of the P2 period (Gu et al., 2023; Liu et al., 2014; R. Zhang et al., 2015; Zhang et al., 2024). Consequently, f(RH) at a specific $R_{\rm eff}$ was generally higher during the P2 period in comparison to that of P1 (Fig. 4c-d), also with high f(RH) levels observed for smaller size cases of $R_{\rm eff}$ <110 nm under some extremely high temperature conditions (T >40 °C, as highlighted by the red dashed circle in Fig. 4d). The higher SOC/OC on P2 non-event days further demonstrated the stronger secondary aerosol formation in comparison to P1 non-event days (Fig. S3b).

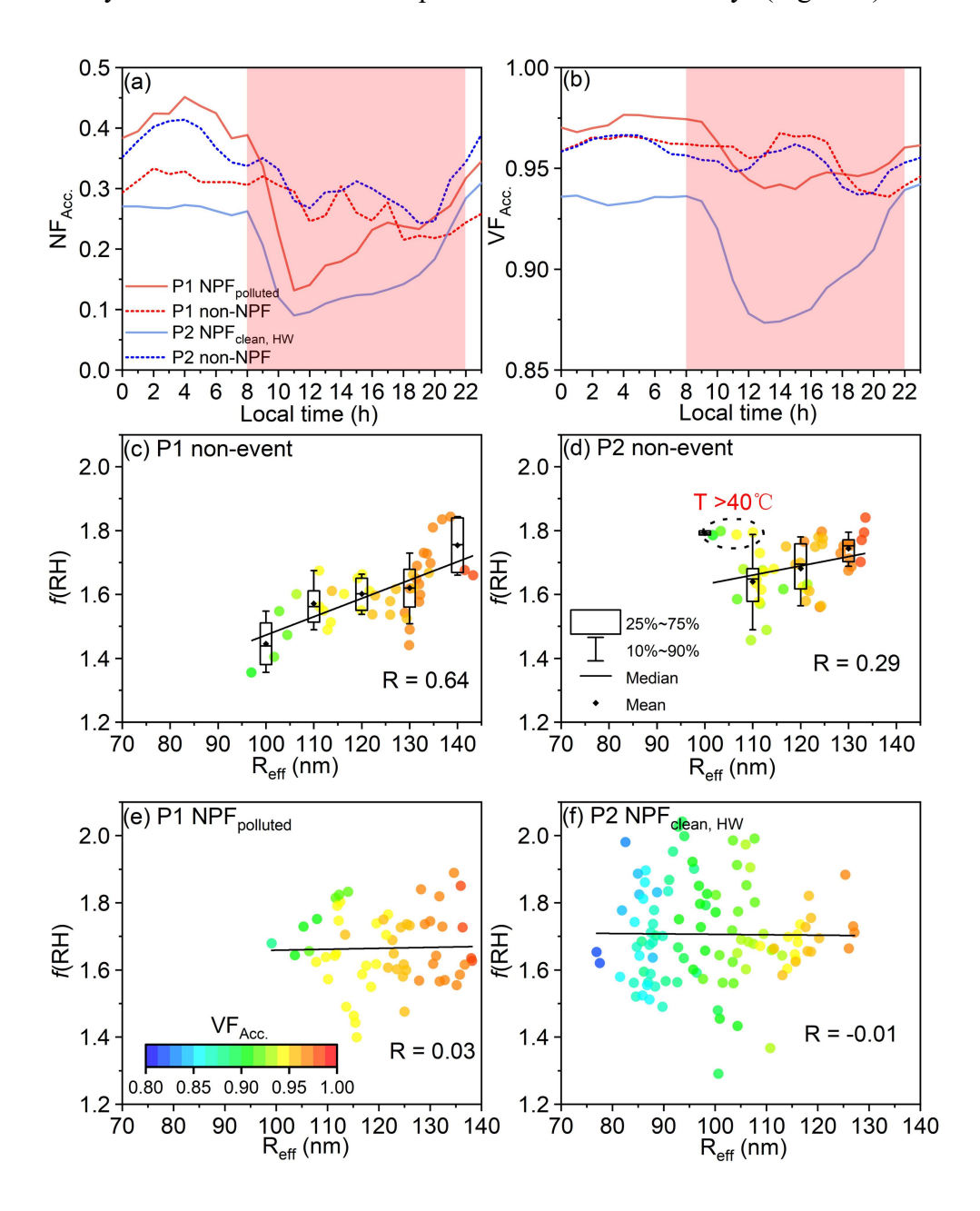


Figure 4. Diurnal variations of **(a)** the number fraction (NF_{Acc.}) and **(b)** volume fraction of accumulation mode particles (VF_{Acc.}) on P1 (red) and P2 (blue) NPF days (solid line), as well as non-event days (dash line). The time window of 08:00-22:00 LT was shaded in red. The relationship of *f*(RH) with R_{eff} and VF_{Acc.} (as indicated by the colored dots) on P1 **(c)** and P2 non-event days **(d)**, as well as on P1 **(e)** and P2 **(f)** NPF days during the 08:00-22:00 LT time window.

492

493

494

495

496

497

498

499

500

501

502

503

504

505

506

507

508

509

510

511

512

513

514

515

516

517

518

519

520

Nevertheless, f(RH) was almost independent of the two parameters (i.e., R_{eff} and VF_{Acc.}) for NPF events (Fig. 4e-f). This is mainly due to the explosive formation of ultrafine particles and subsequent growth on NPF days, significantly altering aerosol size distributions and inducing large fluctuations in the NF_{Acc.} and VF_{Acc.} in comparison to that on non-event days, especially during the P2 periodnumber and volume fractions of accumulation mode particles (as shaded in Fig. 4a-b). Therefore, characterizing f(RH) with the corresponding R_{eff} of aerosol populations was no longer applicable. Alternatively, SAE was commonly used to estimate or parameterize f(RH) (Titos et al., 2014; Xia et al., 2023; Xue et al., 2022), in line with the similar diurnal patterns of f(RH) and SAE observed in this study. Figure 5 demonstrated a significantly positive correlation between f(RH) and SAE during NPF days in comparison to non-event days, with a similar slope of approximately 0.65 suggesting the consistent variation of f(RH) with SAE across both periods. As larger particles contributed higher to the aerosol volume concentrations (Fig. S5), the decrease of SAE also corresponded to an increase in $\sigma_{sca, 525}$ (Fig. 5a3, b3). Given that larger $\sigma_{\text{sca}, 525}$ values typically indicate the condition of a higher aerosol loading, f(RH)increased with SAE whereas decreased with $\sigma_{sca, 525}$, or rather the pollution level, during NPF days. The cleaner environment of P2 period may further favor the occurrence of NPF events. Both f(RH) and SAE exhibited a higher level on P2 NPF_{clean, HW} days (as shown by the dash lines in Fig. 5), likely attributed to the following two aspects. One is related to the smaller aerosol Reff (with a larger SAE) due to the lower FR and GR, likely influenced by the evaporation of newly-formed unstable clusters and particle coatings under heatwaves (Bousiotis et al., 2021;

Cusack et al., 2013; Deng et al., 2020) during the subsequent growth of aerosols. 521 Secondly, the higher temperature was normally associated with stronger 522 photochemical oxidation, which could intensify the formation of secondary aerosol 523 components with a higher hygroscopicity (Asmi et al., 2010; Gu et al., 2023; Liu et al., 524 2014; Wu et al., 2016; R. Zhang et al., 2015; Zhang et al., 2024). This is further 525 supported by the slightly higher levels of UVB (P1: $2.6 \pm 1.9 \text{ W} \cdot \text{m}^{-2}$ versus P2: $2.7 \pm 1.9 \text{ W} \cdot \text{m}^{-2}$ 526 2.0 W·m⁻²) and O_3/O_X (P1: 0.81 ± 0.17 versus P2: 0.82 ± 0.17) during P2 heatwave 527 528 days, also in line with a recent study which demonstrated that heatwaves affected secondary organic aerosols (SOA) formation and aging by accelerating 529 photooxidation in Beijing (Zhang et al., 2024). 530 It is worth noting that f(RH) did not show a consistently higher level after the 531 NPF_{clean, HW} occurrence during P2 period, and it was slightly higher within the first 532 few hours of NPF occurrence (i.e., ~ 12:00 -15:00 LT) on P1 NPF_{polluted} days (Fig. 3b). 533 In fact, aerosol optical hygroscopicity not fully corresponds to the bulk hygroscopicity 534 primarily determined by aerosol chemical components, and the variability in aerosol 535 536 optical features also plays a key role in f(RH). Hence, the size-dependency of aerosol optical properties should be considered. The size-resolved $\sigma_{sca, 525}$ distribution and 537 size-resolved cumulative frequency distribution (CFD) of $\sigma_{sca, 525}$ over different NPF 538 days were calculated using the Mie theory, with good agreements between the 539 theoretically calculated and measured $\sigma_{sca, 525}$ values (R² = 0.99). As shown in Fig. 540 S11a and Fig. S13, new particles must grow into the accumulation mode size at least 541 542 before they can exert a significant influence on the total scattering coefficient. The critical sizes corresponding to the cumulative frequency of 50% in $\sigma_{sca, 525}$ were 358.7 543 544 nm and 333.8 nm on P1 and P2 NPF days, respectively. This indicates that relatively smaller particles including the newly formed and grown ones mixed with pre-existing 545 and aged particles contributed a slightly higher portion to σ_{sca, 525} on P2 NPF_{clean, HW} 546 days, while the $\sigma_{sca, 525}$ was mainly contributed by larger ones on P1 NPF_{polluted} days. 547 548 Nevertheless, the Mie theory suggests that these smaller particles generally have a 549 weaker enhancement in total scattering after hygroscopic growth, in comparison to larger size particles (Collaud Coen et al., 2007, Fig. S11a). Consequently, the changes 550

in aerosol optical and hygroscopic properties necessitate consideration of both aerosol optical and chemical characteristics during different NPF events. Newly formed ultrafine particles contributed minor to aerosol optical properties, resulting in a lower f(RH) during the initial hours of P2 NPF_{clean}, HW events compared to that of P1 NPF_{polluted} events (Fig. 3b), as evidenced by a smaller R_{eff} for P2 NPF_{clean}, HW events (Fig. S6). In contrast, the growth of pre-existing and newly formed particles into larger sizes would subsequently affect bulk aerosol optical properties, which was evidenced by the enhancement in aerosol extinction coefficient observed after NPF occurrence in a recent study (Sun et al., 2024). Specifically, particles could undergo a longer and more intensified photochemical aging process during NPF_{clean}, HW events as influenced by persistent heatwaves, which facilitated the secondary formation of hygroscopic aerosols and resulted in a higher f(RH) after 15:00 LT (Fig. 3b).

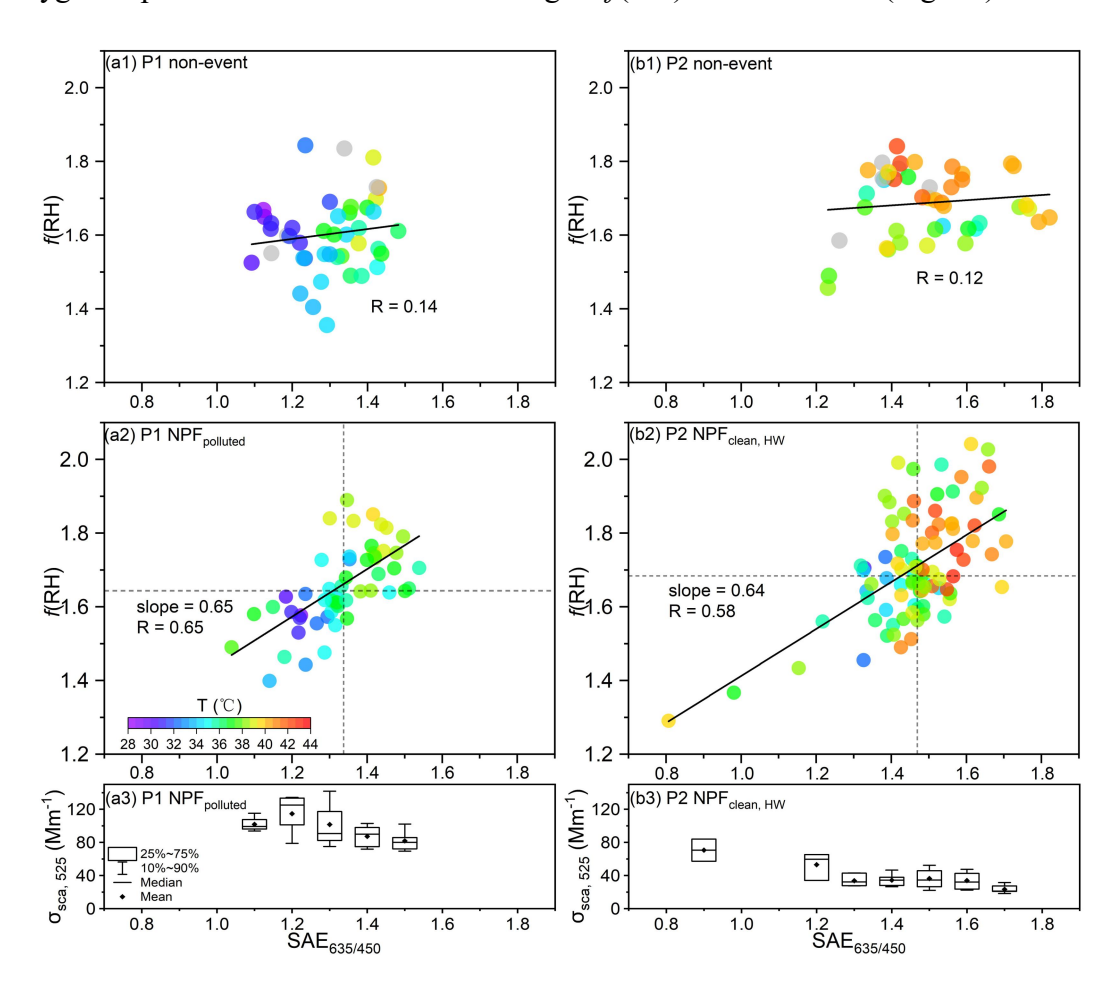


Figure 5. The relationship between f(RH) and $SAE_{635/450}$, as well as temperature (as indicated by the color of dots, missing values are represented in gray), on P1

- non-event days (a1), NPF_{polluted} days (a2) during the 08:00-22:00 LT time window.
- The vertical (horizontal) dash line represents the median value of $SAE_{635/450}$ (f(RH)).
- 568 (a3) The corresponding $\sigma_{sca, 525}$ under different SAE_{635/450} levels on P1 NPF_{polluted} days.
- **(b1-b3)** The same but for P2 period.

3.5 f(RH)-induced changes in aerosol direct radiative forcing

The changes in f(RH) have significant implications for aerosol direct radiative forcing. Despite considerably lower $\sigma_{sca, 525}$ results during heatwaves, the corresponding mean $f_{RF}(RH)$ levels particularly for P2 NPF_{clean, HW} days were higher than that of the P1 cases (Fig. 6a). A robust positive correlation ($R^2 = 0.68$) was observed between f(RH) and aerosol radiative forcing enhancement factor, $f_{RF}(RH)$ (Fig. 6b). This is likely attributed to the enhanced $f_{RF}(RH)$ with the larger forward scattering ratio β , or rather higher HBF for smaller particle sizes, as supported by a generally negative correlation between $f_{RF}(RH)$ and $f_{RF}(RH)$ and $f_{RF}(RH)$ value of $f_{RF}(RH)$ value of $f_{RF}(RH)$ and smallest $f_{RF}(RH)$ and smallest $f_{RF}(RH)$ of the entire study period.

The definition of $f_{RF}(RH)$ in Eq.(5) implies the dependences of $f_{RF}(RH)$ on both f(RH) and HBF-derived $\beta(RH)$ and $\beta(dry)$, or rather the ratio of HBF₅₂₅, RH/HBF₅₂₅. The mean HBF₅₂₅, RH was generally larger than HBF₅₂₅ in this study, specifically with the HBF₅₂₅, RH/HBF₅₂₅ ratios centered around 1.8 and even approached 2.5 on P2 NPF_{clean}, HW days (Fig. 6c, Table S2). This could be different from the classical Mie theory with the spherical-particle premise, i.e., the observed light backscattering was enhanced after hydration likely resulted from the evolution in particle morphology that significantly influences their optical properties (Mishchenko 2009). Additionally, the predominant organic components when heterogeneously mixed with diverse chemical compositions (e.g., inorganics and black carbon) likely introduced the heterogeneity in aerosol hygroscopicity (Yuan and Zhao, 2023), which may alter particle morphology thereby optical properties upon water uptake (Giordano et al., 2015; Tan et al., 2020; Tritscher et al., 2011). The efficient evaporation of organic coatings under extremely hot conditions could also contribute to the change in particle

morphology (e.g., non-spherical inregular shapes) upon humidification, as evidenced by a recent study that high temperature conditions could accelerate the evaporation rate of SOA (Li et al., 2019). Given that the backward scattering intensity of non-spherical particles is suggested to be much larger than its spherical counterparts at scattering angles between 90° and 150° (Mishchenko 2009; Yang et al., 2007) and that the HBF-derived asymmetry parameter (g) normally correlates positively with the aerosol forward scattering (Andrews et al., 2006; Marshall et al., 1995), the generally smaller g_{RH} results (in comparison to g) confirmed the decrease (increase) in the forward (backward) light scattering after water uptake (Fig. S11c), likely implying the change in the morphological structure of particles. This is particularly evident for P2 NPF_{clean, HW} days, with a much lower level of g_{RH} was observed (Fig. S11c). Another possible reason is the distinct size dependences of both light scattering and backscattering efficiencies (Fig. S11a), with much more significant enhancements in the backscattering efficiency thereby HBF specifically of accumulation mode particles after hygroscopic growth (Fig. S11b). As reflected by the Mie model, although the abundant newly formed particles were generally optically-insensitive (e.g., below 100 nm), their contributions to $\sigma_{sca, 525}$ and especially to $\sigma_{bsca, 525}$ could be amplified upon humidification (Fig. S11b). Besides, the shift of size distribution towards larger accumulation-mode particles could also result in a significant elevation in HBF₅₂₅, RH/HBF₅₂₅ ratios, especially under the condition of a smaller mode diameter and narrower distribution of ultrafine-mode particles (e.g., during NPF events) (Fig. S156a1-b2 for the theoretical sensitivity tests of Sect. S9 in the supplement). Furthermore, the HBF₅₂₅, RH/HBF₅₂₅ ratio exhibited a significant positive correlation with the real part of complex refractive index (n) of bulk aerosols (Fig. S167), and ntends to increase with the aging process of organic species (Moise et al., 2015; Zhao et al., 2021). In this sense, the evolution of both aerosol size distribution pattern and chemical compositions, combined with the heterogeneity in aerosol hygroscopicty, could potentially change particle morphology and optical properties (e.g., complex refractive index and elevated HBF_{525, RH}) particularly during heatwave-influenced NPF_{clean, HW} days, characterized with the smallest aerosol R_{eff} (102.8 \pm 12.4 nm)

595

596

597

598

599

600

601

602

603

604

605

606

607

608

609

610

611

612

613

614

615

616

617

618

619

620

621

622

623

(Figure. S6), lowest number concentration (1897.0 \pm 680.8 cm⁻³) and fraction (0.20 \pm 0.10) of accumulation mode particles, intensified photooxidation, and a higher SOC/OC ratio. The higher HBF₅₂₅, RH/HBF₅₂₅ ratios increased the HBF-derived β (RH)/ β (dry) levels, in combination of the elevated f(RH), further resulting in the highest f_{RF} (RH) observed during P2 NPF_{clean}, HW events. Given that previously observed HBF₅₂₅, RH was typically lower than HBF₅₂₅ (Titos et al., 2021; Xia et al., 2023; L. Zhang et al., 2015), the mean f_{RF} (RH) results of this study (f_{RF} (85%) = 2.05 \pm 0.24) were significantly higher than those observed in the Yangtze River Delta (f_{RF} (85%) = 1.5, L. Zhang et al., 2015), the North China Plain (f_{RF} (80%) = 1.6 \pm 0.2, Xia et al., 2023), and some other regions in the world (Titos et al., 2021, Fig. 6d). It should be noted that the reported f_{RF} (RH) for the UGR site (Spain) was even higher, likely due to the higher R_s and α_s used in the derivation of f_{RF} (RH) in that area (Titos et al., 2021).

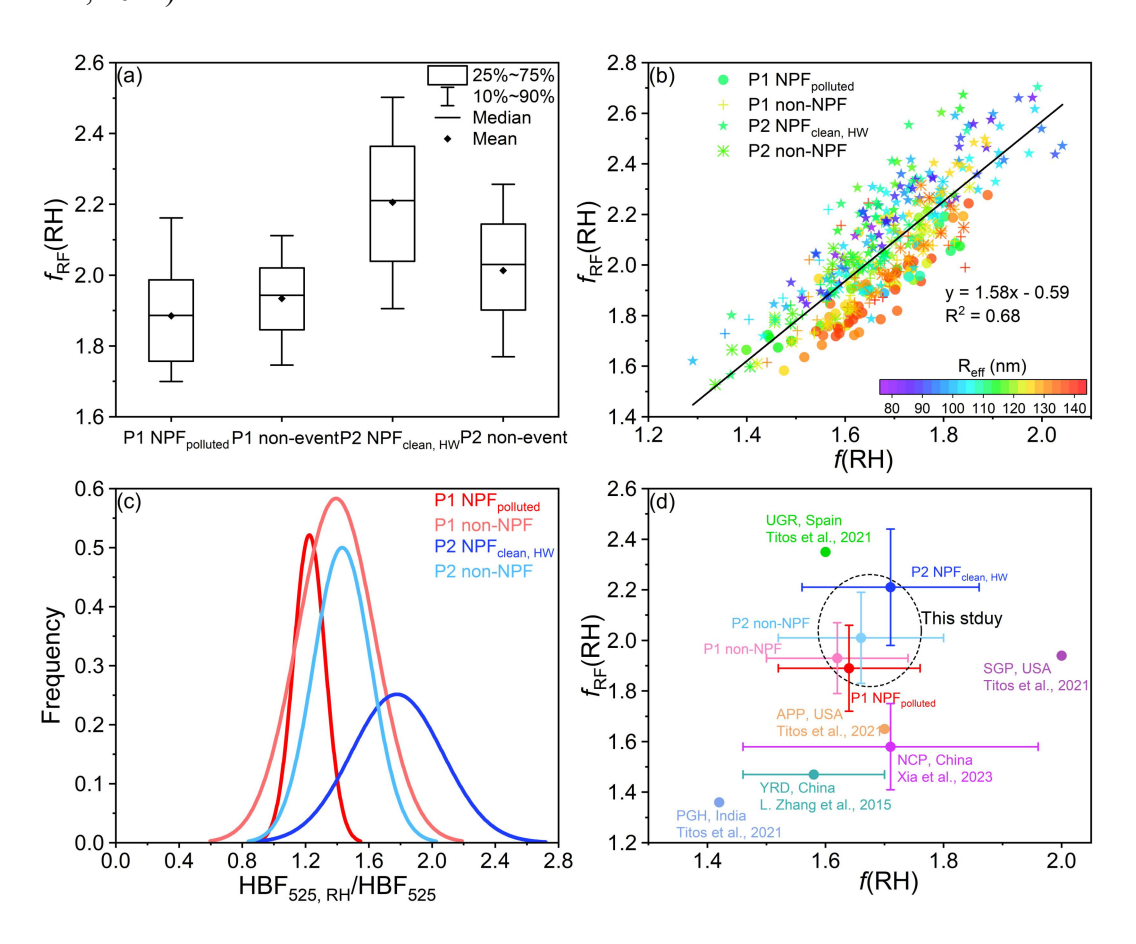


Figure 6. (a) The box-plot of $f_{RF}(RH)$ during P1 or P2 NPF event and non-event days. **(b)** The relationship between $f_{RF}(RH)$ and f(RH), as colored by the corresponding R_{eff} ,

during P1 or P2 NPF and non-event days (shown in different symbols). (c) Occurrence frequency of the HBF₅₂₅, RH/HBF₅₂₅ ratios during P1 or P2 NPF and non-event days. (d) The mean $f_{RF}(RH)$ under different f(RH) levels (the error bars stand for \pm one standard deviations corresponding to $f_{RF}(RH)$ and f(RH), respectively), along with the reported $f_{RF}(RH)$ and f(RH) data for other regions in the world.

641

642

643

644

645

646

647

648

649

650

651

652

653

654

655

656

657

658

659

660

661

662

663

664

665

666

667

668

669

A recent study has indicated that continuous reduction of PM_{2.5} mass loadings can increase the net solar radiation, thereby promoting NPF events (Zhao et al., 2021). Given the complexity and dynamic evolution of the atmospheric environment, these can further alter the intrinsic properties of aerosol particles (e.g., f(RH), HBF, morphology), potentially feeding back into aerosol-radiation interactions. Our findings suggest that NPF and growth events may elevate aerosol optical hygroscopicity in rather hot environments, e.g., the Basin area and tropical regions. Meanwhile, NPF serves as a crucial secondary transformation process in the atmosphere (Zhu et al., 2021). The favorable atmospheric diffusion capability ensured the mixing of newly formed particles into the upper boundary layer, where is colder and more humid than that near the surface during heatwaves (Jin et al., 2022). Hence, the enhancement of aerosol optical hygroscopicity during the subsequent growth of pre-existing and newly formed particles possibly exacerbates secondary pollution and even triggers haze events (Hao et al., 2024; Kulmala et al., 2021). On the other hand, a large number of studies have demonstrated that the new particles of higher hygroscopicity could contribute more to the activation of CCN (Ma et al., 2016; Ren et al., 2021; Rosati et al., 2022; Sun et al., 2024; Wu et al., 2015), thereby modulating the aerosol-cloud interactions and further the global climate (Fan et al., 2016; Merikanto et al., 2006; Westervelt et al., 2013). Additionally, the simultaneous decrease in aerosol effective radius and possibly evaporation-induced non-spherical particle morphology further enhance the aerosol direct radiative forcing enhancement factor, potentially amplifying the cooling effect mainly caused by light scattering aerosols. This highlights the needs for further in-depth exploration on aerosol radiative impacts at weather extremes (e.g., under heatwaves) with the changing

climate, given the continuous reductions of anthropogenic emissions and more intense emissions of biogenic origins with the global warming. Besides, more detailed information on the evolution of particle morphology with the changing environment (e.g., varied temperature and RH) would enrich insights into the aerosol radiative forcing.

4 Conclusions and implications

A rare heatwave event raged throughout urban Chongqing of southwest China in the summer of 2022, which significantly influenced aerosol physicochemical properties and atmospheric processes (e.g., NPF and subsequent growth). Concurrent measurements of aerosol optical and hygroscopic properties, PNSD, and bulk chemical compositions were conducted to explore the mechanisms behind the variations in aerosol optical hygroscopicity during different NPF days under diverse weather conditions.

Although the air masses and the occurrence frequencies of NPF events were similar during different periods, NPF events exhibited distinct characteristics during the normally hot (P1, relatively polluted) and heatwaves-dominated (P2, quite clean) periods. NPF_{polluted} within P1 period was favored by the decrease in background aerosol loading and the higher abundance of H₂SO₄. NPF_{clean, HW} events that occurred during the heatwave P2 period were characterizedobserved with lower CS, CoagS, FR and GR, as well as smaller R_{eff} and D_{mode}, than P1 NPF_{polluted} cases. According to the measured PNSDs, the P1 NPF_{polluted} events were mainly driven by local growth, while NPF_{clean, HW} events may be largely affected by transport under heatwaves. In comparison to the P1 NPF_{polluted} events, NPF_{clean, HW} occurred approximately one hour earlier and the subsequent growth was longer during P2, likely intensifying the photochemical oxidation due to heatwave-influenced aging processes and modulating the evolution of aerosol size distributions differently. Furthermore, significant differences in aerosol optical and hygroscopic properties were observed between the

normally hot and heatwave-dominated NPF days. The newly formed and grown particles mixed with pre-existing aerosols contributed a minor $\sigma_{sca, 525}$ noontime peak occurred on the much cleaner P2 NPF_{clean, HW} days, while the $\sigma_{sca, 525}$ peaked earlier around the morning rush hours on P1 NPF_{polluted} days. HBF and SAE were significantly higher on P2 NPF_{clean, HW} days, primarily due to the smaller R_{eff} for heatwave-influenced NPF_{clean, HW} cases. f(RH) remained relatively stable during the daytime of NPF days and peaked around 16:00-18:00 LT. Specifically, aerosol optical hygroscopicity tended to be higher during the subsequent growth and aging of both pre-existing particles and newly formed ones on P2 NPF_{clean, HW} days than that for P1 NPF_{polluted} days, which aligned with the higher f_W levels.

Compared with non-event cases, the generally higher levels of daily mean f(RH) suggested that the aerosol optical hygroscopicity was enhanced on NPF days in hot summer of urban Chongqing. A significantly positive (negative) correlation between f(RH) and SAE ($\sigma_{sca, 525}$, or rather the pollution level) was observed on NPF days for both periods, accompanied by higher f(RH) and SAE values on NPF_{clean, HW} days. This was likely due to the observed lower FR and GR caused by possible evaporation of both unstable clusters and particle coatings under heatwaves (Bousiotis et al., 2021; Cusack et al., 2013; Deng et al., 2020; Garmash et al., 2024), thereby reducing aerosol sizes (e.g., R_{eff}, D_{mode}) whereas increasing SAE. Moreover, heatwave-influenced stronger photooxidation enhanced the formation of more hygroscopic secondary components during the subsequent growth/aging processes of both pre-existing and newly formed particles on P2 NPF_{clean, HW} days in comparison to that of P1 NPF_{polluted} cases. The aerosol light scattering or volume concentration was mainly contributed by the larger accumulation-mode particles, while more ultrafine particles dominated the size distribution especially for the initial stage of heatwave-influenced NPF_{clean, HW} events, further leading to a lower f(RH) following the NPF occurrence (i.e., ~ 12:00 -15:00 LT) in comparison to P1 NPF_{polluted} days.

Changes in f(RH) could potentially impact the aerosol direct radiative forcing. A robust positive (negative) correlation existed between $f_{RF}(RH)$ and f(RH) (R_{eff}). Despite a lower $\sigma_{sca, 525}$ during heatwaves, the corresponding mean $f_{RF}(RH)$ was

relatively higher and the maximum value of 2.21 ± 0.23 was observed on P2 NPF_{clean, HW} days, associated with the highest f(RH) (1.71 \pm 0.13), smallest R_{eff} (102.8) \pm 12.4 nm), and highest HBF₅₂₅, RH/HBF₅₂₅ ratios (1.78 \pm 0.29). The above highlights that heatwaves could influence the NPF (e.g., the evolution in the aerosol size distribution pattern and chemical composition) and atmospheric processing (although with a decreased aerosol Reff and Dmode likely due to evaporation-resulted non-spherical particle morphology under persistently high temperature conditions), thereby enhancing aerosol optical hygroscopic growth and potentially reducing the net solar radiation directly especially in hot summer. This study revealed divergent changes in aerosol optical and hygroscopic properties on different NPF days, thereby modulating the aerosol radiative forcing distinctly during a heatwave in summer 2022. A comprehensive understanding of the formation mechanisms of different NPF events (e.g., local formation versus the horizontal or vertical transport) in diverse environment is crucial in the future. The last but not the least, further explorations on detailed molecular-scale characterizations molecular (e.g., structures and compositions of newly and secondary formed particles, as well as particle morphology) and aerosol radiative impacts including the aerosol-cloud interactions of both heatwaves and other weather extremes (e.g., heatwaves) with the changing climate are highly recommended.

747

748

728

729

730

731

732

733

734

735

736

737

738

739

740

741

742

743

744

745

746

Data availability. Data will be available upon request.

749

750

751

752

753

754

755

Author contributions. YH and PL: Methodology, Investigation, Data analysis, Formal analysis, Visualization, Validation, Writing – original draft & editing. YG and ZW: Methodology, Investigation, Formal analysis. MT, YC, HX and WH: Data curation, Methodology. FW and YL: Investigation. YK: Methodology, Data analysis, Writing – review & editing. JC: Conceptualization, Methodology, Funding acquisition, Data curation, Writing – review & editing, Supervision.

756

757 **Competing interests.** The authors declare no competing financial interest.

758

- 759 **Acknowledgement.** This work was supported by the National Natural Science
- Foundation of China (No. 42105075), Venture and Innovation Support Program
- for Chongqing Overseas Returnees (No. cx2021021). We thank Biao Xue for the
- 762 technical support on the utilization and maintenance of the humidified
- nephelometer system. We also thank Ziqian Wang for the TSP filter sample
- collection and Jiawei Zhou for the corresponding offline chemical analysis.

765

766

References

- 767 An, J., Lu, Y., Huang, D. D., Ding, X., Hu, Q., Yan, R., Qiao, L., Zhou, M., Huang, C.,
- Wang, H., Fu, Q., Yu, F., and Wang, L.: Sectoral Size Resolved Particle Number
- 769 Emissions With Speciation: Emission Profile Based Quantification and a Case Study
- in the Yangtze River Delta Region, China, J. Geophys. Res. Atmos., 1–22,
- 771 https://doi.org/10.1029/2024JD041234, 2024.
- Andrews, E., Sheridan, P. J., Fiebig, M., McComiskey, A., Ogren, J. A., Arnott, P.,
- Covert, D., Elleman, R., Gasparini, R., Collins, D., Jonsson, H., Schmid, B., and
- Wang, J.: Comparison of methods for deriving aerosol asymmetry parameter, J.
- 775 Geophys. Res. Atmos., 111, 1–16, https://doi.org/10.1029/2004JD005734, 2006.
- 776 Asmi, E., Frey, A., Virkkula, A., Ehn, M., Manninen, H. E., Timonen, H.,
- 777 Tolonen-Kivimäki, O., Aurela, M., Hillamo, R., and Kulmala, M.: Hygroscopicity and
- chemical composition of antarctic sub-micrometre aerosol particles and observations
- of new particle formation, Atmos. Chem. Phys., 10, 4253–4271,
- 780 https://doi.org/10.5194/acp-10-4253-2010, 2010.
- 781 Bae, M. S., Lee, T., Schauer, J. J., Park, G., Son, Y. B., Kim, K. H., Cho, S. S., Park,
- 782 S. S., Park, K., and Shon, Z. H.: Chemical Characteristics of Size-Resolved Aerosols

- 783 in Coastal Areas during KORUS-AQ Campaign; Comparison of Ion Neutralization
- 784 Model, Asia-Pacific J. Atmos. Sci., 55, 387–399,
- 785 https://doi.org/10.1007/s13143-018-00099-1, 2019.
- Bousiotis, D., Brean, J., Pope, F. D., Dall'Osto, M., Querol, X., Alastuey, A., Perez,
- 787 N., Petäjä, T., Massling, A., Klenø Nøjgaard, J., Nordstrøm, C., Kouvarakis, G.,
- Vratolis, S., Eleftheriadis, K., Niemi, J. V., Portin, H., Wiedensohler, A., Weinhold,
- 789 K., Merkel, M., Tuch, T., and Harrison, R. M.: The effect of meteorological
- 790 conditions and atmospheric composition in the occurrence and development of new
- particle formation (NPF) events in Europe, Atmos. Chem. Phys., 21, 3345-3370,
- 792 https://doi.org/10.5194/acp-21-3345-2021, 2021.
- 793 Brooke Anderson, G. and Bell, M. L.: Heat waves in the United States: Mortality risk
- during heat waves and effect modification by heat wave characteristics in 43 U.S.
- 795 communities, Environ. Health Perspect., 119, 210–218,
- 796 https://doi.org/10.1289/ehp.1002313, 2011.
- 797 Cai, R., Chandra, I., Yang, D., Yao, L., Fu, Y., Li, X., Lu, Y., Luo, L., Hao, J., Ma, Y.,
- Wang, L., Zheng, J., Seto, T., and Jiang, J.: Estimating the influence of transport on
- aerosol size distributions during new particle formation events, Atmos. Chem. Phys.,
- 800 18, 16587–16599, https://doi.org/10.5194/acp-18-16587-2018, 2018.
- 801 Chen, J., Zhao, C. S., Ma, N., and Yan, P.: Aerosol hygroscopicity parameter derived
- from the light scattering enhancement factor measurements in the North China Plain,
- 803 Atmos. Chem. Phys., 14, 8105–8118, https://doi.org/10.5194/acp-14-8105-2014,
- 804 2014.
- 805 Chen, Q., Mu, Z., Song, W., Wang, Y., Yang, Z., Zhang, L., and Zhang, Y. L.:
- 806 Size-Resolved Characterization of the Chromophores in Atmospheric Particulate
- Matter From a Typical Coal-Burning City in China, J. Geophys. Res. Atmos., 124,
- 808 10546–10563, https://doi.org/10.1029/2019JD031149, 2019.

- 809 Chen, T., Wang, T., Xue, L., and Brasseur, G.: Heatwave exacerbates air pollution in
- 810 China through intertwined climate-energy-environment interactions, Sci. Bull., 69,
- 811 2765–2775, https://doi.org/10.1016/j.scib.2024.05.018, 2024.
- 812 China Meteorological Administration, 2022. China Climate Bulletin 2022.
- 813 https://www.cma.gov.cn/zfxxgk/gknr/qxbg/202303/t20230324 5396394.html.
- Accessed on 23 March 2023. (in Chinese).
- 815 Cho Cheung, H., Chung-Kuang Chou, C., Siu Lan Lee, C., Kuo, W. C., and Chang, S.
- 816 C.: Hygroscopic properties and cloud condensation nuclei activity of atmospheric
- aerosols under the influences of Asian continental outflow and new particle formation
- at a coastal site in eastern Asia, Atmos. Chem. Phys., 20, 5911-5922,
- 819 https://doi.org/10.5194/acp-20-5911-2020, 2020.
- 820 Chylek, P. and Wong, J.: Effect of absorbing aerosols on global radiation budget,
- 821 Geophys. Res. Lett., 22, 929–931, https://doi.org/10.1029/95GL00800, 1995.
- 822 Collaud Coen, M., Weingartner, E., Nyeki, S., Cozic, J., Henning, S., Verheggen, B.,
- 623 Gehrig, R., and Baltensperger, U.: Long-term trend analysis of aerosol variables at the
- 824 high-alpine site Jungfraujoch, J. Geophys. Res. Atmos., 112,
- 825 https://doi.org/10.1029/2006JD007995, 2007.
- 826 Covert, D. S., Charlson, R. J., and Ahlquist, N. C.: A Study of the Relationship of
- 827 Chemical Composition and Humidity to Light Scattering by Aerosols, J. Appl.
- 828 Meteorol., 11, 968–976,
- 829 https://doi.org/10.1175/1520-0450(1972)011<0968:asotro>2.0.co;2, 1972.
- 830 Crumeyrolle, S., Kontkanen, J. S. S., Rose, C., Velazquez Garcia, A., Bourrianne, E.,
- Catalfamo, M., Riffault, V., Tison, E., Ferreira De Brito, J., Visez, N., Ferlay, N.,
- 832 Auriol, F., and Chiapello, I.: Measurement report: Atmospheric new particle
- formation at a peri-urban site in Lille, northern France, Atmos. Chem. Phys., 23,
- 834 183–201, https://doi.org/10.5194/acp-23-183-2023, 2023.

- 835 Cusack, M., Alastuey, A., and Querol, X.: Case studies of new particle formation and
- evaporation processes in the western Mediterranean regional background, Atmos.
- 837 Environ., 81, 651–659, https://doi.org/10.1016/j.atmosenv.2013.09.025, 2013.
- Dada, L., Paasonen, P., Nieminen, T., Buenrostro Mazon, S., Kontkanen, J., Peräkylä,
- O., Lehtipalo, K., Hussein, T., Petäjä, T., Kerminen, V. M., Bäck, J., and Kulmala, M.:
- 840 Long-term analysis of clear-sky new particle formation events and nonevents in
- 841 Hyytiälä, Atmos. Chem. Phys., 17, 6227–6241,
- 842 https://doi.org/10.5194/acp-17-6227-2017, 2017.
- Dal Maso, M., Kulmala, M., Riipinen, I., Wagner, R., Hussein, T., Aalto, P. P., and
- Lehtinen, K. E. J.: Formation and growth of fresh atmospheric aerosols: Eight years
- of aerosol size distribution data from SMEAR II, Hyytiälä, Finland, Boreal Environ.
- 846 Res., 10, 323–336, 2005.
- Delene, D. J. and Ogren, J. A.: Variability of aerosol optical properties at four North
- 848 American surface monitoring sites, J. Atmos. Sci., 59, 1135–1150,
- 849 https://doi.org/10.1175/1520-0469(2002)059<1135:VOAOPA>2.0.CO;2, 2002.
- Deng, C., Cai, R., Yan, C., Zheng, J., and Jiang, J.: Formation and growth of sub-3
- nm particles in megacities: Impact of background aerosols, Faraday Discuss., 226,
- 852 348–363, https://doi.org/10.1039/d0fd00083c, 2021.
- 853 Deng, C., Fu, Y., Dada, L., Yan, C., Cai, R., Yang, D., Zhou, Y., Yin, R., Lu, Y., Li,
- 854 X., Qiao, X., Fan, X., Nie, W., Kontkanen, J., Kangasluoma, J., Chu, B., Ding, A.,
- Kerminen, V. M., Paasonen, P., Worsnop, D. R., Bianchi, F., Liu, Y., Zheng, J., Wang,
- 856 L., Kulmala, M., and Jiang, J.: Seasonal characteristics of new particle formation and
- 857 growth in urban Beijing, Environ. Sci. Technol., 54, 8547-8557,
- 858 https://doi.org/10.1021/acs.est.0c00808, 2020.
- 859 Duan, J., Huang, R. J., Wang, Y., Xu, W., Zhong, H., Lin, C., Huang, W., Gu, Y.,
- 860 Ovadnevaite, J., Ceburnis, D., and O'Dowd, C.: Measurement report: Size-resolved

- secondary organic aerosol formation modulated by aerosol water uptake in wintertime
- haze, Atmos. Chem. Phys., 24, 7687–7698, https://doi.org/10.5194/acp-24-7687-2024,
- 863 2024.
- Fan, J., Wang, Y., Rosenfeld, D., and Liu, X.: Review of aerosol-cloud interactions:
- Mechanisms, significance, and challenges, J. Atmos. Sci., 73, 4221–4252,
- 866 https://doi.org/10.1175/JAS-D-16-0037.1, 2016.
- Fierz-Schmidhauser, R., Zieger, P., Gysel, M., Kammermann, L., Decarlo, P. F.,
- 868 Baltensperger, U., and Weingartner, E.: Measured and predicted aerosol light
- scattering enhancement factors at the high alpine site Jungfraujoch, Atmos. Chem.
- 870 Phys, 10, 2319–2333, 2010.
- 671 Garmash, O., Ezhova, E., Arshinov, M., Belan, B., Lampilahti, A., Davydov, D., Räty,
- M., Aliaga, D., Baalbaki, R., Chan, T., Bianchi, F., Kerminen, V. M., Petäjä, T., and
- Kulmala, M.: Heatwave reveals potential for enhanced aerosol formation in Siberian
- 874 boreal forest, Environ. Res. Lett., 19, https://doi.org/10.1088/1748-9326/ad10d5,
- 875 2024.
- 876 Giordano, M., Espinoza, C., and Asa-Awuku, A.: Experimentally measured
- morphology of biomass burning aerosol and its impacts on CCN ability, Atmos.
- 878 Chem. Phys., 15, 1807–1821, https://doi.org/10.5194/acp-15-1807-2015, 2015.
- 879 Gu, Y., Huang, R. J., Duan, J., Xu, W., Lin, C., Zhong, H., Wang, Y., Ni, H., Liu, Q.,
- 880 Xu, R., Wang, L., and Li, Y. J.: Multiple pathways for the formation of secondary
- organic aerosol in the North China Plain in summer, Atmos. Chem. Phys., 23,
- 882 5419–5433, https://doi.org/10.5194/acp-23-5419-2023, 2023.
- Guenther, A. B., Monson, R. K., and Fall, R.: Isoprene and monoterpene emission
- 884 rate variability: Observations with eucalyptus and emission rate algorithm
- development, J. Geophys. Res. Atmos., 96, 10799–10808,
- 886 https://doi.org/10.1029/91jd00960, 1991.

- 887 Guo, X., Huang, J., Luo, Y., Zhao, Z., and Xu, Y.: Projection of heat waves over
- China for eight different global warming targets using 12 CMIP5 models, Theor. Appl.
- 889 Climatol., 128, 507–522, https://doi.org/10.1007/s00704-015-1718-1, 2016.
- Hamed, A., Joutsensaari, J., Mikkonen, S., Sogacheva, L., Dal Maso, M., Kulmala,
- 891 M., Cavalli, F., Fuzzi, S., Facchini, M. C., Decesari, S., Mircea, M., Lehtinen, K. E. J.,
- and Laaksonen, A.: Nucleation and growth of new particles in Po Valley, Italy, Atmos.
- 893 Chem. Phys., 7, 355–376, https://doi.org/10.5194/acp-7-355-2007, 2007.
- Hamed, A., Korhonen, H., Sihto, S. L., Joutsensaari, J., Jrvinen, H., Petäjä, T., Arnold,
- F., Nieminen, T., Kulmala, M., Smith, J. N., Lehtinen, K. E. J., and Laaksonen, A.:
- The role of relative humidity in continental new particle formation, J. Geophys. Res.
- 897 Atmos., 116, 1–12, https://doi.org/10.1029/2010JD014186, 2011.
- 898 Hand, J. L. and Malm, W. C.: Review of aerosol mass scattering efficiencies from
- ground-based measurements since 1990, J. Geophys. Res. Atmos., 112,
- 900 https://doi.org/10.1029/2007JD008484, 2007.
- Hao, Y., Gou, Y., Wang, Z., Huang, W., Wan, F., Tian, M., and Chen, J.: Current
- 902 challenges in the visibility improvement of urban Chongqing in Southwest China:
- From the perspective of PM2.5-bound water uptake property over 2015–2021, Atmos.
- 904 Res., 300, 107215, https://doi.org/10.1016/j.atmosres.2023.107215, 2024.
- 905 Hao, Z., Chen, Y., Feng, S., Liao, Z., An, N., and Li, P.: The 2022
- 906 Sichuan-Chongqing spatio-temporally compound extremes: a bitter taste of novel
- 907 hazards, Sci. Bull., 68, 1337–1339, https://doi.org/10.1016/j.scib.2023.05.034, 2023.
- 908 Hauser, M., Orth, R., and Seneviratne, S. I.: Role of soil moisture versus recent
- climate change for the 2010 heat wave in western Russia, Geophys. Res. Lett., 43,
- 910 2819–2826, https://doi.org/10.1002/2016GL068036, 2016.
- 911 Jefferson, A., Hageman, D., Morrow, H., Mei, F., and Watson, T.: Seven years of
- aerosol scattering hygroscopic growth measurements from SGP: Factors influencing

- 913 water uptake, J. Geophys. Res. Atmos., 122, 9451–9466,
- 914 https://doi.org/10.1002/2017JD026804, 2017.
- 915 Jin, X., Li, Z., Wu, T., Wang, Y., Cheng, Y., Su, T., Wei, J., Ren, R., Wu, H., Li, S.,
- 216 Zhang, D., and Cribb, M.: The different sensitivities of aerosol optical properties to
- particle concentration, humidity, and hygroscopicity between the surface level and the
- 918 upper boundary layer in Guangzhou, China, Sci. Total Environ., 803, 150010,
- 919 https://doi.org/10.1016/j.scitotenv.2021.150010, 2022.
- 920 Kerminen, V. M., Chen, X., Vakkari, V., Petäjä, T., Kulmala, M., and Bianchi, F.:
- 921 Atmospheric new particle formation and growth: Review of field observations,
- 922 Environ. Res. Lett., 13, https://doi.org/10.1088/1748-9326/aadf3c, 2018.
- Kim, N., Yum, S. S., Park, M., Park, J. S., Shin, H. J., and Ahn, J. Y.: Hygroscopicity
- of urban aerosols and its link to size-resolved chemical composition during spring and
- 925 summer in Seoul, Korea, Atmos. Chem. Phys., 20, 11245-11262,
- 926 https://doi.org/10.5194/acp-20-11245-2020, 2020.
- 927 Kotchenruther, R. A., Hobbs, P. V., and Hegg, D. A.: Humidification factors for
- atmospheric aerosols off the mid-Atlantic coast of the United States, J. Geophys. Res.
- 929 Atmos., 104, 2239–2251, https://doi.org/10.1029/98JD01751, 1999.
- 930 Kuang, Y., He, Y., Xu, W., Zhao, P., Cheng, Y., Zhao, G., Tao, J., Ma, N., Su, H.,
- Zhang, Y., Sun, J., Cheng, P., Yang, W., Zhang, S., Wu, C., Sun, Y., and Zhao, C.:
- 932 Distinct diurnal variation in organic aerosol hygroscopicity and its relationship with
- 933 oxygenated organic aerosol, Atmos. Chem. Phys., 20, 865–880,
- 934 https://doi.org/10.5194/acp-20-865-2020, 2020.
- 935 Kuang, Y., Zhao, C. S., Zhao, G., Tao, J. C., Xu, W., Ma, N., and Bian, Y. X.: A
- 936 novel method for calculating ambient aerosol liquid water content based on
- 937 measurements of a humidified nephelometer system, Atmos. Meas. Tech., 11,
- 938 2967–2982, https://doi.org/10.5194/amt-11-2967-2018, 2018.

- 839 Kuang, Y., Zhao, C., Tao, J., Bian, Y., Ma, N., and Zhao, G.: A novel method for
- 940 deriving the aerosol hygroscopicity parameter based only on measurements from a
- 941 humidified nephelometer system, Atmos. Chem. Phys., 17, 6651–6662,
- 942 https://doi.org/10.5194/acp-17-6651-2017, 2017.
- Kulmala, M., Dada, L., Daellenbach, K. R., Yan, C., Stolzenburg, D., Kontkanen, J.,
- Ezhova, E., Hakala, S., Tuovinen, S., Kokkonen, T. V., Kurppa, M., Cai, R., Zhou, Y.,
- Yin, R., Baalbaki, R., Chan, T., Chu, B., Deng, C., Fu, Y., Ge, M., He, H., Heikkinen,
- L., Junninen, H., Liu, Y., Lu, Y., Nie, W., Rusanen, A., Vakkari, V., Wang, Y., Yang, G.,
- 947 Yao, L., Zheng, J., Kujansuu, J., Kangasluoma, J., Petaja, T., Paasonen, P., Jarvi, L.,
- Worsnop, D., Ding, A., Liu, Y., Wang, L., Jiang, J., Bianchi, F., and Kerminen, V. M.:
- 949 Is reducing new particle formation a plausible solution to mitigate particulate air
- pollution in Beijing and other Chinese megacities?, Faraday Discuss., 226, 334–347,
- 951 https://doi.org/10.1039/d0fd00078g, 2021.
- Kulmala, M., Petäjä, T., Nieminen, T., Sipilä, M., Manninen, H. E., Lehtipalo, K., Dal
- 953 Maso, M., Aalto, P. P., Junninen, H., Paasonen, P., Riipinen, I., Lehtinen, K. E. J.,
- Laaksonen, A., and Kerminen, V. M.: Measurement of the nucleation of atmospheric
- 955 aerosol particles, Nat. Protoc., 7, 1651–1667, https://doi.org/10.1038/nprot.2012.091,
- 956 2012.
- 957 Kulmala, M.: How Particles Nucleate and Grow, Science, 302, 1000-1001,
- 958 https://doi.org/10.1126/science.1090848, 2003.
- 859 Kurtén, T., Torpo, L., Ding, C. G., Vehkamäki, H., Sundberg, M. R., Laasonen, K.,
- and Kulmala, M.: A density functional study on water-sulfuric acid-ammonia clusters
- and implications for atmospheric cluster formation, J. Geophys. Res. Atmos., 112, 1–7,
- 962 https://doi.org/10.1029/2006JD007391, 2007.
- 963 Lai, S., Hai, S., Gao, Y., Wang, Y., Sheng, L., Lupascu, A., Ding, A., Nie, W., Qi, X.,
- Huang, X., Chi, X., Zhao, C., Zhao, B., Shrivastava, M., Fast, J. D., Yao, X., and Gao,
- 965 H.: The striking effect of vertical mixing in the planetary boundary layer on new

- particle formation in the Yangtze River Delta, Sci. Total Environ., 829, 154607,
- 967 https://doi.org/10.1016/j.scitotenv.2022.154607, 2022.
- Lee, K., Chandra, I., Seto, T., Inomata, Y., Hayashi, M., Takami, A., Yoshino, A., and
- Otani, Y.: Aerial observation of atmospheric nanoparticles on Fukue Island, Japan,
- 970 Aerosol Air Qual. Res., 19, 981–994, https://doi.org/10.4209/aagr.2018.03.0077,
- 971 2019.
- 272 Li, Y., Ding, Y., and Li, W.: Observed trends in various aspects of compound heat
- 973 waves across China from 1961 to 2015, J. Meteorol. Res., 31, 455-467,
- 974 https://doi.org/10.1007/s13351-017-6150-2, 2017.
- Li, Z., Tikkanen, O. P., Buchholz, A., Hao, L., Kari, E., Yli-Juuti, T., and Virtanen, A.:
- 976 Effect of Decreased Temperature on the Evaporation of α-Pinene Secondary Organic
- 977 Aerosol Particles, ACS Earth Sp. Chem., 3, 2775–2785,
- https://doi.org/10.1021/acsearthspacechem.9b00240, 2019.
- Liu, H. J., Zhao, C. S., Nekat, B., Ma, N., Wiedensohler, A., Van Pinxteren, D.,
- 980 Spindler, G., Müller, K., and Herrmann, H.: Aerosol hygroscopicity derived from
- 981 size-segregated chemical composition and its parameterization in the North China
- 982 Plain, Atmos. Chem. Phys., 14, 2525–2539, https://doi.org/10.5194/acp-14-2525-2014,
- 983 2014.
- Liu, P. F., Zhao, C. S., Göbel, T., Hallbauer, E., Nowak, A., Ran, L., Xu, W. Y., Deng,
- 28. Z., Ma, N., Mildenberger, K., Henning, S., Stratmann, F., and Wiedensohler, A.:
- 986 Hygroscopic properties of aerosol particles at high relative humidity and their diurnal
- variations in the north China plain, Atmos. Chem. Phys., 11, 3479–3494,
- 988 https://doi.org/10.5194/acp-11-3479-2011, 2011.
- 989 Lu, Y., Yan, C., Fu, Y., Chen, Y., Liu, Y., Yang, G., Wang, Y., Bianchi, F., Chu, B.,
- Zhou, Y., Yin, R., Baalbaki, R., Garmash, O., Deng, C., Wang, W., Liu, Y., Petäjä, T.,
- 991 Kerminen, V. M., Jiang, J., Kulmala, M., and Wang, L.: A proxy for atmospheric

- daytime gaseous sulfuric acid concentration in urban Beijing, Atmos. Chem. Phys., 19,
- 993 1971–1983, https://doi.org/10.5194/acp-19-1971-2019, 2019.
- Luoma, K., Virkkula, A., Aalto, P., Petäjä, T., and Kulmala, M.: Over a 10-year record
- of aerosol optical properties at SMEAR II, Atmos. Chem. Phys., 19, 11363–11382,
- 996 https://doi.org/10.5194/acp-19-11363-2019, 2019.
- 997 Ma, C. Sen, Ma, G., and Pincebourde, S.: Survive a Warming Climate: Insect
- 998 Responses to Extreme High Temperatures, Annu. Rev. Entomol., 66, 163–184,
- 999 https://doi.org/10.1146/annurev-ento-041520-074454, 2021.
- 1000 Ma, N., Zhao, C., Tao, J., Wu, Z., Kecorius, S., Wang, Z., Groß, J., Liu, H., Bian, Y.,
- Kuang, Y., Teich, M., Spindler, G., Muller, K., Van Pinxteren, D., Herrmann, H., Hu,
- 1002 M., and Wiedensohler, A.: Variation of CCN activity during new particle formation
- events in the North China Plain, Atmos. Chem. Phys., 16, 8593-8607,
- 1004 https://doi.org/10.5194/acp-16-8593-2016, 2016.
- 1005 Marshall, S. F., Covert, D. S., and Charlson, R. J.: Relationship between asymmetry
- 1006 parameter and hemispheric backscatter ratio: implications for climate forcing by
- 1007 aerosols, Appl. Opt., 34, 5–6, 1995.
- 1008 Merikanto, J., Spracklen, D. V, Mann, G. W., Pickering, S. J., and Carslaw, K. S.:
- 1009 Atmospheric Chemistry and Physics Impact of nucleation on global CCN, Atmos.
- 1010 Chem. Phys, 9, 8601–8616, 2009.
- 1011 Mishchenko, M. I.: Electromagnetic scattering by nonspherical particles: A tutorial
- 1012 review, J. Quant. Spectrosc. Radiat. Transf., 110, 808-832,
- 1013 https://doi.org/10.1016/j.jqsrt.2008.12.005, 2009.
- 1014 Moise, T., Flores, J. M., and Rudich, Y.: Optical Properties of Secondary Organic
- 1015 Aerosols and Their Changes by Chemical Processes, Chem. Rev., 115, 4400–4439,
- 1016 https://doi.org/10.1021/cr5005259, 2015.

- Nairn, J. R. and Fawcett, R. J. B.: The excess heat factor: A metric for heatwave
- intensity and its use in classifying heatwave severity, Int. J. Environ. Res. Public
- Health, 12, 227–253, https://doi.org/10.3390/ijerph120100227, 2014.
- 1020 Platis, A., Altstädter, B., Wehner, B., Wildmann, N., Lampert, A., Hermann, M.,
- 1021 Birmili, W., and Bange, J.: An Observational Case Study on the Influence of
- 1022 <u>Atmospheric Boundary-Layer Dynamics on New Particle Formation, Boundary-Layer</u>
- 1023 Meteorol., 158, 67–92, https://doi.org/10.1007/s10546-015-0084-y, 2016.
- 1024 Petters, M. D. and Kreidenweis, S. M.: A single parameter representation of
- hygroscopic growth and cloud condensation nucleus activity, Atmos. Chem. Phys., 7,
- 1026 1961–1971, https://doi.org/10.5194/acp-7-1961-2007, 2007.
- 1027 Pierce, T. E. and Waldruff, P. S.: Pc-beis: A personal computer version of the biogenic
- emissions inventory system, J. Air Waste Manag. Assoc., 41, 937-941,
- 1029 https://doi.org/10.1080/10473289.1991.10466890, 1991.
- 1030 Qi, X. M., Ding, A. J., Nie, W., Petäjä, T., Kerminen, V. M., Herrmann, E., Xie, Y. N.,
- Zheng, L. F., Manninen, H., Aalto, P., Sun, J. N., Xu, Z. N., Chi, X. G., Huang, X.,
- Boy, M., Virkkula, A., Yang, X. Q., Fu, C. B., and Kulmala, M.: Aerosol size
- distribution and new particle formation in the western Yangtze River Delta of China:
- 1034 2 years of measurements at the SORPES station, Atmos. Chem. Phys., 15,
- 1035 12445–12464, https://doi.org/10.5194/acp-15-12445-2015, 2015.
- 1036 Quinn, P. K., Bates, T. S., Baynard, T., Clarke, A. D., Onasch, T. B., Wang, W., Rood,
- 1037 M. J., Andrews, E., Allan, J., Carrico, C. M., Coffman, D., and Worsnop, D.: Impact
- of particulate organic matter on the relative humidity dependence of light scattering: A
- 1039 simplified parameterization, Geophys. Res. Lett., 32, 1-4,
- 1040 https://doi.org/10.1029/2005GL024322, 2005.
- 1041 Ren, J., Chen, L., Fan, T., Liu, J., Jiang, S., and Zhang, F.: The NPF Effect on CCN
- Number Concentrations: A Review and Re-Evaluation of Observations From 35 Sites

- 1043 Worldwide, Geophys. Res. Lett., 48, 1–12, https://doi.org/10.1029/2021GL095190,
- 1044 2021.
- Rosati, B., Isokääntä, S., Christiansen, S., Jensen, M. M., Moosakutty, S. P., De Jonge,
- 1046 R. W., Massling, A., Glasius, M., Elm, J., Virtanen, A., and Bilde, M.:
- Hygroscopicity and CCN potential of DMS-derived aerosol particles, Atmos. Chem.
- 1048 Phys., 22, 13449–13466, https://doi.org/10.5194/acp-22-13449-2022, 2022.
- Salma, I., Thén, W., Aalto, P., Kerminen, V. M., Kern, A., Barcza, Z., Petäjä, T., and
- 1050 Kulmala, M.: Influence of vegetation on occurrence and time distributions of regional
- new aerosol particle formation and growth, Atmos. Chem. Phys., 21, 2861–2880,
- 1052 https://doi.org/10.5194/acp-21-2861-2021, 2021.
- 1053 Schuster, G. L., Dubovik, O., and Holben, B. N.: Angstrom exponent and bimodal
- 1054 aerosol size distributions, J. Geophys. Res. Atmos., 111, 1-14,
- 1055 https://doi.org/10.1029/2005JD006328, 2006.
- 1056 Shang, D., Hu, M., Tang, L., Fang, X., Liu, Y., Wu, Y., Du, Z., Cai, X., Wu, Z., Lou,
- 1057 S., Hallquist, M., Guo, S., and Zhang, Y.: Significant effects of transport on
- nanoparticles during new particle formation events in the atmosphere of Beijing,
- Particuology, 80, 1–10, https://doi.org/10.1016/j.partic.2022.12.006, 2023.
- Sharma, S. and Mujumdar, P.: Increasing frequency and spatial extent of concurrent
- 1061 meteorological droughts and heatwaves in India, Sci. Rep., 7, 1–9,
- 1062 https://doi.org/10.1038/s41598-017-15896-3, 2017.
- 1063 Shen, X. J., Sun, J. Y., Zhang, Y. M., Wehner, B., Nowak, A., Tuch, T., Zhang, X. C.,
- Wang, T. T., Zhou, H. G., Zhang, X. L., Dong, F., Birmili, W., and Wiedensohler, A.:
- First long-term study of particle number size distributions and new particle formation
- events of regional aerosol in the North China Plain, Atmos. Chem. Phys., 11,
- 1067 1565–1580, https://doi.org/10.5194/acp-11-1565-2011, 2011.

- Su, Y. W.: The effects of extreme high temperature day off on electricity conservation,
- 1069 Weather. Clim. Soc., 13, 769–782, https://doi.org/10.1175/WCAS-D-20-0176.1, 2021.
- Sun, J., Hermann, M., Weinhold, K., Merkel, M., Birmili, W., Yang, Y., Flentje, H.,
- Ries, L., Couret, C., Elsasser, M., Sohmer, R., Wirtz, K., Meinhardt, F., Schü, M.,
- Bath, O., Hellack, B., Kerminen, V., Kulmala, M., Ma, N., and Wiedensohler, A.:
- 1073 Measurement report : Contribution of atmospheric new particle formation to ultrafine
- particle concentration, cloud condensation nuclei and radiative forcing: Results from
- 1075 five-year observations in Central Europe, Atmos. Chem. Phys., 1–34,
- 1076 https://doi.org/10.5194/acp-24-10667-2024, 2024.
- 1077 Sun, X., Sun, Q., Zhou, X., Li, X., Yang, M., Yu, A., and Geng, F.: Heat wave impact
- on mortality in Pudong New Area, China in 2013, Sci. Total Environ., 493, 789–794,
- 1079 https://doi.org/10.1016/j.scitotenv.2014.06.042, 2014.
- Sun, Y., Song, L., Yin, H., Zhang, X., Stott, P., Zhou, B., and Hu, T.: 20. Human
- influence on the 2015 extreme high temperature events in Western China, Bull. Am.
- 1082 Meteorol. Soc., 97, S102–S106, https://doi.org/10.1175/BAMS-D-16-0158.1, 2016.
- Tan, J., Zheng, Y., Song, G., Kalkstein, L. S., Kalkstein, A. J., and Tang, X.: Heat
- wave impacts on mortality in Shanghai, 1998 and 2003, Int. J. Biometeorol., 51,
- 1085 193–200, https://doi.org/10.1007/s00484-006-0058-3, 2007.
- Tan, W., Yu, Y., Li, C., Li, J., Kang, L., Dong, H., Zeng, L., and Zhu, T.: Profiling
- Aerosol Liquid Water Content Using a Polarization Lidar, Environ. Sci. Technol., 54,
- 1088 3129–3137, https://doi.org/10.1021/acs.est.9b07502, 2020.
- 1089 Tang, M., Chan, C. K., Li, Y. J., Su, H., Ma, Q., Wu, Z., Zhang, G., Wang, Z., Ge, M.,
- Hu, M., He, H., and Wang, X.: A review of experimental techniques for aerosol
- 1091 hygroscopicity studies, Atmos. Chem. Phys., 19, 12631–12686,
- 1092 https://doi.org/10.5194/acp-19-12631-2019, 2019.

- 1093 Tao, L., Zhou, Z., Tao, J., Zhang, L., Wu, C., Li, J., Yue, D., Wu, Z., Zhang, Z., Yuan,
- 1094 Z., Huang, J., and Wang, B.: High contribution of new particle formation to ultrafine
- particles in four seasons in an urban atmosphere in south China, Sci. Total Environ.,
- 1096 889, https://doi.org/10.1016/j.scitotenv.2023.164202, 2023.
- Teng, M., Liao, H., Burke, P. J., Chen, T., and Zhang, C.: Adaptive responses: the
- effects of temperature levels on residential electricity use in China, Clim. Change, 172,
- 1099 https://doi.org/10.1007/s10584-022-03374-3, 2022.
- 1100 Tian, J., Wang, Q., Zhang, Y., Yan, M., Liu, H., Zhang, N., Ran, W., and Cao, J.:
- 1101 Impacts of primary emissions and secondary aerosol formation on air pollution in an
- urban area of China during the COVID-19 lockdown, Environ. Int., 150, 106426,
- 1103 https://doi.org/10.1016/j.envint.2021.106426, 2021.
- 1104 Titos, G., Burgos, M. A., Zieger, P., Alados-Arboledas, L., Baltensperger, U.,
- Jefferson, A., Sherman, J., Weingartner, E., Henzing, B., Luoma, K., O'Dowd, C.,
- Wiedensohler, A., and Andrews, E.: A global study of hygroscopicity-driven
- light-scattering enhancement in the context of other in situ aerosol optical properties,
- 1108 Atmos. Chem. Phys., 21, 13031–13050, https://doi.org/10.5194/acp-21-13031-2021,
- 1109 2021.
- 1110 Titos, G., Cazorla, A., Zieger, P., Andrews, E., Lyamani, H., Granados-Muñoz, M. J.,
- Olmo, F. J., and Alados-Arboledas, L.: Effect of hygroscopic growth on the aerosol
- light-scattering coefficient: A review of measurements, techniques and error sources,
- 1113 Atmos. Environ., 141, 494–507, https://doi.org/10.1016/j.atmosenv.2016.07.021,
- 1114 2016.
- 1115 Titos, G., Jefferson, A., Sheridan, P. J., Andrews, E., Lyamani, H., Alados-Arboledas,
- 1116 L., and Ogren, J. A.: Aerosol light-scattering enhancement due to water uptake during
- 1117 the TCAP campaign, Atmos. Chem. Phys., 14, 7031–7043,
- 1118 https://doi.org/10.5194/acp-14-7031-2014, 2014.

- 1119 Tritscher, T., Jurnyi, Z., Martin, M., Chirico, R., Gysel, M., Heringa, M. F., Decarlo,
- 1120 P. F., Sierau, B., Prévt, A. S. H., Weingartner, E., and Baltensperger, U.: Changes of
- hygroscopicity and morphology during ageing of diesel soot, Environ. Res. Lett., 6,
- https://doi.org/10.1088/1748-9326/6/3/034026, 2011.
- 1123 Wang, N., Du, Y., Chen, D., Meng, H., Chen, X., Zhou, L., Shi, G., Zhan, Y., Feng,
- 1124 M., Li, W., Chen, M., Li, Z., and Yang, F.: Spatial disparities of ozone pollution in
- the Sichuan Basin spurred by extreme, hot weather, Atmos. Chem. Phys., 24,
- 3029–3042, https://doi.org/10.5194/acp-24-3029-2024, 2024.
- 1127 Wang, Y., Li, Z., Zhang, R., Jin, X., Xu, W., Fan, X., Wu, H., Zhang, F., Sun, Y., Wang,
- 1128 Q., Cribb, M., and Hu, D.: Distinct Ultrafine- and Accumulation-Mode Particle
- Properties in Clean and Polluted Urban Environments, Geophys. Res. Lett., 46,
- 1130 10918–10925, https://doi.org/10.1029/2019GL084047, 2019.
- 1131 Wang, Z. B., Hu, M., Sun, J. Y., Wu, Z. J., Yue, D. L., Shen, X. J., Zhang, Y. M., Pei,
- 1132 X. Y., Cheng, Y. F., and Wiedensohler, A.: Characteristics of regional new particle
- formation in urban and regional background environments in the North China Plain,
- 1134 Atmos. Chem. Phys., 13, 12495–12506, https://doi.org/10.5194/acp-13-12495-2013,
- 1135 2013.
- 1136 Wang, Z., Wu, Z., Yue, D., Shang, D., Guo, S., Sun, J., Ding, A., Wang, L., Jiang, J.,
- Guo, H., Gao, J., Cheung, H. C., Morawska, L., Keywood, M., and Hu, M.: New
- particle formation in China: Current knowledge and further directions, Sci. Total
- Environ., 577, 258–266, https://doi.org/10.1016/j.scitotenv.2016.10.177, 2017.
- Westervelt, D. M., Pierce, J. R., Riipinen, I., Trivitayanurak, W., Hamed, A., Kulmala,
- 1141 M., Laaksonen, A., Decesari, S., and Adams, P. J.: Formation and growth of nucleated
- particles into cloud condensation nuclei: Model-measurement comparison, Atmos.
- 1143 Chem. Phys., 13, 7645–7663, https://doi.org/10.5194/acp-13-7645-2013, 2013.

- Wu, Z. J., Poulain, L., Birmili, W., Größ, J., Niedermeier, N., Wang, Z. B., Herrmann,
- 1145 H., and Wiedensohler, A.: Some insights into the condensing vapors driving new
- particle growth to CCN sizes on the basis of hygroscopicity measurements, Atmos.
- 1147 Chem. Phys., 15, 13071–13083, https://doi.org/10.5194/acp-15-13071-2015, 2015.
- Wu, Z. J., Zheng, J., Shang, D. J., Du, Z. F., Wu, Y. S., Zeng, L. M., Wiedensohler, A.,
- and Hu, M.: Particle hygroscopicity and its link to chemical composition in the urban
- atmosphere of Beijing, China, during summertime, Atmos. Chem. Phys., 16,
- 1151 1123–1138, https://doi.org/10.5194/acp-16-1123-2016, 2016.
- 1152 Xia, C., Sun, J., Hu, X., Shen, X., Zhang, Y., Zhang, S., Wang, J., Liu, Q., Lu, J., Liu,
- 1153 S., and Zhang, X.: Effects of hygroscopicity on aerosol optical properties and direct
- radiative forcing in Beijing: Based on two-year observations, Sci. Total Environ., 857,
- 1155 159233, https://doi.org/10.1016/j.scitotenv.2022.159233, 2023.
- 1156 Xu, W. Y., Zhao, C. S., Ran, L., Deng, Z. Z., Liu, P. F., Ma, N., Lin, W. L., Xu, X. B.,
- 1157 Yan, P., He, X., Yu, J., Liang, W. D., and Chen, L. L.: Characteristics of pollutants and
- their correlation to meteorological conditions at a suburban site in the North China
- Plain, Atmos. Chem. Phys., 11, 4353–4369, https://doi.org/10.5194/acp-11-4353-2011,
- 1160 2011.
- 1161 Xu, W., Chen, C., Qiu, Y., Xie, C., Chen, Y., Ma, N., Xu, W., Fu, P., Wang, Z., Pan,
- 1162 X., Zhu, J., Ngcg, N. L., and Sun, Y.: Size-resolved characterization of organic
- aerosol in the North China Plain: New insights from high resolution spectral analysis,
- Environ. Sci. Atmos., 1, 346–358, https://doi.org/10.1039/d1ea00025j, 2021.
- 1165 Xu, W., Kuang, Y., Xu, W., Zhang, Z., Luo, B., Zhang, X., Tao, J., Qiao, H., Liu, L.,
- and Sun, Y.: Hygroscopic growth and activation changed submicron aerosol
- 1167 composition and properties in the North China Plain, Atmos. Chem. Phys., 24,
- 1168 9387–9399, https://doi.org/10.5194/acp-24-9387-2024, 2024.

- 1169 Xue, B., Kuang, Y., Xu, W., and Zhao, P.: Joint increase of aerosol scattering
- efficiency and aerosol hygroscopicity aggravate visibility impairment in the North
- 1171 China Plain, Sci. Total Environ., 839, 141163,
- https://doi.org/10.1016/j.scitotenv.2022.156279, 2022.
- Yang, P., Feng, Q., Hong, G., Kattawar, G. W., Wiscombe, W. J., Mishchenko, M. I.,
- Dubovik, O., Laszlo, I., and Sokolik, I. N.: Modeling of the scattering and radiative
- properties of nonspherical dust-like aerosols, J. Aerosol Sci., 38, 995-1014,
- https://doi.org/10.1016/j.jaerosci.2007.07.001, 2007.
- 1177 Yarragunta, Y., Srivastava, S., Mitra, D., and Chandola, H. C.: Source apportionment
- of carbon monoxide over India: a quantitative analysis using MOZART-4, Environ.
- 1179 Sci. Pollut. Res., 28, 8722–8742, https://doi.org/10.1007/s11356-020-11099-y, 2021.
- 1180 Yuan, L. and Zhao, C.: Quantifying particle-To-particle heterogeneity in aerosol
- 1181 hygroscopicity, Atmos. Chem. Phys., 23, 3195–3205,
- https://doi.org/10.5194/acp-23-3195-2023, 2023.
- In 183 Zhang, L., Sun, J. Y., Shen, X. J., Zhang, Y. M., Che, H., Ma, Q. L., Zhang, Y. W.,
- Zhang, X. Y., and Ogren, J. A.: Observations of relative humidity effects on aerosol
- light scattering in the Yangtze River Delta of China, Atmos. Chem. Phys., 15,
- 1186 8439–8454, https://doi.org/10.5194/acp-15-8439-2015, 2015.
- Zhang, R., Khalizov, A. F., Pagels, J., Zhang, D., Xue, H., and McMurry, P. H.:
- 1188 Variability in morphology, hygroscopicity, and optical properties of soot aerosols
- during atmospheric processing, Proc. Natl. Acad. Sci. U. S. A., 105, 10291–10296,
- https://doi.org/10.1073/pnas.0804860105, 2008.
- Zhang, R., Khalizov, A., Wang, L., Hu, M., and Xu, W.: Nucleation and growth of
- 1192 nanoparticles in the atmosphere, Chem. Rev., 112, 1957–2011,
- https://doi.org/10.1021/cr2001756, 2012.

- Zhang, R., Suh, I., Zhao, J., Zhang, D., Fortner, E. C., Tie, X., Molina, L. T., and
- 1195 Molina, M. J.: Atmospheric new particle formation enhanced by organic acids,
- Science (80-.)., 304, 1487–1490, https://doi.org/10.1126/science.1095139, 2004.
- Zhang, R., Wang, G., Guo, S., Zamora, M. L., Ying, Q., Lin, Y., Wang, W., Hu, M.,
- and Wang, Y.: Formation of Urban Fine Particulate Matter, Chem. Rev., 115,
- 3803–3855, https://doi.org/10.1021/acs.chemrev.5b00067, 2015.
- 1200 Zhang, Z., Xu, W., Zeng, S., Liu, Y., Liu, T., Zhang, Y., Du, A., Li, Y., Zhang, N.,
- Wang, J., Aruffo, E., Han, P., Li, J., Wang, Z., and Sun, Y.: Secondary Organic
- 1202 Aerosol Formation from Ambient Air in Summer in Urban Beijing: Contribution of
- 1203 S/IVOCs and Impacts of Heat Waves, Environ. Sci. Technol. Lett.,
- 1204 https://doi.org/10.1021/acs.estlett.4c00415, 2024.
- 1205 Zhao, C., Yu, Y., Kuang, Y., Tao, J., and Zhao, G.: Recent Progress of Aerosol
- 1206 Light-scattering Enhancement Factor Studies in China, Adv. Atmos. Sci., 36,
- 1207 1015–1026, https://doi.org/10.1007/s00376-019-8248-1, 2019.
- 1208 Zhao, G., Hu, M., Fang, X., Tan, T., Xiao, Y., Du, Z., Zheng, J., Shang, D., Wu, Z.,
- 1209 Guo, S., and Zhao, C.: Larger than expected variation range in the real part of the
- refractive index for ambient aerosols in China, Sci. Total Environ., 779, 146443,
- 1211 https://doi.org/10.1016/j.scitotenv.2021.146443, 2021.
- Zhao, S., Yu, Y., Li, J., Yin, D., Qi, S., and Qin, D.: Response of particle number
- concentrations to the clean air action plan: Lessons from the first long-term aerosol
- measurements in a typical urban valley in western China, Atmos. Chem. Phys., 21,
- 1215 14959–14981, https://doi.org/10.5194/acp-21-14959-2021, 2021.
- 1216 Zhu, Y., Shen, Y., Li, K., Meng, H., Sun, Y., Yao, X., Gao, H., Xue, L., and Wang, W.:
- 1217 Investigation of Particle Number Concentrations and New Particle Formation With
- 1218 Largely Reduced Air Pollutant Emissions at a Coastal Semi-Urban Site in Northern

- 1219 China, J. Geophys. Res. Atmos., 126, 1–20, https://doi.org/10.1029/2021JD035419,
- 1220 2021.
- Zieger, P., Weingartner, E., Henzing, J., Moerman, M., De Leeuw, G., Mikkilä, J., Ehn,
- 1222 M., Petäjä, T., Clémer, K., Van Roozendael, M., Yilmaz, S., Frieß, U., Irie, H., Wagner,
- 1223 T., Shaiganfar, R., Beirle, S., Apituley, A., Wilson, K., and Baltensperger, U.:
- 1224 Comparison of ambient aerosol extinction coefficients obtained from in-situ,
- 1225 MAX-DOAS and LIDAR measurements at Cabauw, Atmos. Chem. Phys., 11,
- 1226 2603–2624, https://doi.org/10.5194/acp-11-2603-2011, 2011.

Supporting Information for

2	Divergent changes in aerosol optical hygroscopicity and new
3	particle formation during <u>a</u> heatwaves of summer 2022
4 5 6	Yuhang Hao ^{1, a} , Peizhao Li ^{1, a} , Yafeng Gou ¹ , Zhenshuai Wang ¹ , Mi Tian ¹ , Yang Chen ² , Ye Kuang ³ , Hanbing Xu ⁴ , Fenglian Wan ¹ , Yuqian Luo ¹ , Wei Huang ⁵ , Jing Chen ^{1, 6, *}
7 8	¹ College of Environment and Ecology, Chongqing University, Chongqing 400045, China
9	² Center for the Atmospheric Environment Research, Chongqing Institute of Green and
10	Intelligent Technology, Chinese Academy of Sciences, Chongqing 400714, China
11	³ Institute for Environmental and Climate Research, Jinan University, Guangzhou 511443
12	China
13	⁴ Experimental Teaching Center, Sun Yat-sen University, Guangzhou 510275, China
14	⁵ National Meteorological Center, China Meteorological Administration, Beijing 100081,
15	China
16	⁶ Key Laboratory of Three Gorges Reservoir Region's Eco-Environment, Ministry of
17	Education, Chongqing University, Chongqing 400045, China
18 19 20	^a These authors contributed equally
21	Correspondence to: Jing Chen (chen.jing@cqu.edu.cn)
22	
23	
24	
25	Contents of this file
26	
27	Figures S1 to S1 <u>7</u> 6
28	Tables S1 to S3
29	References

S1. Site description

The observation site was located on the rooftop of a building (~15 m above the ground) in the main campus of Chongqing University (29.57°N, 106.46°E) in the urban center of Chongqing, southwest China. The site is characterized by a typical residential and commercial environment, mainly influenced by local emissions (e.g., traffic, cooking). All instruments were installed in an air-conditioned room, with the room temperature maintained about 25°C. The ambient air was sampled at a flowrate of 16.7 LPM through a PM_{2.5} impactor (model 2000-30EH, URG Inc.) and dried with a Nafion dryer (model MD-700, Perma Pure LLC), to achieve a low relative humidity level (RH <35%) prior to the online aerosol size distribution, optical and hygroscopic measurements. During the observation period, urban Chongqing suffered a rare heatwave. The mean temperature and relative humidity during the study period and the same period from 2011 to 2021 in urban Chongqing are given in Figure S1. Based on the method proposed by Nairn and Fawcett (2014), the Excess Heat Factor (EHF) metric was accordingly calculated for this study (Figure S2a).

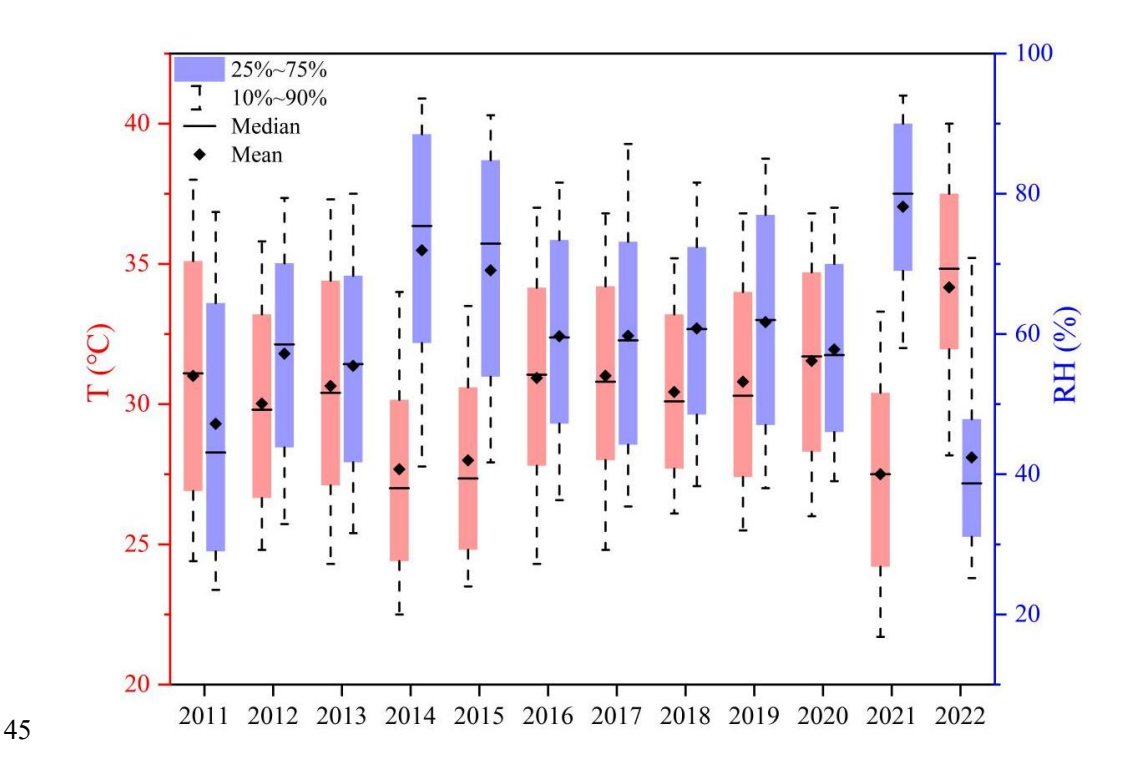


Figure S1. The variation trends of annual temperature and RH during the study period in 2022 and the same period from 2011 to 2021 in urban Chongqing.

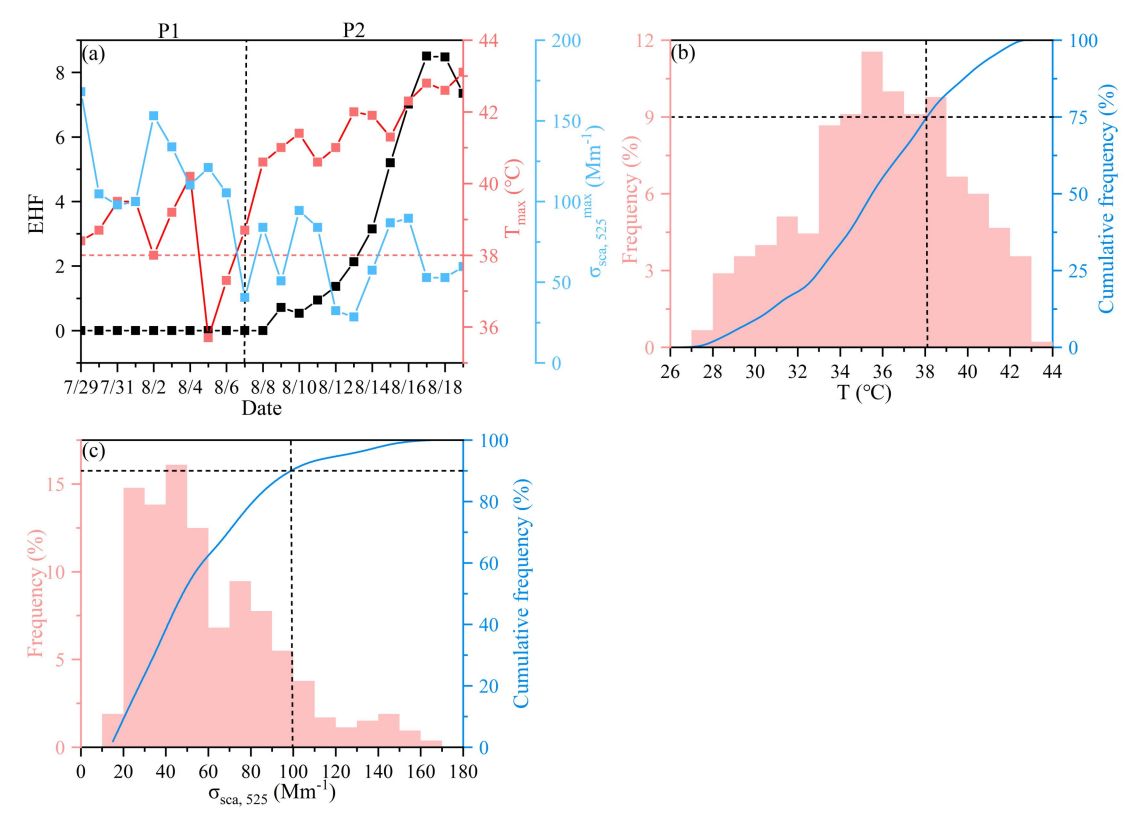


Figure S2. (a) Time series of calculated EHF, along with the daily maximum temperature (T_{max}) and dry $\sigma_{sca, 525}$ results, during the study period. The corresponding occurrence frequency and cumulative frequency of hourly (b) temperature and (c) $\sigma_{sca, 525}$ data records.

S2. Derivation of aerosol liquid water content (ALWC)

In this study, ALWC was determined as the discrepancy in aerosol volume concentration between the humidified and dry particles:

$$ALWC = V_{dry} \times (f v(RH) - 1)$$
(1)

where the dry aerosol volume concentration (V_{dry}) was estimated with the dry scattering coefficients at three wavelengths utilizing a machine learning method (Kuang et al., 2018). Given the dependence on aerosol hygroscopicity and size distribution, the aerosol volume growth factor ($f_V(RH)$) can be obtained from the observed f(RH) and SAE (a proxy of aerosol size distribution) with the humidified nephelometer system (Kuang et al., 2018). Accordingly, the fraction of aerosol water content (f_W) upon hydration could be expressed as:

$$f = \frac{ALWC}{ALWC + V_{dry}}$$
 (2)

Both dry and humidified nephelometers were calibrated before the measurement for the zero/span check with the particle-free air/standard gas (R134a), following standard calibration procedures. More detailed descriptions about the home-built humidified nephelometer system can refer to Kuang et al. (2017, 2020) and Xue et al. (2022).

S3. Offline particle sampling and chemical analysis

69

70

71

72

73

74

75

76

77

78

79

80

81

82

83

84

85

86

87

88

are depicted in Figure S3.

Total suspended particle (TSP) filter samples were collected by a moderate volume air sampler at a flow rate of 200 L/min from August 5 to 19, 2022. Daily (from 9:30 a.m. to 9:00 a.m. of the next day) integrated ambient TSP samples were collected on prebaked (600°C, 5h) quartz-fiber filters (90 mm, Whatman) for water-soluble ions, organic carbon (OC), and elemental carbon (EC) analysis. Water-soluble inorganic anions (i.e., SO_4^{2-} , NO_3^{-} , Cl^{-} and F^{-}) and cations (i.e., NH_4^{+} , Na⁺, Mg²⁺, Ca²⁺ and K⁺) were quantified using an ion chromatograph analyzer (Dionex 600, Dionex, USA) following standard procedures (Peng et al., 2019; Wang et al., 2018). Elemental carbon (EC) and organic carbon (OC) in the collected TSP samples were analyzed using a DRI Model 2015 Multi-wavelength Carbon Analyzer (Magee Scientific, USA). The methodology for OC/EC analysis was based on the thermal-optical reflectance (TOR) method following the Interagency Monitoring of Protected Visual Environments (IMPROVE-A) protocol, as shown in Chow et al. (2007, 2011) and Peng et al. (2020). The secondary organic carbon (SOC) can be estimated with the obtained OC and EC data according to the EC-tracer method (Castro et al., 1999; Strader et al., 1999), details of which was also available in our previous study (Hao et al., 2024). The chemical components mass concentration and mass fraction in TSP, as well as the PM_{2.5} (PM₁₀) mass concentration and the ratio of SOC/TOC during the study period

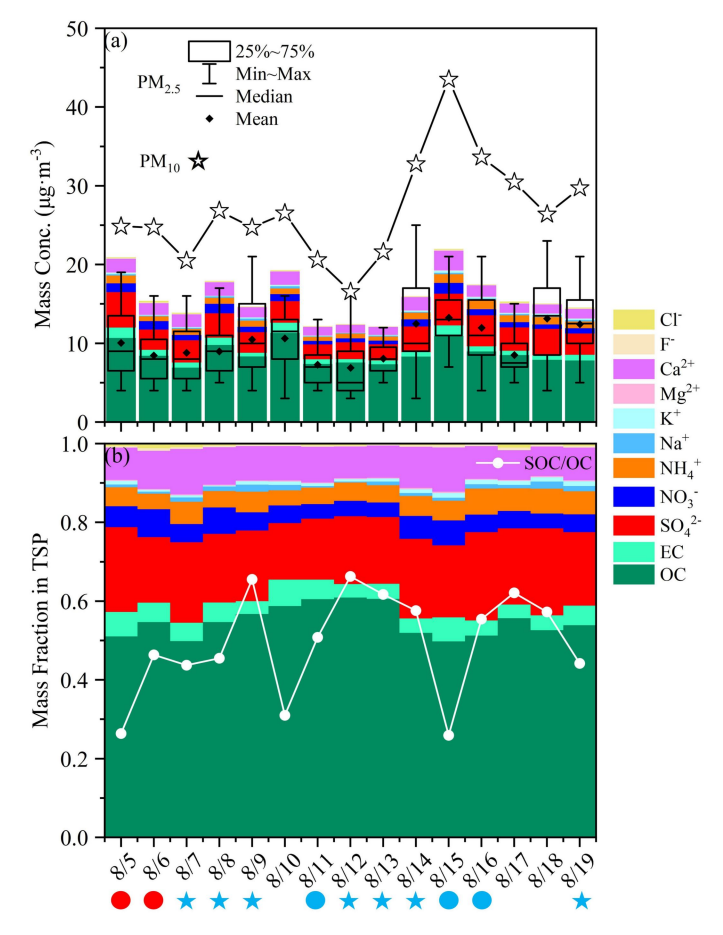


Figure S3. The mass concentration **(a)** and mass fraction **(b)** of chemical components in TSP (total suspended particulates) during the study period. The black stars, box plots and white line stands for daily mean PM₁₀, PM_{2.5} and SOC/OC, respectively. The red or blue circle symbols below specific dates represent the P1 or P2 non-event days, and the blue stars represent the P2 NPF_{clean, HW} days.

S4. Meteorological and air quality data

All the contemporary hourly meteorological datasets including relative humidity (RH), temperature (T), visibility (VIS), wind speed (WS), wind direction (WD), precipitation were obtained from the Integrated Surface Database from the U.S. National Centers for Environmental Information (https://ncdc.noaa.gov/isd) (Wan et al., 2023; Xu et al., 2020), and the mixing layer height (MLH) data were achieved from China Meteorological Administration in this study. Ultraviolet (UV) radiation data were downloaded from European Centre for Medium-Range Weather Forecasts (https://cds.climate.copernicus.eu/).

Hourly air pollutant datasets including $PM_{2.5}$, PM_{10} , NO_2 , SO_2 , CO and O_3 were achieved from the China National Environmental Monitoring Center (http://www.cnemc.cn/en). The gas-phase sulfuric acid, known as the most ubiquitous and key precursor for NPF, was estimated with the UVB (UVB = 5%UV, Fitsiou et al., 2021) and SO_2 concentration (Lu et al., 2019):

$$H_2SO_4 = 280.05 \times UVB^{0.14} \times SO_2^{0.40}$$
 (3)

S5. Particle number size distribution measurements

During the field observation, every 3-min PNSD and particle volume size distribution (PVSD) was measured by a SMPS, which consisted of a soft X-Ray neutralizer (model 3088, TSI Inc.), a differential mobility analyzer (model 3081, TSI Inc.), and a condensation particle counter (model 3775, TSI Inc.) (Dominick et al., 2018; Rissler et al., 2006). The SMPS was operated at a sheath/sample flow rate of 3.0/0.3 LPM, and the detected size range was 14.1-710.5 nm with 110 size bins. Data inversion of measured particle size distributions was achieved with the Aerosol Instrument Manager software (AIM, TSI Inc.), including the multiple charge and diffusion corrections (Denjean et al., 2015; Rosati et al., 2022).

The aerosol effective radius (R_{eff}) is a crucial parameter regulating optical properties (e.g., light scattering) of the aerosol population (Hansen and Travis, 1974; Grainger et al., 1995). It can be calculated with the measured size distribution as below (Hansen and Travis, 1974; Grainger et al., 1995):

$$R_{eff} = \frac{\int D_P^3 n(\log D_P) \operatorname{dlog} D_P}{\int D_P^2 n(\log D_P) \operatorname{dlog} D_P}$$
(4)

where $n(log D_P)$ is the particle number size distribution in log scale.

Using the measured PNSD data, NPF events were identified according to the criteria raised by Dal Maso et al. (2005), and the key parameters related to NPF events (e.g., formation rate (FR) and growth rate (GR) of new particles, condensation sink (CS) and coagulation sink (CoagS)) could be derived following the methodologies introduced by Dal Maso et al. (2005) and Kulmala et al. (2012).

The specific dates for NPF and non-event classifications were summarized in Table S1, and the frequencies of NPF, non-event and Undefined days during both periods were shown in Figure S4a. By using the HYSPLIT (Hybrid Single-Particle Lagrangian Integrated Trajectory) 4 model developed by NOAA (Stein et al., 2015), the 48-h and 72-h back trajectories of air masses at 500 or 1000 m altitude above the observation site during this study period were calculated and visualized by MeteoInfoMap (version 3.9.9; Figure S4b) (Chen et al., 2021; Tian et al., 2021; Wang, 2014).

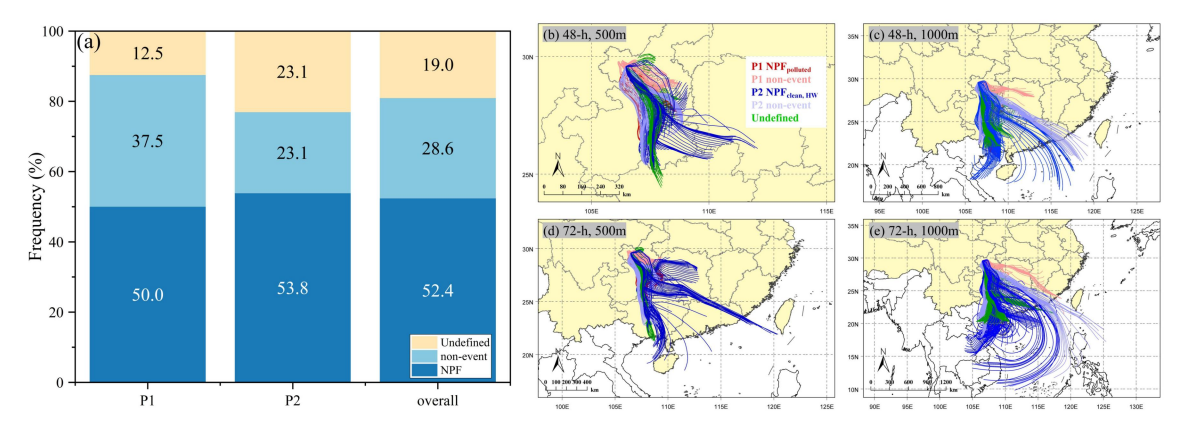


Figure S4. (a) The occurrence frequencies of NPF, non-event and Undefined days during P1, P2 and the whole observation periods. **(b-e)** The 48-h and 72-h air-mass back trajectories at 500 or 1000 m altitude during the study period.

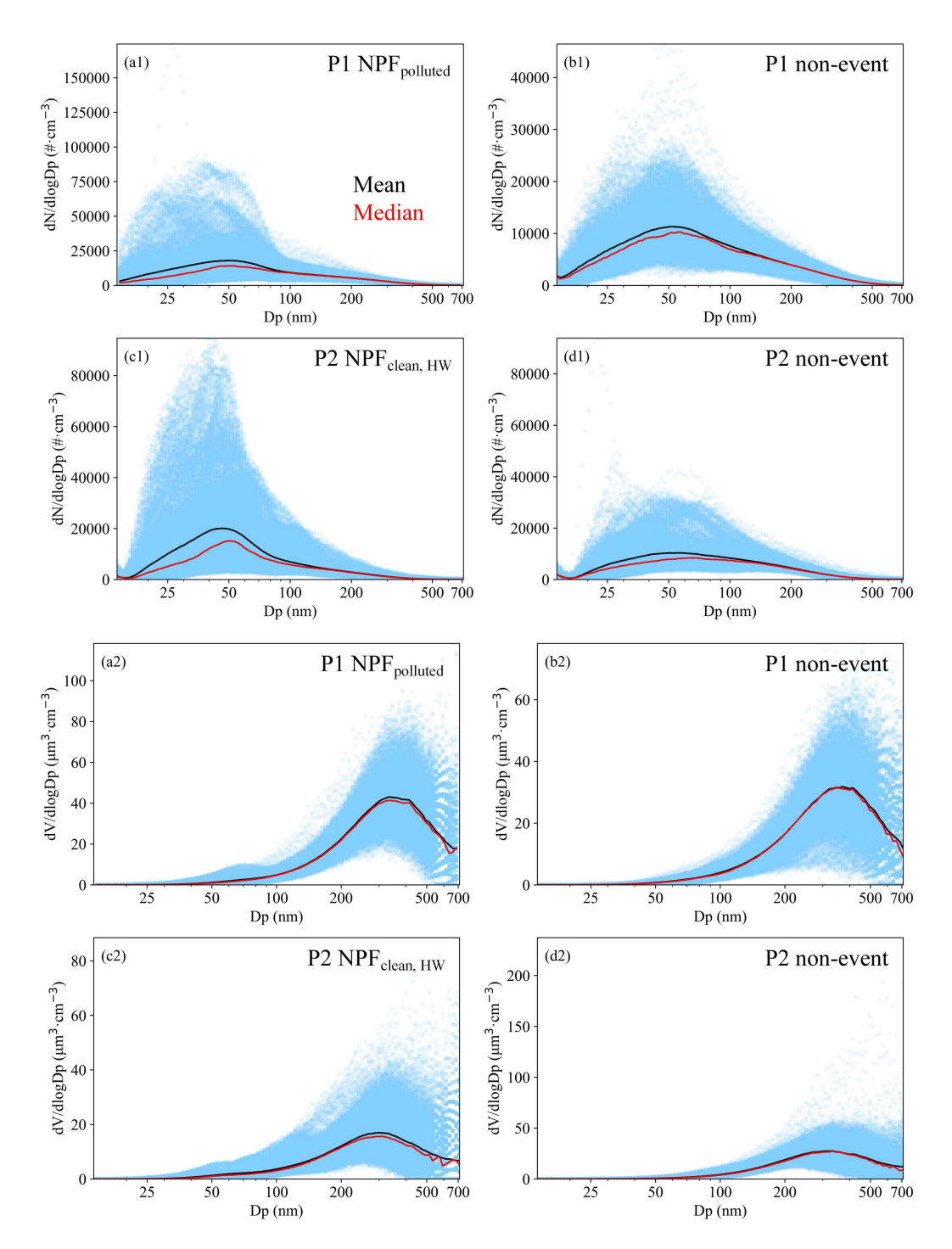


Figure S5. The PNSDs (a1-d1) and PVSDs (a2-d2) for different event categories. The black and red lines represent the mean and median values, respectively.

The diurnal variations of PNSD, R_{eff} , particle mode diameter (D_{mode}), as well as CS, were given in Figure S6.

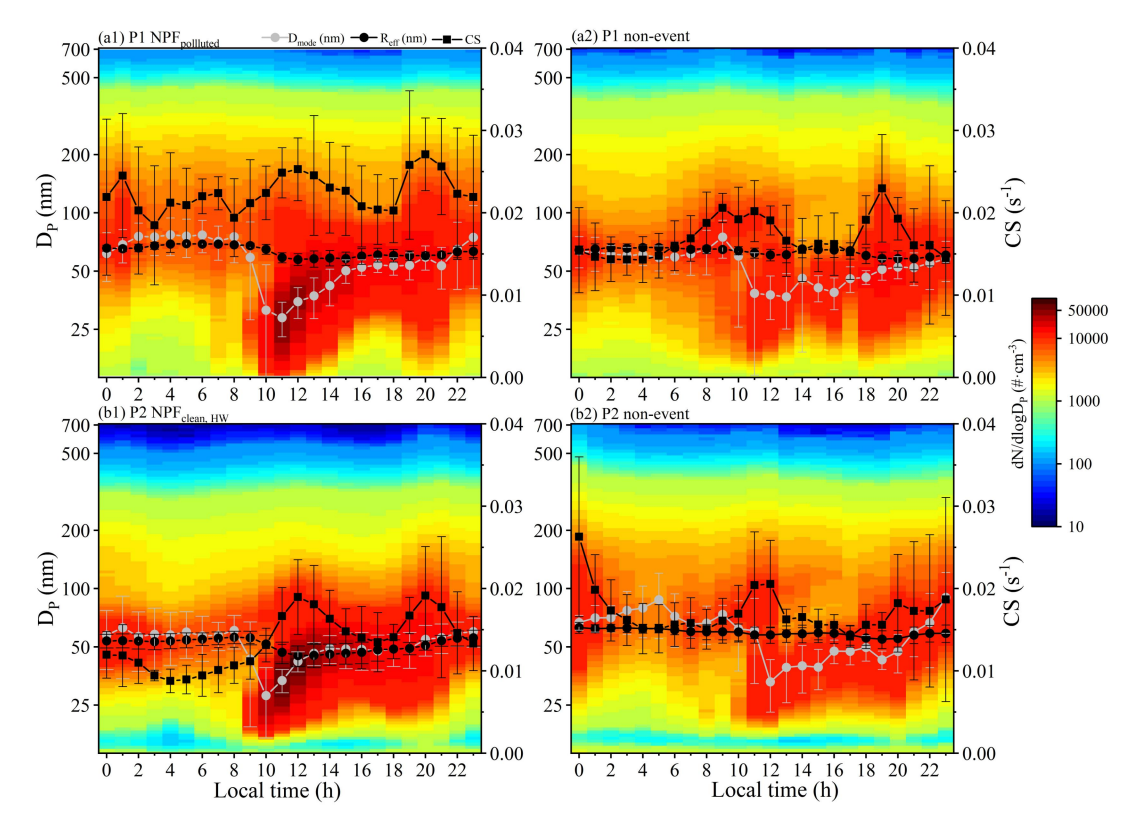


Figure S6. Diurnal variations of PNSDs, D_{mode} , R_{eff} , and CS during P1 and P2 NPF days (a1, b1) and non-event days (a2, b2), the error bars stand for \pm one standard deviations.

147148

The PNSD is typically categorized into three modes: the nucleation mode (D_p <25 nm), Aitken mode (25-100 nm), and accumulation mode (D_p >100 nm) (Zhu et al., 2021). The number concentrations and volume concentrations of different mode particles for different event categoriesthe corresponding NPF and non-event days during both P1 and P2 periods are shown in Figure S7. The diurnal variations of aerosol number and volume concentrations, as well as R_{eff} , for different modes on NPF event days are illustrated in Figure S8.



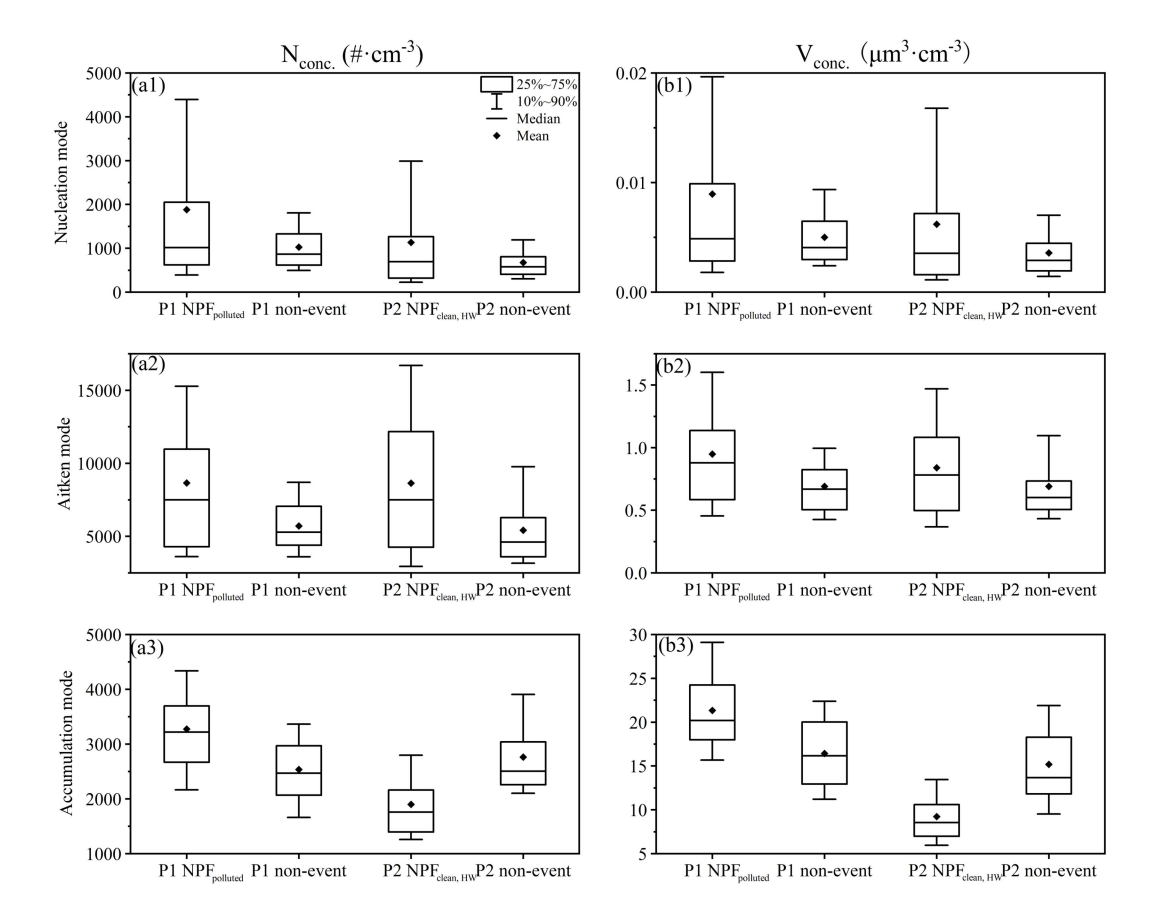


Figure S7. The number concentrations (left column: a1-a3) and volume concentrations (right column: b1-b3) of different mode particles for <u>the corresponding different event eategories NPF</u> and non-event days during both P1 and P2 periods.

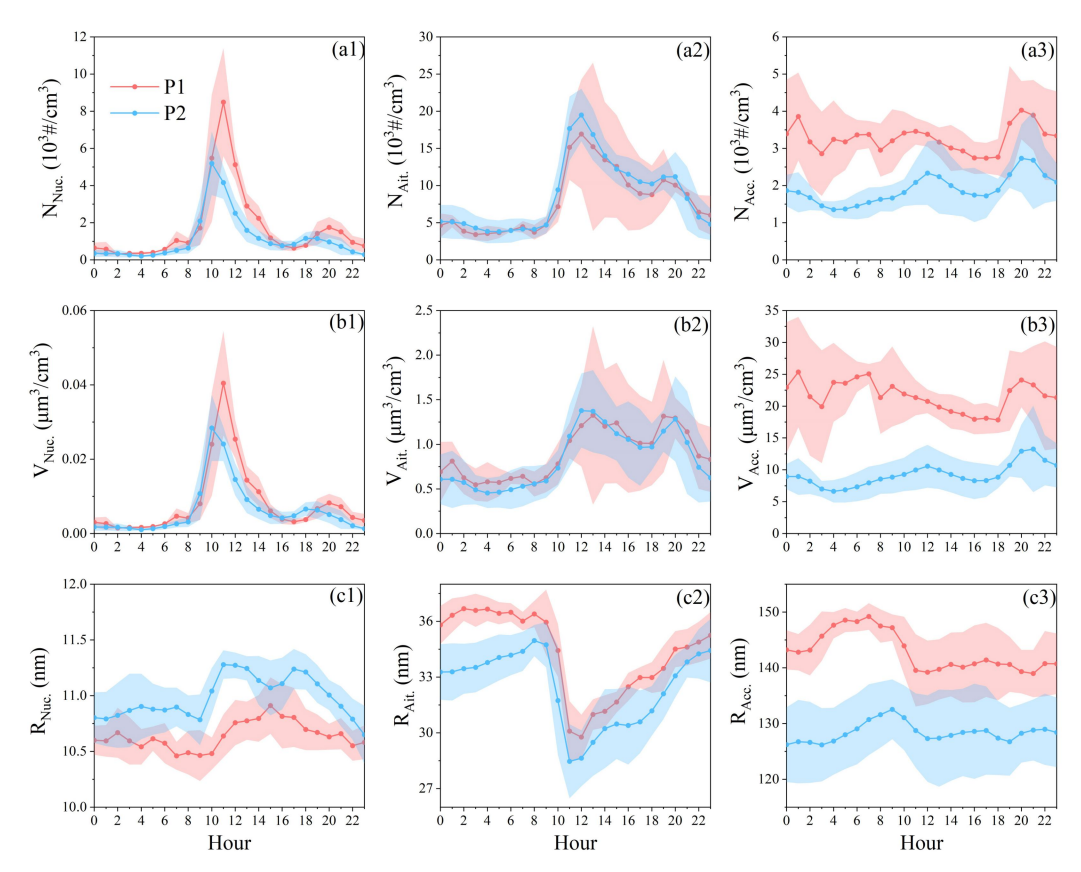


Figure S8. Diurnal variations of the number (a1-a3), volume (b1-b3) concentration and effective radius (c1-c3) of nucleation mode (left column), Aitken mode (middle column), and accumulation mode (right column) particles on NPF event days during P1 (red line) and P2 (blue line) periods. The shaded areas stand for the corresponding \pm 1 σ standard deviations.

The specific start and end time of NPF, along with the subsequent growth end time during NPF events were displayed in Figure S9. The NPF event end time is defined as the moment when the formation of new nucleation-mode particles (diameter <25 nm) ceases, specifically identified by the absence of a notable increase in sub-25 nm particles (Dal Maso et al., 2005; Hamed et al., 2007; Kerminen et al., 2018). The growth event end time refers to the time when the newly formed particles stop growing, typically due to the depletion of low-volatility vapors or particle coagulation (Dal Maso et al., 2005; Kerminen et al., 2018). This can be observed as the stabilization of particle diameters in the Aitken/accumulation mode, marked by a flattening of the growth trajectory in the PNSD plot (Figure 1i).

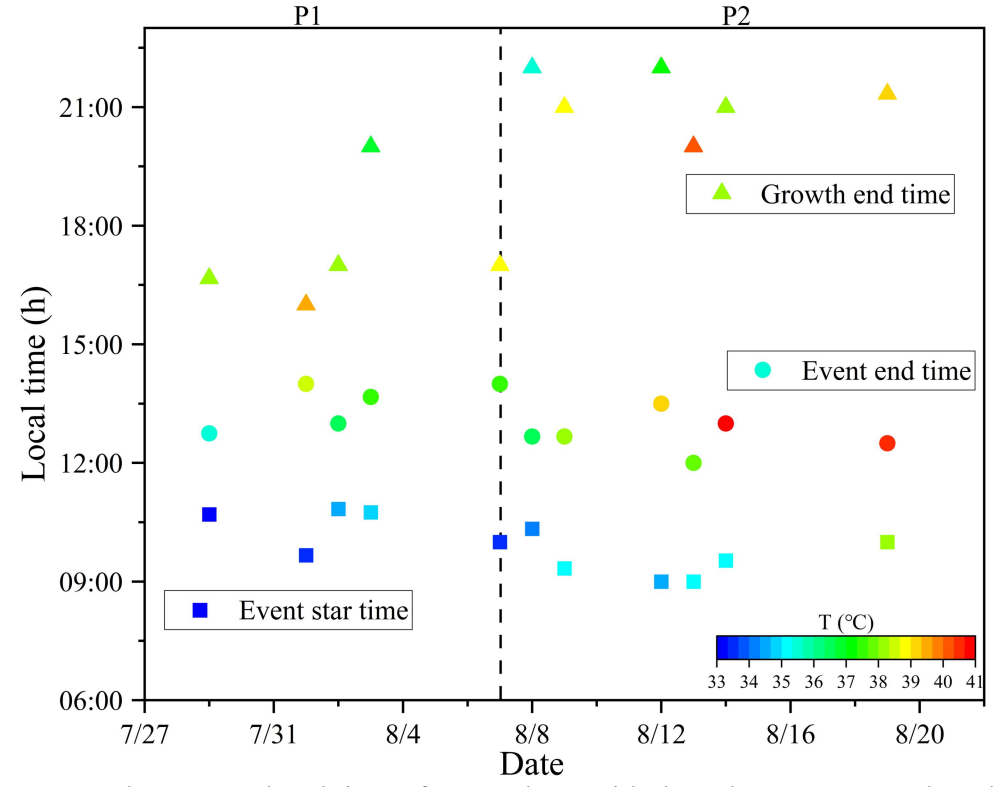


Figure S9. The start and end time of NPF, along with the subsequent growth end time and their corresponding temperature levels during NPF events.

S6. Diurnal variations of humidified nephelometer system related parameters on non-event days during both P1 and P2 periods

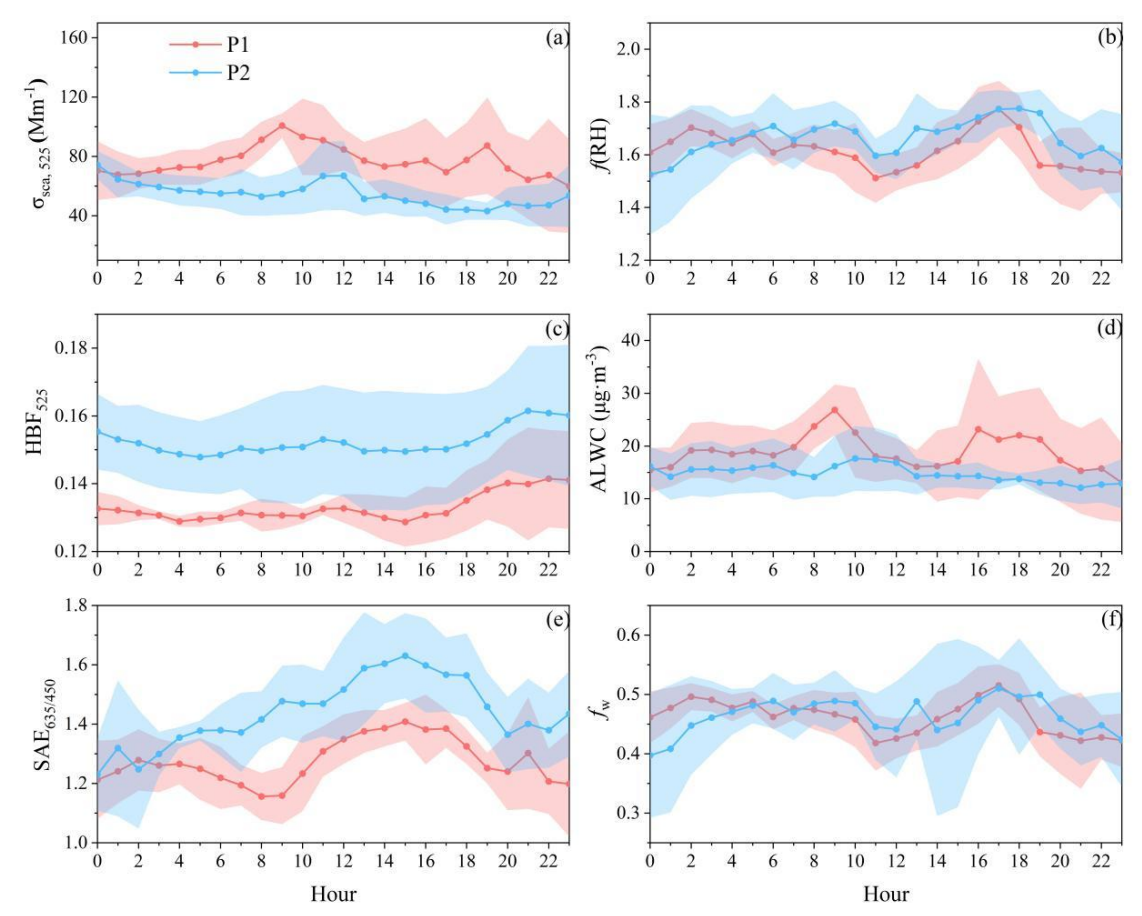


Figure S10. Diurnal variations of $\sigma_{sca, 525}$ (a), f(RH) (b), HBF₅₂₅ (c), ALWC (d), SAE_{635/450} (e) and f_W (f) on non-event days during P1 (red line) and P2 (blue line) periods. The shaded areas stand for the corresponding $\pm 1\sigma$ standard deviations.

S7. Calculation of σ_{sca} and HBF with the Mie theory and measured PNSD

188

189

190

191

192

193

194

195

196

197

198

199

200

201

202

203

204

205

206

207

208

209

210

211

212

213

214

215

216

The size-dependent efficiencies of σ_{sca} , σ_{bsca} and HBF in dry conditions, as well as the corresponding enhancements in these efficiencies of a single particle upon hydration at $\lambda = 525$ nm could be simulated using the Mie model. Aerosol diameter growth factor (g(RH)) is normally determined by the aerosol hygroscopicity parameter κ (Brock et al., 2016; Tan et al., 2024). The bulk aerosol $\kappa_{f(RH)}$ of this study could be derived from the f(RH) measurements based on the method proposed by Kuang et al. (2017). The aerosol population was typically divided into the ultrafine (D_p <100 nm; Uf.) and accumulation $(D_p \ge 100 \text{ nm}; Acc.)$ modes (Fig. S5). Although the size-resolved κ results were unavailable, the mean κ_i for both Uf. and Acc. mode particles could be roughly estimated assuming that $\kappa_{f(RH)}$ is a linear combination of volume-weighted κ_i for different modes (Hong et al., 2024). Since the hygroscopicity for Uf. mode was generally weaker (Chen et al., 2012; Petters and Kreidenweis, 2007), the mean $\kappa_{\rm Uf}$ was defined to be half of the measured bulk $\kappa_{f(RH)}$, and $\kappa_{Acc.}$ can be derived from the bulk $\kappa_{f(RH)}$ with the measured VF_{Uf.} and VF_{Acc.} Consequently, the corresponding g(RH) for both Uf. and Acc. modes can be calculated with the κ -Köhler theory. The complex refractive index is another critical input parameter for the Mie model, with the real part of complex refractive index (n)determining the aerosol light scattering ability. Under the assumption of a fixed *n* for dry aerosols ($n_{\text{dry}} = 1.53$) in this study, the volume-weighted n of hydrated particles can be derived with n_{dry} and f(RH)-derived volume fractions of uptake water, f_W and the n of pure water (1.33; Jung et al., 2016) (Chen et al., 2012). Hence, the efficiencies of σ_{sca} , σ_{bsca} and HBF after hygroscopic growth could be simulated with the time-averaged dry PNSD, the mean g(RH) of Uf. Mode (1.15) and Acc. mode (1.27), and the mean n of humidified aerosols (1.44) for the observation period. The theoretically simulated results are displayed in Figure S11. A good correlation between SMPS-determined particle volume concentration and the measured $\sigma_{sca, 525}$ is also observed in Figure S12. The size-resolved $\sigma_{sca, 525}$

A good correlation between SMPS-determined particle volume concentration and the measured $\sigma_{sca, 525}$ is also observed in Figure S12. The size-resolved $\sigma_{sca, 525}$ distributions and size-resolved $\sigma_{sca, 525}$ cumulative frequency distribution on NPF event (non-event) days during P1 and P2 periods are displayed in Figure S13.

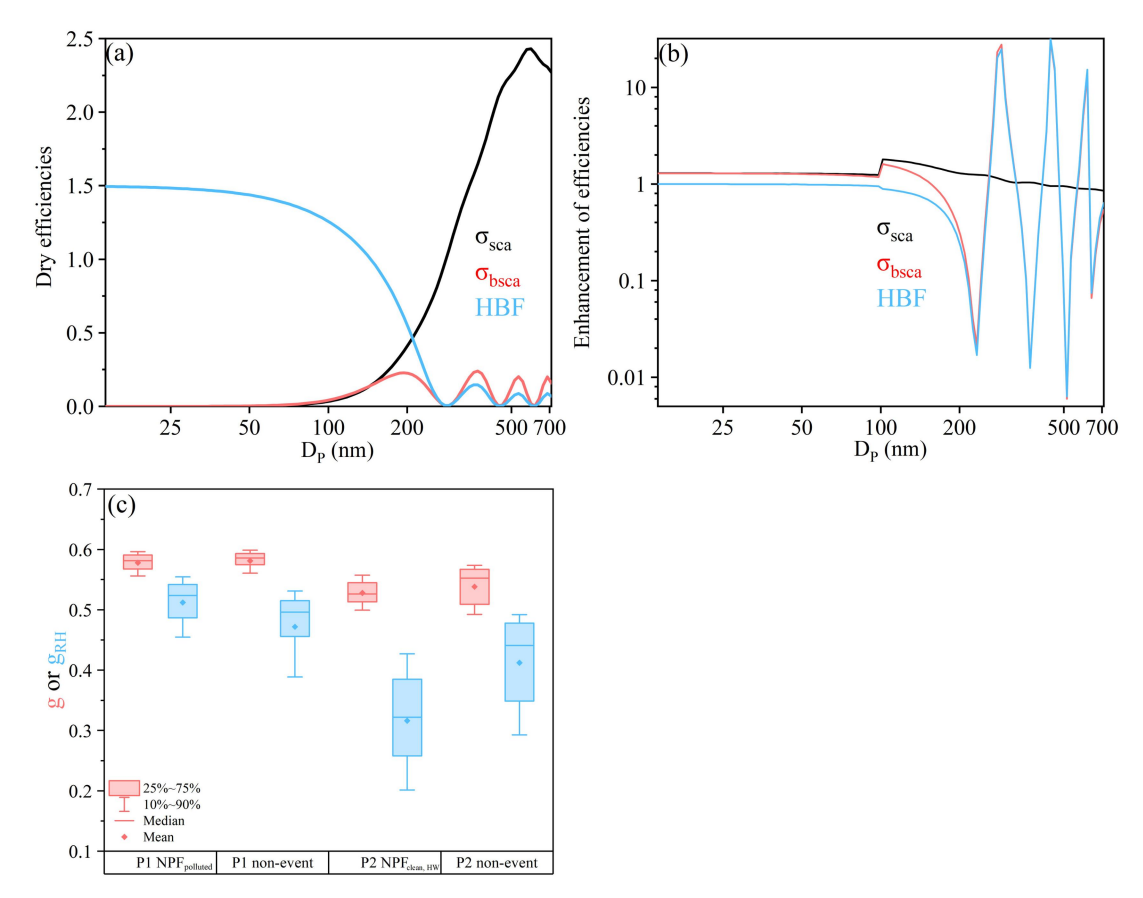


Figure S11. Size-dependent efficiencies of **(a)** light scattering (the black line), backscattering (the red line) and HBF (the blue line) in dry conditions, as well as **(b)** the enhancements in corresponding efficiencies of light scattering (the black line), backscattering (the red line) and HBF (the blue line) at $\lambda = 525$ nm simulated with the Mie theory. **(c)** The box plots of the HBF₅₂₅ (HBF_{525, RH}) derived asymmetry factor g (g_{RH}).

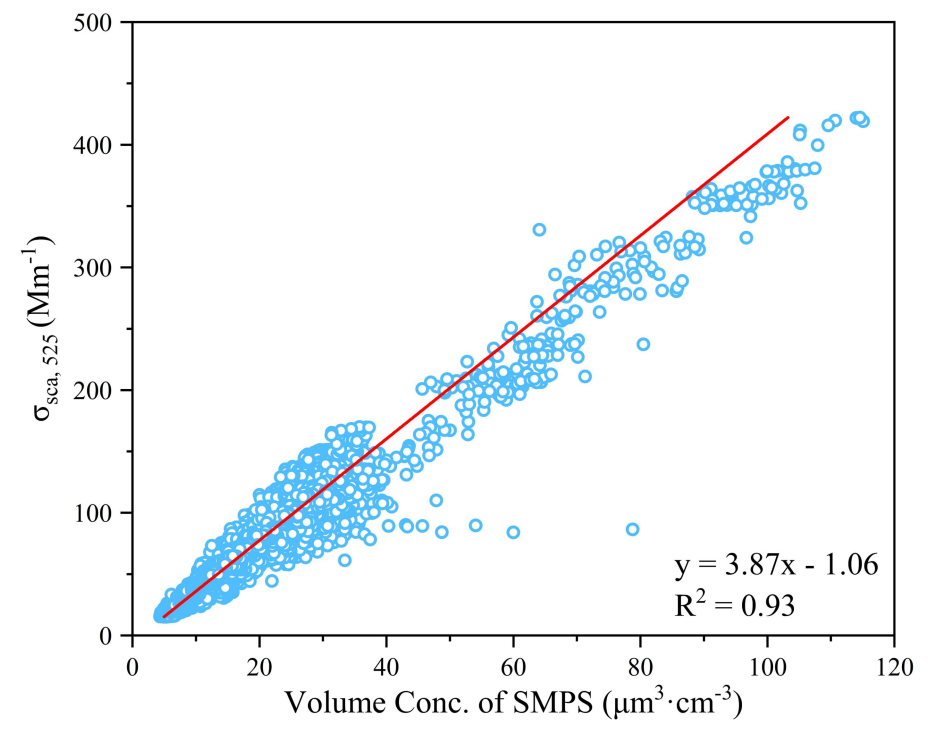


Figure S12. Correlation between the particle volume concentration determined by SMPS and $\sigma_{sca, 525}$ measured by the humidified nephelometer system during the study period. The solid line represents the fitting line.

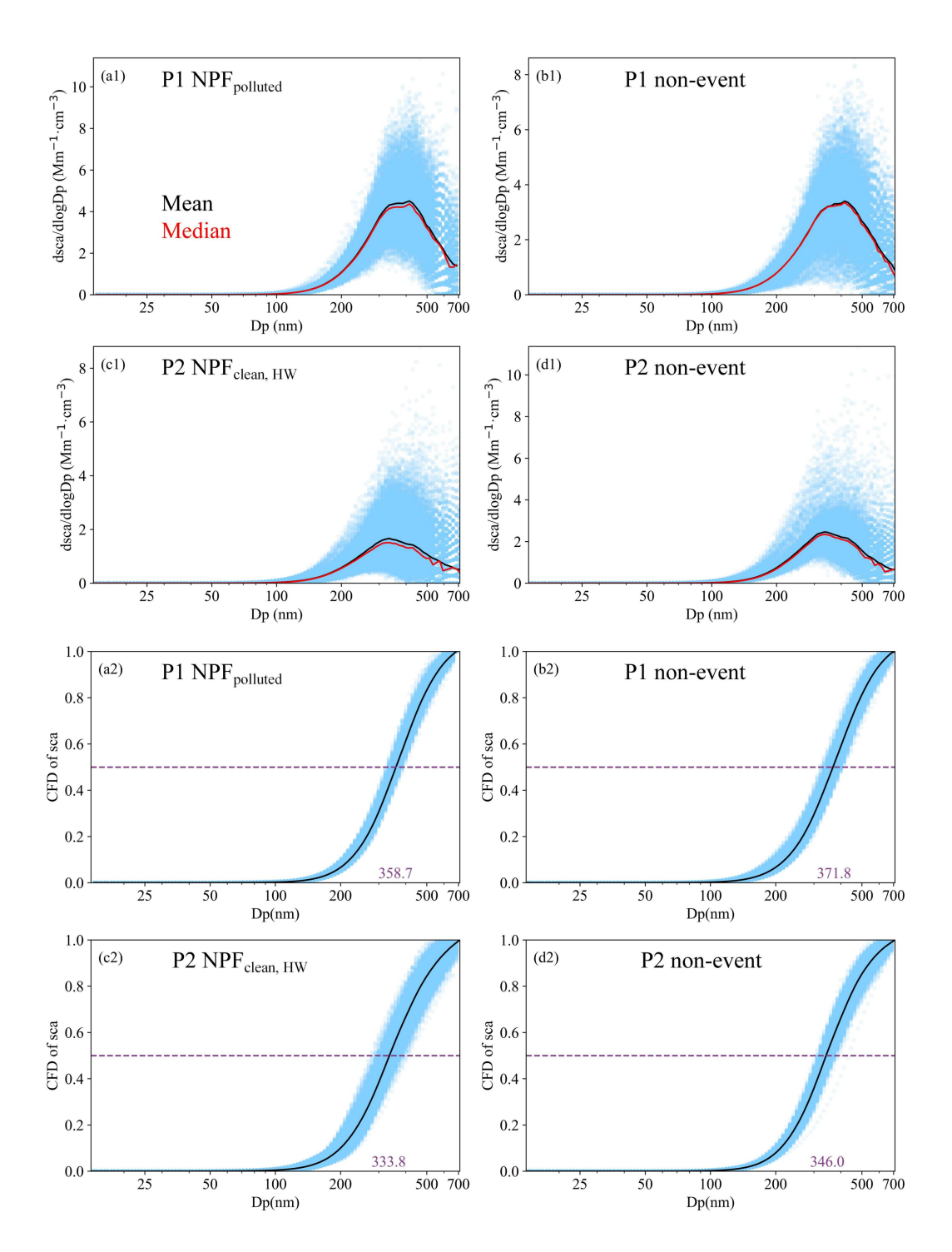


Figure S13. The size-resolved σ_{sca} , 525 distributions (a1-d1) and size-resolved σ_{sca} , 525 cumulative frequency distribution (a2-d2) for different event categories. The black and red lines represent the mean and median values, the purple dashed line and the purple numbers on the abscissa represent the 50% cumulative frequency and the corresponding particle size (D₅₀), respectively.

S8. Correlation coefficients between different PNSD-related parameters, temperature, O₃/O_x, aerosol optical and hygroscopic properties on NPF (non-event) days during either P1 or P2 period

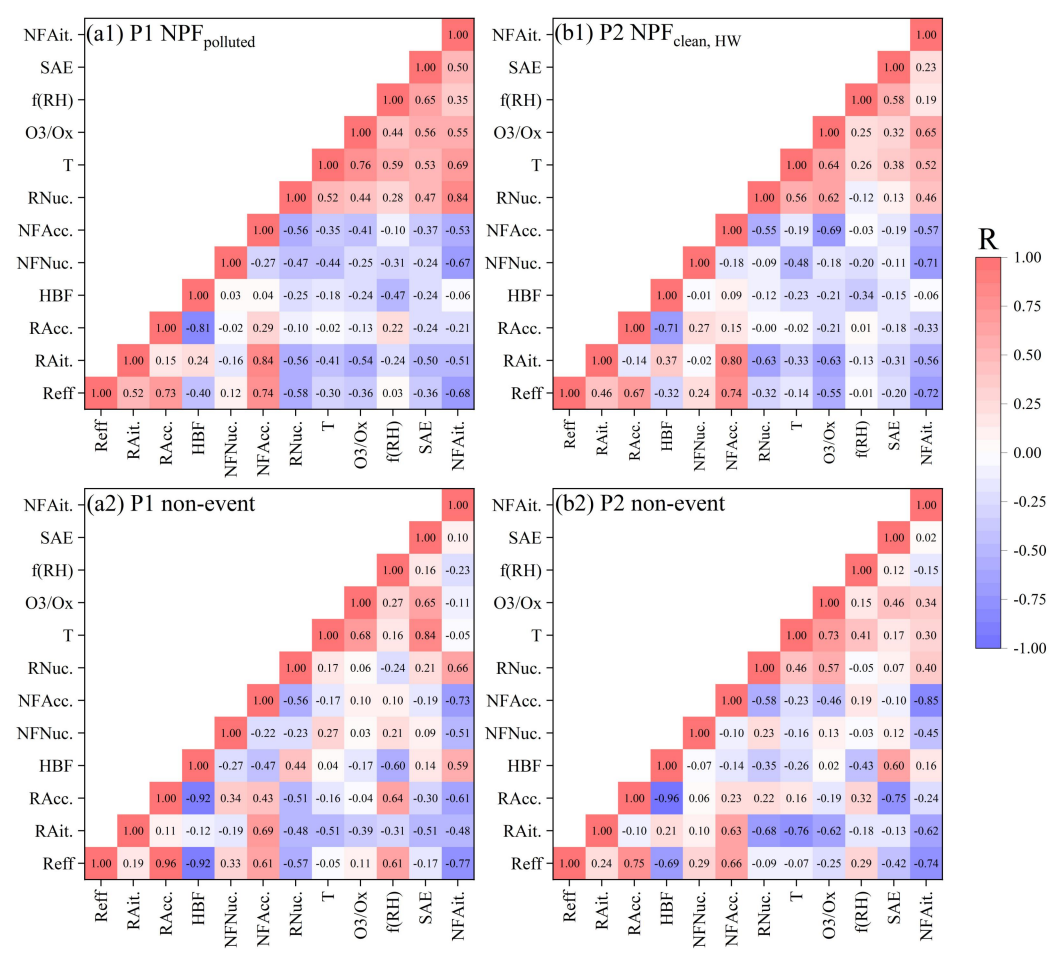


Figure S14. Correlation coefficients between different PNSD-related parameters (R_{eff}, R_{Nuc.}, R_{Ait.}, R_{Acc.}, NF_{Nuc.}, NF_{Ait.}, NF_{Acc.}), temperature (T), O₃/O_X, HBF, SAE, and *f*(RH) during NPF events (**a1**, **b1**) and non-event days (**a2**, **b2**) over the 08:00-22:00 LT time window.

S9. The sensitive test on dependences of the HBF₅₂₅, RH/HBF₅₂₅ ratio on the aerosol size distribution, hygroscopic growth, and complex refractive index

To investigate the distinct influences of PNSD, optical and hygroscopic properties on the HBF_{525, RH}/HBF₅₂₅ ratio, a sensitivity analysis with the measured data specifically for both P1 and P2 NPF days using the Mie model was conducted. Aerosol number size distributions could be assumed as a combination of multi-lognormal distribution functions, with each mode representing a distinct particle population (Hussein et al., 2004):

$$\frac{dN}{d\log D_P} = \sum_{i=1}^{n} \frac{N_{t,i}}{\sqrt{2\pi} \log \sigma_{g,i}} \exp \left[-\frac{(\log D_P - \log \overline{D_{Pg,i}})^2}{2 \log^2 \sigma_{g,i}} \right]$$
 (5)

Where the three representative parameters, i.e., the total number concentration $N_{t, i}$, the geometric standard deviation (GSD) $\sigma_{g, i}$, and the geometrical mean diameter $D_{Pg, i}$, can be used to characterize an individual mode i; and n is the number of individual modes (Hussein et al., 2004). In this study, the measured PNSD data on NPF days during P1 and P2 periods were normally fitted into two modes: the predominant Uf. mode and the other one dominated by Acc. Mode particles (Fig. S5). The geometrical mean diameter of fitted ultrafine mode (GMD_{Uf}) from NPF_{clean, HW} onset until 19:00 LT was shown in Figure S15.

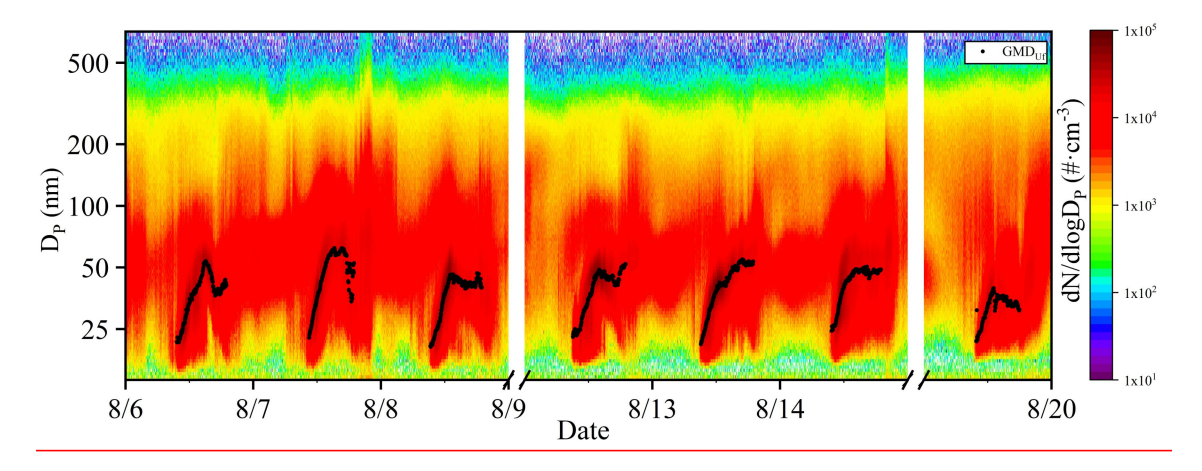


Figure S15. Overview of the measured PNSD and geometrical mean diameter of the fitted ultrafine mode (GMD_{Uf}; black dots) during the P2 NPF_{clean, HW} days.

Hence, nine parameters were employed in the Mie model: four parameter pairs (D_{Pg} , GSD, N_t and g(RH)) for both Uf. and Acc. mode particles, along with the mean n of the bulk aerosol population upon hydration. Further, the HBF₅₂₅, RH/HBF₅₂₅ can be simplified as a function of aerosol size distribution (i.e., D_{Pg} , GSD, N_t), water uptake (e.g., g(RH)), and n as below:

267
$$HBF_{525, RH}/HBF_{525} = f(D_{Pg}, GSD, N_{t}, g(RH), n)$$
 (6)

The influence of a specific parameter on the HBF₅₂₅, RH/HBF₅₂₅ was evaluated by fixing all the other parameters at their measured mean values and computing HBF₅₂₅, RH/HBF₅₂₅ ratios across the range of this target parameter.

The measured mean value and variation range of each parameter were summarized in Table S3. The ranges of D_{Pg} , GSD, N_t and g(RH) were determined based on field measurements of this study. Zhao et al. (2021) reported that n of diverse aerosol populations could range from 1.36 to 1.78 across different Chinese cities, and this study constrained n to vary from 1.3 (nearly pure water of 1.33; Jung et al., 2016) to 1.8 (similar to black carbon of approximately 1.87; Schkolnik et al., 2007) in the modeling framework. The results are shown in Figures S156-167.

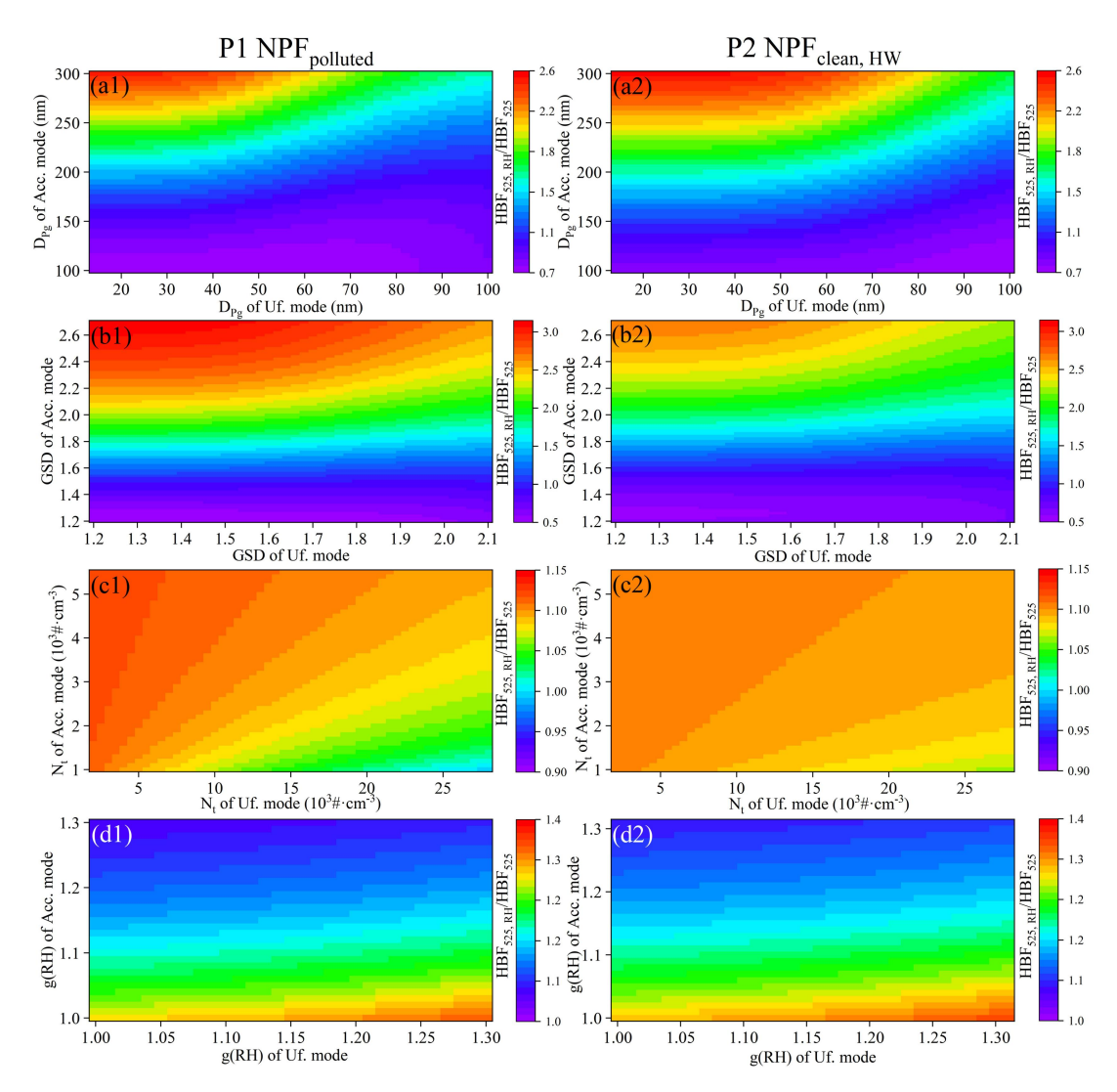


Figure S156. The relationships between the HBF₅₂₅, RH/HBF₅₂₅ ratios and the D_{pg} (a), GSD (b), N_t (c), g(RH) (d) of two modes particleas. The left (right) column was corresponding to the P1 NPF_{polluted} (P2 NPF_{clean, HW}) days.

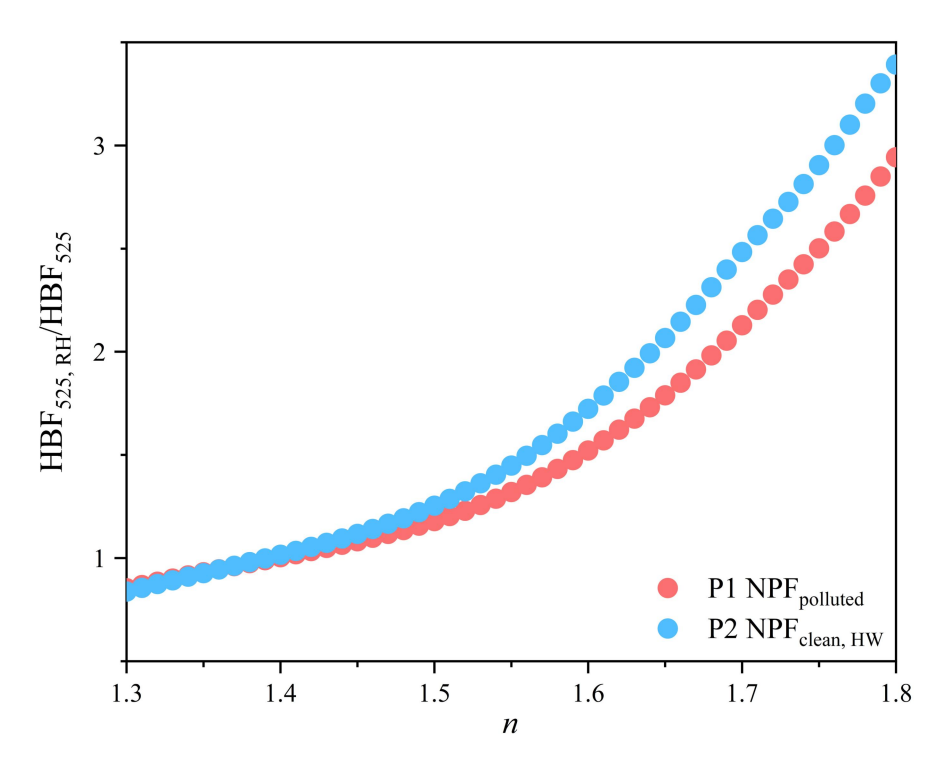


Figure S167. The variations of the HBF_{525, RH}/HBF₅₂₅ ratios with n on the P1 and P2 NPF days.

Table S1. Specific dates for different event categories during P1 and P2 periods.

Period	Category	Date		
	$NPF_{polluted}$	7.29, 8.1-3		
P1	non-event	8.4-6		
	Undefined	7.30-31		
	$\mathrm{NPF}_{\mathrm{clean,HW}}$	8.7-9, 8.12-14, 8.19		
P2	non-event	8.11, 8.15-16		
	Undefined	8.10, 8.17-18		

Table S2. A summary (avg. \pm std.) of the humidified nephelometer system determined parameters ($\sigma_{sca, 525}$, f(RH), ALWC, HBF₅₂₅, SAE_{634/450}, f_W), SMPS-relevant parameters (N_{conc.}, V_{conc.}, R_{eff}, NF_{Acc.}, VF_{Acc.}), meteorological parameters (T, RH, WS, VIS, MLH), air pollutants (PM_{2.5}, NO₂, SO₂, O₃, CO, O₃/O_X), NPF events related parameters (FR, GR, CS, CoagS), HBF₅₂₅, RH/HBF₅₂₅ and $f_{RF}(RH)$ on NPF event and non-event days, as well as overall mean results during P1 and P2 periods.

	N	PF non-event		Overall		
	P1 P2		P1 P2		P1 P2	
$\sigma_{sca,525}(Mm^{\text{-}1})$	103.8 ± 30.4	33.2 ± 11.7	76.7 ± 23.5	54.7 ± 17.6	88.0 ± 29.3	41.2 ± 16.0
f(RH)	1.64 ± 0.10	1.71 ± 0.13	1.62 ± 0.10	1.66 ± 0.12	1.61 ± 0.12	1.71 ± 0.15
ALWC (μg·m ⁻³)	25.9 ± 6.6	10.2 ± 3.2	18.9 ± 7.5	14.8 ± 4.5	21.4 ± 7.8	12.0 ± 3.9
HBF ₅₂₅	0.134 ±	$0.157 \pm$	0.133 ±	0.152 ±	0.135 ±	$0.153 \pm$
	0.007	0.011	0.008	0.016	0.008	0.012
SAE _{635/450}	1.31 ± 0.10	1.48 ± 0.13	1.27 ± 0.11	1.44 ± 0.16	1.29 ± 0.12	1.47 ± 0.16
fw (104#	0.47 ± 0.04	0.48 ± 0.05	0.46 ± 0.04	0.46 ± 0.06	0.46 ± 0.05	0.48 ± 0.05
$N_{\rm conc.}$ (10 ⁴ #·cm ⁻	1.4 ± 0.7	1.2 ± 0.6	0.9 ± 0.3	0.9 ± 0.3	1.2 ± 0.6	1.0 ± 0.6
3)	1. 4 ± 0./	1.2 ± 0.0	0.9 ± 0.3	0.9 ± 0.3		-10
$V_{conc.}$ ($\mu m^3 \cdot cm^2$	22.5 ±	10.1 ±	17.0 ±	15.9 ±	$19.5 \pm$	$12.1 \pm$
3)	5.5	3.6	4.8	5.6	6.0	5.0
R _{eff} (nm)	124.8 ±	102.8 ±	126.2 ±	118.6 ±	$125.0 \pm$	110.6 ±
Reff (IIIII)	10.7	12.4	10.6	11.4	10.0	13.7
NF _{ACC} .	0.28 ± 0.11	0.20 ± 0.10	0.28 ± 0.06	0.33 ± 0.07	0.28 ± 0.09	0.26 ± 0.11
$VF_{ACC.}$	0.96 ± 0.02	0.91 ± 0.04	0.96 ± 0.02	0.96 ± 0.02	0.96 ± 0.02	0.93 ± 0.04
T (°C)	34.0 ± 3.4	36.8 ± 3.1	33.2 ± 3.3	37.6 ± 2.7	33.8 ± 3.4	37.3 ± 3.0
RH (%)	46.6 ± 14.1	34.7 ± 9.1	52.6 ± 13.0	34.0 ± 7.5	47.9 ± 13.7	33.5 ± 8.5
WS (m/s)	1.1 ± 0.6	1.8 ± 1.0	1.4 ± 1.1	1.6 ± 0.9	1.2 ± 0.8	1.8 ± 1.0
VIS (km)	23.3 ± 6.3	29.9 ± 0.7	25.7 ± 5.1	29.2 ± 2.1	25.0 ± 5.6	29.8 ± 1.2
MLH (m)	$1062.0 \pm$	$1461.3 \pm$	$1075.6 \pm$	$1340.8 \pm$	$1063.3 \pm$	$1454.8 \pm$
	475.6	529.9	415.4	589.8	465.8	562.6
$PM_{2.5} (\mu g \cdot m^{-3})$	18.3 ± 6.2	9.3 ± 4.5	10.5 ± 4.2	11.8 ± 4.0	15.1 ± 6.6	10.1 ± 4.4
$NO_2 (\mu g \cdot m^{-3})$	30.8 ± 18.7	22.7 ± 12.8	21.7 ± 9.6	33.4 ± 19.2	29.8 ± 19.1	24.8 ± 15.4
$SO_2 (\mu g \cdot m^{-3})$	7.2 ± 1.8	8.8 ± 2.3	6.4 ± 1.5	9.6 ± 3.9	6.9 ± 1.8	9.0 ± 3.0
$O_3 (\mu g \cdot m^{-3})$	108.2 ± 62.2	84.1 ± 50.2	98.7 ± 51.9	82.3 ± 58.3	100.2 ± 61.1	82.5 ± 49.5
$CO (mg \cdot m^{-3})$	0.57 ± 0.10	0.44 ± 0.09	0.53 ± 0.05	0.51 ± 0.10	0.55 ± 0.10	0.45 ± 0.09
O_3/O_X	0.71 ± 0.24	0.72 ± 0.21	0.78 ± 0.14	0.62 ± 0.27	0.70 ± 0.25	0.70 ± 0.22
FR (cm ⁻³ ·s ⁻¹)	17.10 ± 7.79	11.22 ± 6.81	/	/	/	/
GR _{<25 nm} (nm·h ⁻¹)	13.68 ± 3.39	9.31 ± 3.23	/	/	/	/
GR _{25-40 nm} (nm·h ⁻¹)	7.12 ± 2.05	9.22 ± 4.28	/	/	/	/
$GR_{40-60 \text{ nm}} (nm \cdot h^{-1})$	6.87 ± 6.27	4.41 ± 1.72	/	/	/	/
GR _{60-80 nm} (nm·h ⁻¹)	10.73 ± 8.37	5.51 ± 2.98	/	/	/	/
CS (s ⁻¹)	2.3 ±	1.3 ±	/	/	/	/

	0.4×10^{-2}	0.3×10^{-2}				
C_{ong} $(a-1)$	$1.3 \pm$	$0.9 \pm$	/	/	/	/
CoagS (s ⁻¹)	0.2×10^{-4}	0.2×10^{-4}	/	/	/	/
HBF ₅₂₅ , RH/HBF ₅₂₅	1.22 ± 0.10	1.78 ± 0.29	1.39 ± 0.24	1.43 ± 0.18	1.32 ± 0.19	1.63 ± 0.29
$f_{RF}(RH)$	1.89 ± 0.17	2.21 ± 0.23	1.93 ± 0.14	2.01 ± 0.18	1.91 ± 0.16	2.15 ± 0.23

Table S3. A summary of the input parameters for the sensitivity analysis with the Mie models.

	Variable	Mode	Mean	Range
	D (nm)	Uf.	39	14-100
	$D_{Pg}\left(nm\right)$	Acc.	173	100-300
	GSD	Uf.	1.69	1.2-2.1
	GSD	Acc.	1.56	1.2-2.7
P1 NPF _{polluted}	NT (II -3)	Uf.	16,844	2,000-28,000
	$N_t (\# \cdot cm^{-3})$	Acc.	2,311	1,000-5,500
	- (DII)	Uf.	1.14	1.0-1.3
	g(RH)	Acc.	1.26	1.0-1.3
	n	/	1.45	1.3-1.8
	D- (nm)	Uf.	39	14-100
	$D_{Pg}\left(nm\right)$	Acc.	150	100-300
	CCD	Uf.	1.46	1.2-2.1
	GSD	Acc.	1.65	1.2-2.7
P2 NPF _{clean, HW}	N (#3)	Uf.	14,963	2,000-28,000
	$N_t (\# \cdot cm^{-3})$	Acc.	2,251	1,000-5,500
	- (DII)	Uf.	1.15	1.0-1.3
	g(RH)	Acc.	1.27	1.0-1.3
	n	/	1.44	1.3-1.8

297 **References**

- 298 Brock, C. A., Wagner, N. L., Anderson, B. E., Attwood, A. R., Beyersdorf, A.,
- 299 Campuzano-Jost, P., Carlton, A. G., Day, D. A., Diskin, G. S., Gordon, T. D., Jimenez, J.
- L., Lack, D. A., Liao, J., Markovic, M. Z., Middlebrook, A. M., Ng, N. L., Perring, A. E.,
- Richardson, M. S., Schwarz, J. P., Washenfelder, R. A., Welti, A., Xu, L., Ziemba, L. D.,
- and Murphy, D. M.: Aerosol optical properties in the southeastern United States in
- 303 summer Part 1: Hygroscopic growth, Atmos. Chem. Phys., 16, 4987–5007,
- 304 https://doi.org/10.5194/acp-16-4987-2016, 2016.
- Castro, L. M., Pio, C. A., Harrison, R. M., and Smith, D. J. T.: Carbonaceous aerosol in
- 306 urban and rural European atmospheres: Estimation of secondary organic carbon
- 307 concentrations, Atmos. Environ., 33, 2771–2781, https://doi.org/10.1016/S1352-
- 308 2310(98)00331-8, 1999.
- Chen, J., Wu, Z., Chen, J., Reicher, N., Fang, X., Rudich, Y., and Hu, M.: Size-resolved
- atmospheric ice-nucleating particles during East Asian dust events, Atmos. Chem. Phys.,
- 311 21, 3491–3506, https://doi.org/10.5194/acp-21-3491-2021, 2021.
- 312 Chen, J., Zhao, C. S., Ma, N., Liu, P. F., Göbel, T., Hallbauer, E., Deng, Z. Z., Ran, L.,
- 313 Xu, W. Y., Liang, Z., Liu, H. J., Yan, P., Zhou, X. J., and Wiedensohler, A.: A
- parameterization of low visibilities for hazy days in the North China Plain, Atmos.
- Chow, J. C., Watson, J. G., Chen, L. W. A., Chang, M. C. O., Robinson, N. F., Trimble,
- D., and Kohl, S.: The IMPROVE A temperature protocol for thermal/optical carbon
- analysis: Maintaining consistency with a long-term database, J. Air Waste Manag. Assoc.,
- 318 57, 1014–1023, https://doi.org/10.3155/1047-3289.57.9.1014, 2007.
- Chow, J. C., Watson, J. G., Robles, J., Wang, X., Chen, L. W. A., Trimble, D. L., Kohl, S.
- 320 D., Tropp, R. J., and Fung, K. K.: Quality assurance and quality control for
- 321 thermal/optical analysis of aerosol samples for organic and elemental carbon, Anal.
- 322 Bioanal. Chem., 401, 3141–3152, https://doi.org/10.1007/s00216-011-5103-3, 2011.

- Dal Maso, M., Kulmala, M., Riipinen, I., Wagner, R., Hussein, T., Aalto, P. P., and
- 324 Lehtinen, K. E. J.: Formation and growth of fresh atmospheric aerosols: Eight years of
- aerosol size distribution data from SMEAR II, Hyytiälä, Finland, Boreal Environ. Res.,
- 326 10, 323–336, 2005.
- Denjean, C., Formenti, P., Picquet-Varrault, B., Camredon, M., Pangui, E., Zapf, P.,
- Katrib, Y., Giorio, C., Tapparo, A., Temime-Roussel, B., Monod, A., Aumont, B., and
- Doussin, J. F.: Aging of secondary organic aerosol generated from the ozonolysis of α-
- pinene: Effects of ozone, light and temperature, Atmos. Chem. Phys., 15, 883–897,
- 331 https://doi.org/10.5194/acp-15-883-2015, 2015.
- Dominick, D., Wilson, S. R., Paton-Walsh, C., Humphries, R., Guérette, E. A., Keywood,
- 333 M., Kubistin, D., and Marwick, B.: Characteristics of airborne particle number size
- distributions in a coastal-urban environment, Atmos. Environ., 186, 256–265,
- 335 https://doi.org/10.1016/j.atmosenv.2018.05.031, 2018.
- Fitsiou, E., Pulido, T., Campisi, J., Alimirah, F., and Demaria, M.: Cellular Senescence
- and the Senescence-Associated Secretory Phenotype as Drivers of Skin Photoaging, J.
- 338 Invest. Dermatol., 141, 1119–1126, https://doi.org/10.1016/j.jid.2020.09.031, 2021.
- Grainger, R. G., Lambert, A., Rodgers, C. D., Taylor, F. W., and Deshler, T.:
- 340 Stratospheric aerosol effective radius, surface area and volume estimated from infrared
- measurements, J. Geophys. Res., 100, https://doi.org/10.1029/95jd00988, 1995.
- Hamed, A., Joutsensaari, J., Mikkonen, S., Sogacheva, L., Dal Maso, M., Kulmala, M.,
- Cavalli, F., Fuzzi, S., Facchini, M. C., Decesari, S., Mircea, M., Lehtinen, K. E. J., and
- Laaksonen, A.: Nucleation and growth of new particles in Po Valley, Italy, Atmos. Chem.
- 345 Phys., 7, 355–376, https://doi.org/10.5194/acp-7-355-2007, 2007.
- Hansen, J. E. and Travis, L. D.: Light scattering in planetary atmospheres, Space Sci.
- 347 Rev., 16, 527–610, https://doi.org/10.1007/BF00168069, 1974.
- Hao, Y., Gou, Y., Wang, Z., Huang, W., Wan, F., Tian, M., and Chen, J.: Current
- 349 challenges in the visibility improvement of urban Chongqing in Southwest China: From

- 350 the perspective of PM2.5-bound water uptake property over 2015–2021, Atmos. Res.,
- 351 300, 107215, https://doi.org/10.1016/j.atmosres.2023.107215, 2024.
- 352 Hong, J., Ma, J., Ma, N., Shi, J., Xu, W., Zhang, G., Zhu, S., Zhang, S., Tang, M., Pan, X.,
- 353 Xie, L., Li, G., Kuhn, U., Yan, C., Qi, X., Zha, Q., Nie, W., Tao, J., He, Y., Zhou, Y.,
- Sun, Y., Xu, H., Liu, L., Cai, R., Zhou, G., Kuang, Y., Yuan, B., Wang, Q., Petäjä, T.,
- Kerminen, V. M., Kulmala, M., Cheng, Y., and Su, H.: Low Hygroscopicity of Newly
- Formed Particles on the North China Plain and Its Implications for Nanoparticle Growth,
- 357 Geophys. Res. Lett., 51, https://doi.org/10.1029/2023GL107516, 2024.
- Hussein, T., Puustinen, A., Aalto, P. P., Mäkelä, J. M., Hämeri, K., and Kulmala, M.:
- 359 Urban aerosol number size distributions, Atmos. Chem. Phys., 4, 391–411,
- 360 https://doi.org/10.5194/acp-4-391-2004, 2004.
- Jung, C. H., Shin, H. J., Lee, J. Y., and Kim, Y. P.: Sensitivity and contribution of
- 362 organic aerosols to aerosol optical properties based on their refractive index and
- 363 hygroscopicity, Atmosphere (Basel)., 7, https://doi.org/10.3390/atmos7050065, 2016.
- Kerminen, V. M., Chen, X., Vakkari, V., Petäjä, T., Kulmala, M., and Bianchi, F.:
- 365 Atmospheric new particle formation and growth: Review of field observations, Environ.
- 366 Res. Lett., 13, https://doi.org/10.1088/1748-9326/aadf3c, 2018.
- 367 Kuang, Y., He, Y., Xu, W., Zhao, P., Cheng, Y., Zhao, G., Tao, J., Ma, N., Su, H., Zhang,
- 368 Y., Sun, J., Cheng, P., Yang, W., Zhang, S., Wu, C., Sun, Y., and Zhao, C.: Distinct
- diurnal variation in organic aerosol hygroscopicity and its relationship with oxygenated
- organic aerosol, Atmos. Chem. Phys., 20, 865–880, https://doi.org/10.5194/acp-20-865-
- 371 2020, 2020.
- Kuang, Y., Zhao, C. S., Zhao, G., Tao, J. C., Xu, W., Ma, N., and Bian, Y. X.: A novel
- method for calculating ambient aerosol liquid water content based on measurements of a
- humidified nephelometer system, Atmos. Meas. Tech., 11, 2967–2982,
- 375 https://doi.org/10.5194/amt-11-2967-2018, 2018.

- Kuang, Y., Zhao, C., Tao, J., Bian, Y., Ma, N., and Zhao, G.: A novel method for
- deriving the aerosol hygroscopicity parameter based only on measurements from a
- 378 humidified nephelometer system, Atmos. Chem. Phys., 17, 6651–6662,
- 379 https://doi.org/10.5194/acp-17-6651-2017, 2017.
- Kulmala, M., Petäjä, T., Nieminen, T., Sipilä, M., Manninen, H. E., Lehtipalo, K., Dal
- Maso, M., Aalto, P. P., Junninen, H., Paasonen, P., Riipinen, I., Lehtinen, K. E. J.,
- Laaksonen, A., and Kerminen, V. M.: Measurement of the nucleation of atmospheric
- aerosol particles, Nat. Protoc., 7, 1651–1667, https://doi.org/10.1038/nprot.2012.091,
- 384 2012.
- 385 Lu, Y., Yan, C., Fu, Y., Chen, Y., Liu, Y., Yang, G., Wang, Y., Bianchi, F., Chu, B.,
- Zhou, Y., Yin, R., Baalbaki, R., Garmash, O., Deng, C., Wang, W., Liu, Y., Petäjä, T.,
- Kerminen, V. M., Jiang, J., Kulmala, M., and Wang, L.: A proxy for atmospheric daytime
- 388 gaseous sulfuric acid concentration in urban Beijing, Atmos. Chem. Phys., 19, 1971-
- 389 1983, https://doi.org/10.5194/acp-19-1971-2019, 2019.
- Nairn, J. R. and Fawcett, R. J. B.: The excess heat factor: A metric for heatwave intensity
- and its use in classifying heatwave severity, Int. J. Environ. Res. Public Health, 12, 227–
- 392 253, https://doi.org/10.3390/ijerph120100227, 2014.
- Peng, C., Tian, M., Chen, Y., Wang, H., Zhang, L., Shi, G., Liu, Y., Yang, F., and Zhai,
- 394 C.: Characteristics, formation mechanisms and potential transport pathways of PM2.5 at a
- rural background site in Chongqing, Southwest China, Aerosol Air Qual. Res., 19, 1980–
- 396 1992, https://doi.org/10.4209/aaqr.2019.01.0010, 2019.
- Peng, C., Tian, M., Wang, X., Yang, F., Shi, G., Huang, R. J., Yao, X., Wang, Q., Zhai,
- 398 C., Zhang, S., Qian, R., Cao, J., and Chen, Y.: Light absorption of brown carbon in
- 399 PM2.5 in the Three Gorges Reservoir region, southwestern China: Implications of
- 400 biomass burning and secondary formation, Atmos. Environ., 229, 117409,
- 401 https://doi.org/10.1016/j.atmosenv.2020.117409, 2020.
- Rissler, J., Vestin, A., Swietlicki, E., Fisch, G., Zhou, J., Artaxo, P., and Andreae, M. O.:
- Size distribution and hygroscopic properties of aerosol particles from dry-season biomass

- burning in Amazonia, Atmos. Chem. Phys., 6, 471–491, https://doi.org/10.5194/acp-6-
- 405 471-2006, 2006.
- Rosati, B., Isokääntä, S., Christiansen, S., Jensen, M. M., Moosakutty, S. P., De Jonge, R.
- W., Massling, A., Glasius, M., Elm, J., Virtanen, A., and Bilde, M.: Hygroscopicity and
- 408 CCN potential of DMS-derived aerosol particles, Atmos. Chem. Phys., 22, 13449–13466,
- 409 https://doi.org/10.5194/acp-22-13449-2022, 2022.
- 410 Schkolnik, G., Chand, D., Hoffer, A., Andreae, M. O., Erlick, C., Swietlicki, E., and
- Rudich, Y.: Constraining the density and complex refractive index of elemental and
- organic carbon in biomass burning aerosol using optical and chemical measurements,
- 413 Atmos. Environ., 41, 1107–1118, https://doi.org/10.1016/j.atmosenv.2006.09.035, 2007.
- Stein, A. F., Draxler, R. R., Rolph, G. D., Stunder, B. J. B., Cohen, M. D., and Ngan, F.:
- Noaa's hysplit atmospheric transport and dispersion modeling system, Bull. Am.
- 416 Meteorol. Soc., 96, 2059–2077, https://doi.org/10.1175/BAMS-D-14-00110.1, 2015.
- 417 Strader, R., Lurmann, F., and Pandis, S. N.: Evaluation of secondary organic aerosol
- 418 formation in winter, Atmos. Environ., 33, 4849-4863, https://doi.org/10.1016/S1352-
- 419 2310(99)00310-6, 1999.
- 420 Tan, F., Zhang, H., Xia, K., Jing, B., Li, X., Tong, S., and Ge, M.: Hygroscopic behavior
- 421 and aerosol chemistry of atmospheric particles containing organic acids and inorganic
- 422 salts, npj Clim. Atmos. Sci., 7, 1–21, https://doi.org/10.1038/s41612-024-00752-9, 2024.
- Tian, J., Guan, H., Zhou, Y., Zheng, N., Xiao, H., Zhao, J., Zhang, Z., and Xiao, H.:
- 424 Isotopic source analysis of nitrogen-containing aerosol: A study of PM2.5 in Guiyang
- 425 (SW, China), Sci. Total Environ., 760, 143935,
- 426 https://doi.org/10.1016/j.scitotenv.2020.143935, 2021.
- Wan, F., Hao, Y., Huang, W., Wang, X., Tian, M., and Chen, J.: Hindered visibility
- 428 improvement despite marked reduction in anthropogenic emissions in a megacity of
- 429 southwestern China: An interplay between enhanced secondary inorganics formation and

- 430 hygroscopic growth at prevailing high RH conditions, Sci. Total Environ., 895, 165114,
- 431 https://doi.org/10.1016/j.scitotenv.2023.165114, 2023.
- Wang, H., Tian, M., Chen, Y., Shi, G., Liu, Y., Yang, F., Zhang, L., Deng, L., Yu, J.,
- Peng, C., and Cao, X.: Seasonal characteristics, formation mechanisms and source origins
- of PM2.5 in two megacities in Sichuan Basin, China, Atmos. Chem. Phys., 18, 865–881,
- 435 https://doi.org/10.5194/acp-18-865-2018, 2018.
- Wang, Y. Q.: MeteoInfo: GIS software for meteorological data visualization and analysis,
- 437 Meteorol. Appl., 21, 360–368, https://doi.org/10.1002/met.1345, 2014.
- 438 Xu, W., Kuang, Y., Bian, Y., Liu, L., Li, F., Wang, Y., Xue, B., Luo, B., Huang, S., Yuan,
- 439 B., Zhao, P., and Shao, M.: Current Challenges in Visibility Improvement in Southern
- 440 China, Environ. Sci. Technol. Lett., 7, 395–401,
- 441 https://doi.org/10.1021/acs.estlett.0c00274, 2020.
- 442 Xue, B., Kuang, Y., Xu, W., and Zhao, P.: Joint increase of aerosol scattering efficiency
- and aerosol hygroscopicity aggravate visibility impairment in the North China Plain, Sci.
- 444 Total Environ., 839, 141163, https://doi.org/10.1016/j.scitotenv.2022.156279, 2022.
- Zhao, G., Hu, M., Fang, X., Tan, T., Xiao, Y., Du, Z., Zheng, J., Shang, D., Wu, Z., Guo,
- S., and Zhao, C.: Larger than expected variation range in the real part of the refractive
- 447 index for ambient aerosols in China, Sci. Total Environ., 779, 146443,
- 448 https://doi.org/10.1016/j.scitotenv.2021.146443, 2021.
- 249 Zhu, Y., Shen, Y., Li, K., Meng, H., Sun, Y., Yao, X., Gao, H., Xue, L., and Wang, W.:
- 450 Investigation of Particle Number Concentrations and New Particle Formation With
- 451 Largely Reduced Air Pollutant Emissions at a Coastal Semi-Urban Site in Northern
- 452 China, J. Geophys. Res. Atmos., 126, 1–20, https://doi.org/10.1029/2021JD035419, 2021.